Synaptic targets of functionally specialized R7 and R8 photoreceptors in the central eye and dorsal rim area of *Drosophila*

Emil Kind[1,*], Kit D. Longden[2,*], Aljoscha Nern[2,*], Arthur Zhao[2,*], Gizem Sancer[1,3], Miriam Flynn[2], Connor Laughland[2], Bruck Gezahegn[2], Henrique Ludwig[2], Alex Thomson[2], Tessa Obrusnik[1], Paula G. Alarcón[1], Heather Dionne[2], Davi D. Bock[2,4], Gerald M. Rubin[2], Michael B. Reiser[2,#], and Mathias F. Wernet[1,#]

1 : Instititut für Biologie – Abteilung Neurobiologie, Fachbereich Biologie, Chemie & Pharmazie, Freie Universität Berlin, Königin-Luise Strasse 1-3, 14195 Berlin, Germany.

2 : Janelia Research Campus, Howard Hughes Medical Institute, Ashburn, USA

3: Current address: Department of Neuroscience, Yale University School of Medicine, Sterling Hall of Medicine C-400, 333 Cedar Street, New Haven, CT 06510, USA.

4: Current address: Department of Neurological Sciences, University of Vermont, Burlington, VT 05405, USA.

* : These author contributed equally

#: Corresponding authors:

reiserm@janelia.hhmi.org

mathias.wernet@fu-berlin.de

Abstract

Color and polarization provide complementary information about the world and are detected by specialized photoreceptors. However, the downstream neural circuits that process these distinct modalities are incompletely understood in any animal. We have systematically reconstructed, using light and electron microscopy, the synaptic targets of the photoreceptors specialized to detect color and polarized light in *Drosophila*. We identified known and novel downstream targets that are selective for different wavelengths as well as for polarized light and followed their projections to other areas in the optic lobes and the central brain. Strikingly, photoreceptors in the polarization-sensitive dorsal rim area target fewer cell types, that lack strong connections to the lobula, a neuropil with a proposed role in color processing. Our reconstruction identifies shared wiring and modality-specific specializations for color and polarization vision, and provides a comprehensive view of the first steps of the pathways processing color and polarized light inputs.

Introduction

Both the wavelength and the polarization angle of light contain valuable information that can be exploited by many visual animals. For instance, color gradients across the sky can serve as navigational cues, and skylight's characteristic pattern of linear polarization can also inform navigation by indicating the orientation relative to the sun (Heinze 2017; Figure 1A). The spectral content of light is detected by groups of photoreceptor cells containing rhodopsin molecules with different sensitivities, often organized in stochastic retinal mosaics (Rister and Desplan 2011), and specialized, polarization-sensitive photoreceptors have been characterized in many species, both vertebrates and invertebrates (Nilsson and Warrant 1999). These two visual modalities, color and polarization vision, require the processing of signals of specialized photoreceptors over a great range of spatial and temporal scales, and many questions remain about how the signals from functionally specialized photoreceptors are integrated in downstream neurons. Are color and polarization signal mixed at an early stage, or are they processed by different, modality-specific cell types? Do separate pathways exist that selectively process and convey information from photoreceptor types in the retinal mosaic to targets in the central brain? The full scope of the early synaptic stages of color and polarization circuitry is unknown in any animal, and the analysis of EM connectomes is ideally suited to exhaustively answer them, especially when corroborated with genetic labelling of cell types and circuit elements in light microscopy. Mapping neuronal connections within the *Drosophila* Full Adult Fly Brain (FAFB) dataset (Zheng et al. 2018), combined with the available powerful genetic tools available in *Drosophila*, provides an opportunity to address these questions.

While studies in many insects have contributed to the understanding of polarized light and color vision (Homberg 2015; Dacke and El Jundi 2018; Heinze 2017; Hempel de Ibarra, Vorobyev, and Menzel 2014), the visual system of of *Drosophila* offers many advantages for the exploration of neural circuits (Wernet, Huberman, and Desplan 2014). Anatomical studies are facilitated by the stereotyped, repetitive structure of the optic lobes, with many cell types, the so-called columnar neurons, found in repeated circuit units, called visual columns, that are

retinotopically arranged and each correspond to one of the ~800 unit eyes (ommatidia) of the compound eye. Many of over one hundred optic lobe cell types have been described in classical Golgi work (Fischbach and Dittrich 1989), by more recent studies combining genetic labeling with light microscopy, for example (Morante and Desplan 2008; Otsuna and Ito 2006; Wu et al. 2016; Nern, Pfeiffer, and Rubin 2015) and, for some cell types, through electron microscopic (EM) reconstructions that have revealed not only cell shapes but most importantly detailed synaptic connectivity (Takemura et al. 2015; Takemura et al. 2013; Takemura, Lu, and Meinertzhagen 2008; Meinertzhagen and O'Neil 1991; Rivera-Alba et al. 2011; Shinomiya et al. 2014). Furthermore, genetic tools (Jenett et al. 2012; Pfeiffer et al. 2008; Kvon et al. 2014; Dionne et al. 2018; Tirian and Dickson 2017), and, most recently, gene expression data (Davis et al. 2020; Konstantinides et al. 2018; Ozel et al. 2021; Kurmangaliyev et al. 2020) are available for many optic lobe cell types.

Each *Drosophila* ommatidium contains eight photoreceptor types whose output is processed in a series of synaptic layers called the lamina, medulla, lobula and lobula plate that together form the optic lobes of the fly (Fischbach and Dittrich 1989). Outer photoreceptors R1-6 project to the lamina neuropil, and serve as the main input to the motion vision circuitry (Mauss et al. 2017); inner photoreceptors R7 and R8 skip the lamina and project directly to the deeper medulla neuropil, that also receives lamina projections (Fischbach and Dittrich 1989). In the main part of the retina, R7 and R8 differ in their axonal target layers, with R7 projecting to layer M6, and R8 to layer M3 (Fischbach and Dittrich 1989). R7 and R8 can also differ in their rhodopsin expression, being sensitive to short wavelength UV (R7) and blue (R8), respectively, in so-called ‘pale’ ommatidia (Chou et al. 1996; Papatsenko, Sheng, and Desplan 1997), and to long wavelength UV (R7) and green (R8) in ‘yellow’ ommatidia (Salcedo et al. 1999; Huber et al. 1997). Pale and yellow ommatidia are distributed randomly throughout the main part of the retina (Feiler et al. 1992; Fortini and Rubin 1990), at an uneven ratio that is conserved across insects (Wernet, Perry, and Desplan 2015; Kind, Belušič, and Wernet 2020). Meanwhile, along the dorsal rim area (DRA) of the eye, the ommatidia are morphologically and molecularly specialized for detecting skylight polarization (Wernet et al. 2012; Wernet et al.

2003; Wada 1974a), that *Drosophila* can use to set a specific heading (Mathejczyk and Wernet 2020, 2019; Warren, Weir, and Dickinson 2018; Weir and Dickinson 2012). In the DRA ommatidia, R7 and R8 express the same UV rhodopsin (Rh3; Fortini and Rubin 1991, 1990) and detect perpendicular angles of polarized ultraviolet light (Weir et al. 2016). In contrast to the rest of the medulla, R7 and R8 in the DRA project to the same medulla layer (M6; Chin et al. 2014; Pollack and Hofbauer 1991; Fischbach and Dittrich 1989), where their targets are thought to include polarization-specific cell types (Sancer et al. 2020; Sancer et al. 2019; Hardcastle et al. 2021). Across insects, a 'compass pathway' connects the DRA to the central brain via an optic glomerulus called the anterior optic tubercle (AOTU; Homberg 2015; Hardcastle et al. 2021; Pfeiffer and Kinoshita 2012). Anatomical and functional data from *Drosophila* suggests that the central medulla is also connected to the compass pathway (Omoto et al. 2017; Hardcastle et al. 2021; Otsuna, Shinomiya, and Ito 2014), potentially forming parallel pathways for processing different celestial cues (Timaeus et al. 2020; Tai, Chin, and Chiang 2021).

Electron microscopy studies have begun to reveal some of the circuitry downstream of R7 and R8 (Takemura et al. 2015; Takemura et al. 2013; Gao et al. 2008). For example, axons of R7 and R8 from the same ommatidium are reciprocally connected with inhibitory synapses, leading to color-opponent signals in their presynaptic terminals (Schnaitmann et al. 2018). Interestingly, R7 and R8 in the DRA also inhibit each other (Weir et al. 2016). Other known R7 and R8 targets in the main medulla include local interneurons (e.g. Dm8; Gao et al. 2008; Karuppudurai et al. 2014; Pagni et al. 2021; Menon et al. 2019) and projection neurons that provide connections to deeper optic lobe regions (e.g. Tm5 and Tm20 neurons; Karuppudurai et al. 2014; Meinertzhagen et al. 2009; Gao et al. 2008). A previous light microscopy study (Karuppudurai et al. 2014) identified a single cell type, Tm5a, that is specific for pale medulla columns; this neurons has been used to identify pale and yellow columns in an EM volume (Menon et al. 2019; Takemura et al. 2015; Karuppudurai et al. 2014). Using genetic labelling techniques, four classes of TmY cells have also been reported as specific targets of pale versus yellow photoreceptors (Jagadish et al. 2014), yet previous connectomic studies did not

reveal similar cells. The currently most comprehensive EM study of the medulla reconstructed the connections between neurons in 7 neighboring medulla columns (Takemura et al. 2015), revealing an exquisitely detailed inventory of cell types connected to R7/8. This dataset, now publicly available (Clements et al. 2020), is remarkable for its dense reconstruction of columnar circuits, but could not be used to identify many multicolumnar neurons, that were cut-off at the edge of the data volume, leaving 40% of R7/8 synapses to unidentified cell types. In addition, no EM-based reconstructions of DRA columns that would reveal the underlying synapses is currently available.

Here, we present a comprehensive reconstruction of all R7 and R8 synaptic outputs and inputs, from pairs of pale and yellow columns and from three DRA columns in the FAFB dataset. We discovered a large visual projection neuron with distinctive morphology, named accessory medulla cell type 12 (aMe12), that selectively innervates pale ommatidia across the whole medulla. We identified this cell in the FAFB dataset to enumerate the connectivity in two pale and two yellow columns of R7 and R8 with known and novel cell types within the optic lobes and projecting to the central brain, including more cells with pale-yellow specificity, and synapses on axons between neuropils. In the DRA, we show that cellular diversity is reduced, with local interneurons and projection neurons to the AOTU dominating, and connections to the lobula virtually missing. We identify circuit motifs shared between DRA and central columns, and describe modality-specific cell types, including cells with interhemispheric connections and projections to the central brain. Together, we identify the connected neurons that account for 96% of R7/8 synapses, a nearly complete set of the neurons that comprise the first step of the pathways through which color and polarization signals are transduced to the rest of the brain.

Results

Systematic reconstruction of all synaptic targets of different R7 and R8 photoreceptor subtypes

From an electron microscopic data set spanning the full adult female brain (FAFB; Zheng et al. 2018), we reconstructed R7 and R8 photoreceptor axons in the central region of

the right hemisphere, as well as R7/R8 pairs from 27 DRA columns (Figure 1C). From these, we selected seven 'seed columns' (four central, three DRA), for which all pre- and post-synaptic sites of the photoreceptor axons were identified and manually annotated in the EM images (Figure 1F; Material and Methods). There were 422 skeletons, corresponding to individual cells, contacted by the seed column photoreceptors, and we focused our analysis on the 245 individual cells with >2 synapses to or from the photoreceptors. We reconstructed the morphology of these cells with a sufficient degree of completeness to ascribe a unique cell type to 92% (225/245) or to identify a cell class (Dm, Mi, Tm, or TmY cell class) for an additional 6.5% (16/245), so that 98% (241/245) of these cells were identified. We also traced and uniquely identified the cell type of all 30 cells that provided >2 synaptic inputs to the photoreceptors. In total, we identified 4043 synaptic connections from the seed column R7 and R8 photoreceptors, and 970 synaptic inputs to them, summarized in Figure 1H.

To distinguish between pale and yellow columns we took advantage of our recent discovery of one specific cell type from the 'accessory medulla' (aMe) that widely arborised in the medulla with ascending branches that align with the photoreceptors (Figure 1Ei-iii). The cell type was selective for R8 input, and showed a strong preference for innervating pale columns (Figure 1D, Eiii). We identified three of these cells per hemisphere (hereinafter referred to as aMe12), that had heavily overlapping arbors, but only rarely shared ascending branches in the same columns (3/779 columns). Using the presence of aMe12 branches, we were able to assign as pale 38% (297/779) of the medulla columns, in good agreement with studies on the retinal mosaic of *Drosophila* (Feiler et al. 1992; Fortini and Rubin 1990; Bell, Earl, and Britt 2007; Hilbrant et al. 2014). Since further analysis identified a total of 42 DRA columns (see below), we assigned the remaining columns as nominally yellow (Figure 1C). Our reconstructions also revealed another new pale-selective visual projection neuron, that we named ML-VPN1, and confirmed the previously reported yellow-selectivity of Tm5a cells (Menon et al. 2019; Karuppudurai et al. 2014), findings that further supported the designations of pale and yellow seed columns (see below).

After mapping the pale and yellow columns, we selected four adjacent central seed columns, two nominally pale and two nominally yellow (Figure 1C). Across the four central seed columns, the absolute number of both synaptic inputs and outputs for R7 and R8 photoreceptors were in good agreement with previous reports analyzing a medulla FIB-SEM data set—a somewhat surprising result in light of the reported increases in synapse counts between TEM and FIB-SEM data sets (Takemura et al. 2015; Figure 1 – figure supplement 2A-D). As we had access to the complete brain volume, we additionally found substantial numbers of synapses in the axon bundles projecting between the lamina and the medulla, which accounted for 14% and 12% of the output synapses for R7 and R8 respectively, and 16% and 27% of their input synapses (Figure 1 F, Figure 1 – figure supplement 2G).

We readily identified columns in the DRA region of the medulla since it is only there that both R7 and R8 terminate in medulla layer M6 (Pollack and Hofbauer 1991; Fortini and Rubin 1991; Sancer et al. 2019; Chin et al. 2014; Fischbach and Dittrich 1989; Figure 1F, arrow). The morphology of DRA-specific Dm-DRA1 cells differs significantly between central and polar positions of the DRA (Sancer et al. 2019), and we therefore chose one polar DRA seed column and two more equatorial columns (Figure 1C). Beyond the 27 DRA columns with manually traced R7 and R8 photoreceptors we mapped the full extent of the DRA region by systematically probing for the presence of two inner photoreceptor profiles in layer M6 without reconstruction (see Materials and Methods), which resulted in a total of 42 identified DRA columns (Figure 1C). Direct comparison of the absolute number of pre- versus post-synaptic sites between central and DRA photoreceptors revealed drastic differences between R7 and R8: while the numbers of R7 and R7-DRA presynapses were comparable (250 ±27 for R7-DRA vs 285 ±26 for R7), the number of R8-DRA presynapses was drastically reduced by ~60% compared to central columns (155 ±10 for R8-DRA vs 362 ±10 for R8). In particular, there was a striking reduction in the number of synapses from R8 to cells intrinsic to the medulla and to cells that projected to the lobula (see below and Figure 1G, H).

We have endeavored to make this comprehensive data set as accessible and navigable as possible. In the following sections we first describe the connections of the central

eye R7 and R8 cells (Figure 2 – 5), following the sequence of cell classes in Figure 1G-H, before presenting the connections of the DRA (Figures 6 – 9). The synaptic outputs from and inputs to the central pale and yellow R7/8 cells are summarized in Tables 1-2, for the R7/8-DRA in Tables 3-4, and presentations of individual cell types include summaries of total R7/8 synapse counts (e.g., Figure 1Eiii for aMe12). The text highlights downstream cell types that are selective for inputs from either R7 or R8, or are preferentially found in pale or yellow columns. We used 65% as the threshold to consider an input selective and tables of connectivities of the individual cells are arranged by cell type and collected together into a single file (Supplementary File 1). The main figures show the morphology of reconstructed exemplars, with the many full reconstructions noted (and listed in Materials and Methods), while the morphologies of individual cells are collected together into a single file (Supplementary File 2). For the cell types for which we are unaware of published, detailed descriptions, we endeavored to produce light microscopic images of single cell clones which were matched largely based on the cell body location, the extent and neuropil-layer-specific branching patterns, and comparisons to any other know cell types (see Materials and Methods). In a few cases, we also use light miscroscopy to illustrate specific features of known neurons or to explore additional properties (such as direct co-labeling with markers for pale and yellow columns) that are not readily accessible by EM.

Connections between central eye R7 and R8 photoreceptors, and with lamina cells

Photoreceptors R7 and R8 inhibit each other via direct histaminergic synapses, an important mechanism for converting their sensitivity to specific wavelengths into presynaptic color-opponency (Schnaitmann et al. 2018). We reconstructed a large proportion of the reciprocal synapses between the R7 and R8 cells from central seed columns in the axonal projection between the lamina and the medulla (Figure 2A, Figure 1 – figure supplement 2G). Axons of both R7 and R8 cells were thicker just before they entered the medulla, consistent with anatomical specializations in the optic chiasm (Fischbach and Dittrich 1989). For the R8 cells, ~80% of the synaptic input from R7 cells was found in the axonal projection (mean 11.5

extramedulla synapses per cell, range 9-17), and the R8 inputs to the R7 cells in this region were as frequent (mean 10.3 extramedulla synapses per cell, range 5-13). These results were not anticipated by prior EM reconstructions that surveyed synaptic connections within the neuropils, and our numbers were therefore substantial increases in the numbers of inter-photoreceptor synapses (Takemura et al. 2015; Meinertzhagen and O'Neil 1991; Figure 1 – figure supplement 2D).

Photoreceptors R7 and R8 pass through the lamina without forming synapses there (Meinertzhagen and O'Neil 1991), and instead form synapses with lamina cell types within the medulla (Takemura et al. 2013; Takemura, Lu, and Meinertzhagen 2008). Our reconstructions further revealed that 58% of the R7/R8 inputs to the lamina cells L1 and L3 were also located within the optic chiasm (Figure 1 – figure supplement 1B, Figure 1 – figure supplement 2G, Figure 2 – figure supplement 1A-B).

Central eye R7 and R8 connections with distal medulla cells

The distal medulla (Dm) neurons included the strongest targets of the R7 and R8 photoreceptors (Table 1). Dm9 is a recently characterized glutaminergic cell type that provides excitatory feedback onto R7 and R8 cells, regulating their gain and augmenting their color-opponency (Heath et al. 2020; Davis et al. 2020; Uhlhorn and Wernet 2020; Gao et al. 2008). This cell type alone accounted for more than 90% all the synaptic inputs to the R7 and R8 that were not from photoreceptors (333/369 synapses, Table 2). Dm9 cells span multiple columns (Nern, Pfeiffer, and Rubin 2015; Takemura et al. 2015; Figure 2B), and we reconstructed a total of six Dm9 cells that were contacted by the eight R7/8 cells from our central seed columns, which together received 16% of all R7/8 synapses, and provided 57% of the total synapses to these cells (Tables 1, 2). One completely reconstructed Dm9 cell received 92 synapses per seed column (mean, range 78-102), and provided 70 synapses per seed column (mean, range 64-78) offering the most detailed picture of Dm9 connectivity yet (Supplementary File 1—Dm9 outgoing). While its R7 and R8 inputs were biased towards R8 (31% R7 vs 69% R8), the output synapses were balanced, weakly favoring R7 (55% R7 vs 45% R8). Importantly, pale and

yellow columns were equally contacted by Dm9 (outputs from R7 and R8: 54% pale vs 46% yellow; inputs from R7 and R8: 53% pale vs 47% yellow). In total, 8% of the synapses from R7 and R8 to Dm9 were located outside the medulla (34/445 of all R7/8 synapses onto Dm9), on processes that follow the photoreceptors' axonal projections (Figure 2Bii, arrow).

The most strongly connected R7 target cell type was Dm8, a central component of *Drosophila*'s circuitry mediating color vision and wavelength-specific phototaxis (Gao et al. 2008; Melnattur et al. 2014; Pagni et al. 2021). Dm8 has also recently gained interest for illustrating the developmental mechanisms for determining a cell's fate downstream from a sensory neuron with a stochastic fate (Courgeon and Desplan 2019). Individual Dm8 cells cover multiple columns in medulla layer M6 (Gao et al. 2008; Nern, Pfeiffer, and Rubin 2015; Luo et al. 2020), and extend processes vertically, with one characteristic process usually reaching higher than the others, up to layer M3, defining the so-called 'home' column for a given Dm8 cell (Figure 2Ci, arrow). The existence of pale and yellow subtypes of Dm8 cells with home columns raised the possibility that Dm8 cells may have a center-surround organization of pale and yellow inputs. In our reconstructions, we therefore analyzed the connectivity of each Dm8 cell with the surrounding pale and yellow R7 photoreceptors in relation to its home column.

The four R7 cells from our seed columns contacted 16 Dm8 cells altogether, and individual R7 cells synapsed onto 8 Dm8 cells (mean, range 6-10). Dm8 was exclusively a target of R7 cells, and there were no synapses from our seed column R8 cells onto Dm8s. There were five Dm8 cells with processes spanning our seed column R7s and receiving >40 synapses from them. Two of these cells had a pale home column and no input from yellow seed column R7 cells, and two had a yellow home column and received 13% and 20% of their from seed column input from pale R7 cells (Supplementary File 1—Dm8 outgoing). The fifth cell had a pale home column outside the seed column area, and its seed column inputs were divided evenly, 55% from pale and 45% from yellow. Collectively, these data revealed that Dm8 cells selectively innervated columns around the home column, but not simply the closest columns.

In view of the importance of Dm8 cells for processing R7 output, we extended our reconstructions to include all the photoreceptor inputs to three Dm8 cells, one with a pale home seed column, one with a yellow home seed column, and one with a yellow home column outside the seed columns (Figure 2Cii). All three Dm8 cells were most densely innervated by R7s in their home column: the yellow home column cells received 26% and 23% of their R7 input in the home column, and the pale home column cell received 52% (Figure 2Ciii). The innervated columns outside the home column were not simply the nearest neighbors of the home column, but formed a more irregular, idiosyncratic spatial pattern. Together, our data are consistent with Dm8 cells having a central, strong R7 input from either a pale or a yellow cell in its home column and a surround that integrates spatially varied pale and yellow R7 inputs.

Two additional distal medulla cell types, Dm11 and Dm2, were prominent R7 and/or R8 targets. Dm11 cells tile the medulla in layer M6, with each cell covering ~8 columns (Nern, Pfeiffer, and Rubin 2015; Figure 2Di), and sending vertical processes that reach far up into the optic chiasm, tracking the R7 and R8 photoreceptor axons (Courgeon and Desplan 2019; Figure 2Dii, Diii, arrows). Dm11 was R7-selective, with 87% of its seed column photoreceptor inputs originating from R7 cells (Figure 2Dii). Two-thirds of the Dm11 seed column R7/8 inputs were within the optic chiasm (44/63 synapses), and so this was another cell type that was innervated by photoreceptors much more than previously reported in a medulla FIB-SEM data set (Figure 1 – figure supplement 2D; Clements et al. 2020; Takemura et al. 2015). One Dm11 cell squarely occupied the four seed columns, receiving 52 synapses from the seed column photoreceptors, and this cell showed no clear bias for pale or yellow inputs (40% pale, 60% yellow; Supplementary File 1—Dm11 outgoing).

Dm11 is a significant input to Dm2 (Takemura et al. 2015; Clements et al. 2020), a cell type that is columnar, spans 1-2 columns, and has processes that reach from layer M6 up to layer M3 to receive synaptic input from R8 cells (Figure 2Ei, Eii; Takemura et al. 2013; Nern, Pfeiffer, and Rubin 2015). In our seed columns, there were four Dm2 cells that received photoreceptor input, with 77% from R8 cells (Figure 2Eii) and 81% from pale cells. Three of the cells were centered on seed columns, with two in the pale seed colums receiving 36 and

35 synapses, and the cell in a yellow seed column receiving 18; the fourth cell was centered on a neighboring yellow column and innervated one of the pale seed columns (Supplementary File 2—Dm2). In the columns of the medulla FIB-SEM data set that have been be identified as pale and yellow (Menon et al. 2019; see Materials and Methods), Dm2 was also R8-selective (70% of photoreceptor input from R8; Takemura et al. 2015; Clements et al. 2020). The cell was missing from one of the pale columns in that data set (Takemura et al. 2015), but in the columns where it was present, the cells received ~50% more synapses per column in the pale columns (18 mean, range 16-20 in pale columns, versus 12, mean, range 10-15 in yellow columns).

Central eye R7 and R8 connections to medulla intrinsic and medulla tangential intrinsic cells

The medulla intrinsic (Mi) cells connect the distal with the proximal medulla (Fischbach and Dittrich 1989). These two zones of the medulla are separated by the serpentine layer M7, that contains the processes of large medulla tangential cells, some of which are intrinsic to the medulla (Fischbach and Dittrich 1989). We refer to these medulla intrinsic tangential cells as Mti cells. The synaptic inputs of R7 and R8 cells to the Mi and Mti cell types proved to be of particular interest because these connections were depleted in the DRA region, even though Mi and Mti cell types were also present there (Figure 1H).

We found three Mti cells synaptically connected to our seed column R7 and R8 cells, and we matched these cells to light microscopy images of two separate, previously undescribed cell types using the locations of cell bodies, sizes of arbors and layer expression (Figure 3A,B). Both of these cell types received a modest number of synapses from our seed-column R7 and R8 cells (Mti1: 7 synapses; Mti2: 10 and 2 synapses, respectively; Supplementary File 1—Mti outgoing), yet were likely to be substantial targets of R7 and R8 cells overall since their processes covered large sections of the medulla (Figure 3A,B). The first cell type, which we refer to as Mti1, had a cell body located in the cell body layer distally to the medulla, similar to most medulla neurons. Its processes were asymmetrically oriented mainly along the dorsoventral axis, with dendrites that occupied layers M3-M6, and axonal

processes that spread laterally in layers M7-M8 (Figure 3A). The second cell type, here named Mti2 (Figure 3B), had cell bodies located at the anterior ventral edge of the medulla, adjacent to where its processes entered and coursed through layer M7 and to make elaborations in layer 6 and small, further vertical processes that reached up vertically up to layers M3 and M4 (Figure 3Biii and 3Bvi, arrows). In our EM reconstructions, two cells shared these properties and overlapped around our seed columns (Figure 3Bv).

Mi15 is the only local dopaminergic medulla cell type identified in *Drosophila* so far (Meissner et al. 2019; Davis et al. 2020). Its morphology and connectivity in the medulla have been described in previous EM reconstructions (Takemura et al. 2015; Takemura et al. 2013), and it has a long process that extends into the optic chiasm and tracks photoreceptor axons. Our reconstruction revealed that this process was a locus of photoreceptor input (Figure 3Cii, black arrow), and that overall Mi15 cells were R8-selective, with 91% of their seed column photoreceptor input drawn from R8 cells. The Mi15 cells received 47% of their seed column photoreceptor input within the chiasm (mean of 15/32 synapses per column; Figure 1 – figure supplement 2G), and the R8 cells characteristically formed synapses with Mi15 cells at locations where they also made synapses with R7 cells (Figure 3 – figure supplement 1A).

The columnar cell types Mi1, Mi4 and Mi9 are all integral components of the ON-motion pathway (Strother et al. 2017); prior EM reconstructions have found they receive significant input from R7 and R8 cells, a result confirmed by our new data (Takemura et al. 2015; Takemura et al. 2013; Figure 3 – figure supplement 1B-D). In the identified pale and yellow columns of the medulla FIB-SEM data set, Mi9 was selective for R8 (65% R8 vs 35 R7 input), and 53% of its photoreceptor input originated from pale R8 cells (Takemura et al. 2015). Our data reinforced the observation that Mi9 show a bias for R8 input: 68% of our reconstructed Mi9 input originated from pale seed column R8 cells; the cells in pale columns received 15 and 14 R7/8 synapses, while those in yellow columns received 6 and 4 (Figure 3 – figure supplement 1D).

Central eye R7 and R8 connections with cells projecting to the lobula

The lobula receives diverse inputs from the medulla, including from cell types types required for wavelength-specific phototaxis and learned color discrimination (Gao et al. 2008; Karuppudurai et al. 2014; Melnattur et al. 2014; Otsuna, Shinomiya, and Ito 2014). Many of these cell types express the histamine receptor *ort*, indicating that they, most notably the transmedulla (Tm) cell types Tm5a, Tm5b, Tm5c and Tm20 (Gao et al. 2008), receive direct input from the histaminergic R7 or R8 photoreceptors (Pantazis et al. 2008). We found all of these Tm cell types in our reconstruction, where they were highly connected with the seed column R7 and R8 cells, with a mean of 35 seed column photoreceptor inputs per cell for Tm20, 27 for Tm5a, 23 for Tm5c, and 18 for Tm5b (Figure 4, Figure 4 – figure supplement 1).

The cholinergic Tm5a cell type was the first cell type described to show pale vs yellow selectivity, being preferentially innervated by yellow R7 cells, as revealed by genetic methods and light microscopy (Karuppudurai et al. 2014). This cell type was identified in the medulla FIB-SEM data set (Menon et al. 2019) and was used for identitfing putative yellow columns therein (see Materials and Methods). Its medulla processes are centered on one yellow column, with a single main dendrite from which branches spread laterally reaching some of the neighboring columns in M3, M6 and M8, and an axon terminating in lobula layer 5B manifesting a characteristically hooked final reversal of direction at the axon terminal (Gao et al. 2008; Figure 4A). In both of our yellow seed columns (which we had annotated as being yellow by the lack of innervation by aMe12), we found a Tm5a cell whose seed column photoreceptor input was exclusively from the R7 cell in the home column (Figure 4Aiv). Reassuringly, there were also no Tm5a cells centered on pale columns, or innervated by pale photoreceptors. Thus the localization of Tm5a cells further supported the designation of our four seed columns as being either pale or yellow consistent with the assignment based on the presence or absence of aMe12 vertical processes. One more cell that we refer to as a Tm5a-like had the morphological features of a Tm5a cell, and was selective for yellow seed column input, but from R8 cells (Figure 4 – figure supplement 1A). There was no cell with a similar morphology or connectivity in the medulla FIB-SEM data set, as explored using NeuPrint (Clements et al. 2020). The cell received its R8 input on three different braches of the dendritic arbors,

379 indicating that they were unlikely to have resulted from a reconstruction error (Figure 4 – figure
380 supplement 1Aiv). Overall, our results confirmed the selectivity of Tm5a cells for yellow
381 columns and the reliability of finding R7-selective Tm5a cells in yellow columns.

382 The cholinergic Tm5b cell type is similar to Tm5a, but with ~2-3 vertical main dendrites
383 spanning ~5 columns, from which branches spread laterally in M3, M6 and M8 (Gao et al.
384 2008; Karuppudurai et al. 2014; Meinertzhagen et al. 2009; Figure 4B). A recent analysis of
385 the medulla FIB-SEM data set has proposed that Tm5b cells are pale-specific (Menon et al.
386 2019). Our reconstructions revealed two Tm5b cells that were innervated by pale R7, and not
387 yellow R7 cells (Figure 4B), with only a minor input from seed column R8 cells (19 and 20 R7
388 inputs, vs 7 and 2 R8 inputs, respectively). We also identified 3 more cells with a morphology
389 matching the Tm5b cell type, but innervated by predominantly yellow inputs, which we refer to
390 as Tm5b-like (Figure 4 – figure supplement 1B). In these yellow-specific cells, the input from
391 R8 photoreceptors dominated, with 9.0 R8 inputs (mean, range 4-16), versus 4.7 R7 inputs
392 (mean, range 3-7; Figure 4 – figure supplement 1Biv). In particular, one of these Tm5b-like
393 cells had >20 synapses, and innervated all four seed columns, and was therefore well-covered
394 by our seed-column-focussed reconstructions (Figure 4 – figure supplement 1B).

395 The Tm5c cells are glutaminergic neurons, spanning ~8 columns with single vertical
396 dendrite in the medulla, from which lateral branches spread out in M1, as well as M3 and M6,
397 while the axons terminates near the boundary between lobula layers 5 and 6, often with a
398 branch in layer 4 (Gao et al. 2008; Karuppudurai et al. 2014; Meinertzhagen et al. 2009; Figure
399 4C); one cell axon terminated deep in layer 6 (Supplementary File 2—Tm5c). Our
400 reconstructions confirmed that they were indeed selective for R8 input, as indicated by
401 previous studies (Takemura et al. 2015; Takemura et al. 2013; Karuppudurai et al. 2014; Figure
402 1 – figure supplement 2D). In total, six Tm5c cells were innervated by seed column
403 photoreceptors, and all of them received many synapses from multiple columns, ranging from
404 11 to 44 synapses, consistent with R7/R8 input over a large spatial receptive field. One Tm5c
405 cell was centered on our seed columns, with processes in all of them (Figure 4Cii), and this
406 cell was only targeted by yellow seed column photoreceptors, predominantly R8. This bias

407 towards yellow R8 inputs was maintained over the population (Figure 4Civ). In the identified
408 pale and yellow columns of the FIB-SEM data set, there were two Tm5c cells reliably contacted
409 by R7/8, with > 10 synapses (Takemura et al. 2015; Clements et al. 2020). These two cells
410 also showed a bias for yellow R8 input, with respectively 18 and 11 synapses from yellow R8
411 cells, versus 5 and 0 synapses from pale R8 and R7 combined.

412 The Tm20 cell type is a known columnar target of R8 (Takemura et al. 2015; Takemura
413 et al. 2013; Gao et al. 2008), and the four Tm20 cells located in our seed columns were indeed
414 selectively connected to R8, confirming this previous result, and further revealed no pale or
415 yellow selectivity (Figure 4 – figure supplement 1C, Figure 1 – figure supplement 2D). The
416 Tm20 and Tm5c cell types together received 140 synapses from seed column photoreceptors,
417 making them two of the most targeted cell types (Table 1). We also found one TmY10 cell that
418 received 7 synapses from our seed column photoreceptors (Supplementary File 1—TmY10).
419 In addition we partially reconstructed 10 other Tm cells with a mean of 4.4 photoreceptor
420 synapses per cell. We did not fully reconstruct these lightly innervated Tm cells; Tm subtypes
421 may manifest subtle differences in morphology and connectivity that require multiple examples
422 to distinguish (Jagadish et al. 2014; Gao et al. 2008; Fischbach and Dittrich 1989), which was
423 beyond the scope of our targeted reconstruction.

424 We found one more prominent cell type that was a seed column photoreceptor target
425 projecting to the lobula, that we refer to as the medulla-to-lobula cell type ML1, and we
426 completely reconstructed the morphology of one example (Figure 4D). In addition, we used
427 light microscopy data to explore the anatomy of the ML1 population (Figure 4Dv-vi). These
428 cells projected to the deepest layer of the lobula and also to the adjacent central brain, with
429 cell bodies in the anterior medulla cell body rind (Figure 4Dv), and they were morphologically
430 similar to a putative *ort*-expressing cell identified by Gao et al. (2008; see their Figure S6). ML1
431 dendrites covered ~20 medulla columns with overlap, and as a population covered the entire
432 medulla (Figure 4Dii,vi), ramifying from vertical processes in layers M1-4, and also in M8
433 (Figure 4Diii,v). Unlike the Tm cells, the ML1 axon exited the distal surface of the medulla and
434 traveled anteriorly to enter and terminate in or near lobula layer 6 (Figure 4Diii, v, vi), providing

an alternative pathway connecting the medulla to the lobula. Light microscopy data suggest that a fraction of the cells also formed synapses in the central brain, in the posterior lateral protocerebrum (Figure 4Dvi, arrow). The input to the lobula was non-columnar, and although it was not retinotopically organized, it was spatially organized, with two axon bundles originating in the dorsal and ventral medulla terminated in two locations. Our seed columns contacted four ML1 cells, making an average of 25 synapses per ML1 cell. The cell was exclusively targeted by R8 cells, from both pale and yellow columns (Figure 4Div).

Interneurons connecting central eye R7 and R8 with the central brain

Nearly 10% of the synapses made by the central seed column R7 and R8 photoreceptors were with cells projecting directly to the central brain. Of these, the strongest targets were the MeTu cells, which resemble Tm cells, but instead of sending axons to the lobula, projected to the anterior optic tubercule (AOTU) via the anterior optic tract (Fischbach and Lyly-Hunerberg 1983; Otsuna, Shinomiya, and Ito 2014; Otsuna and Ito 2006; Omoto et al. 2017; Timaeus et al. 2020; Tai, Chin, and Chiang 2021; Figure 5A). Our reconstructions confirmed that MeTu cells were indeed synaptic targets of R7 (Timaeus et al. 2020), and that their photoreceptor input was exclusively from R7 (Figure 5Aiv). In total MeTu cells received 15% of all the synapses made by the seed column R7 cells (Table 1). We found 7 such neurons, and reconstructed the complete morphology of one. Their dendrites overlapped and covered ~20-30 columns (Figure 5Aii), while the axons all targeted the lateral tip of the AOTU (Timaeus et al. 2020; Omoto et al. 2017; Tai, Chin, and Chiang 2021; Figure 5Ai).

The presence of MeTu cells was the largest discrepancy between our list of strong R7 targets and those of the medulla FIB-SEM data set (Clements et al. 2020; Takemura et al. 2015; Figure 1 – figure supplement 2E). In that restricted-volume data set, which focused mainly on columnar cell types, MeTu cells were not identified. We identified in the FIB-SEM data set a previously unidentified Tm cell with a morphology matching the MeTu cells that was an R7 target (Figure 1 – figure supplement 2F). This cell had a connectivity profile that matched reconstructions named Dm7 in the FIB-SEM data set, with prominent input from R7 and Mi15.

We did not identify any Dm7 cells postsynaptic to R7 in our data, and closer inspection of the Dm7 cells in the FIB-SEM data revealed that these putative Dm7 cells were also morphologically very similar to MeTu cells in the medulla. We confirmed other details of the connectivity of our MeTu neurons that were found for the FIB-SEM putative Dm7 neurons (including strong inputs from Dm2 and Mi15 neurons), and therefore we propose that Dm7 cells in the 7-column data set were most likely MeTu cells, resolving the largest (numerical) discrepancy between the data sets, and underscoring the benefit of reconstructing even small circuits in whole-brain EM volumes.

Amongst the photoreceptor target cells projecting to the central brain, we identified a second cell type whose axonal projections follow the anterior axonal tracts of the ML1 neuron, that we refer to here as ML-VPN1 (Figure 5B). The cell bodies were located near the anterior proximal medulla, and, based on our match using light-microscopic data, their dendrites overlapped, with each cell covering tens of columns, collectively covering the medulla (Figure 5Ci-vi). The dendrites ramified along the border of M7 and M8, with vertical processes reaching up and spreading laterally in M3 and again vertically up to M1 (Figure 5Bii-iii, Ciii). Although the ML-VPN1 axons followed the ML1 axonal tract, they innervated the posterior lateral protocerebrum of the ipsilateral hemisphere, in a region just posterior to the optic glomeruli, and did not form synapses in the lobula (Figure 5Bi, Ci). The ML-VPN1 cells were almost exclusively targeted by the pale R8 cells, with 8.7 pale R8 inputs per cell (mean, range 5-14), and just one yellow R8 input across the three cells connected to our seed column photoreceptors (Figure 5Biv). Light microscopic analyses of co-labelling of ML-VPN1 neurons with either yellow R8 axons (Figure 5Cvi) or pale R8 axons (Figure 5 – figure supplement 1) supported the pale preference seen in the EM data: ~90% of columns in which ML1 arbors and photoreceptors appeared to overlap were pale. Together, our data indicate that ML-VPN1 neurons have a strong bias for pale R8 input.

The aMe12 cells were also R8 targets, and the two contacted cells received 15 and 11 R8 synapses, and 2 and 1 R7 synapses, respectively (Figure 1D, Eiii, Supplementary File 1—aMe12 outgoing). Their axons also targeted the posterior lateral protocerebrum, although in

491 slightly different locations to ML-VPN1, but they did so to both hemispheres (Figure 5D). In
492 addition, aMe12 cells also projected to the mushroom body calyces of both hemispheres, as
493 well as to the contralateral and ipsilateral accessory medulla and superior clamp (Figure 5Di,
494 Dii). All three aMe12 cells shared a characteristic branching pattern, but only one of them
495 additionally innervated the contralateral accessory medulla (Figure 5Dii). The aMe12 cell type
496 is present in the hemibrain connectome, where it is also a strong input to γd Kenyon cells, and
497 both cells reach the contralateral accessory medulla (Li et al. 2020).

498 There were 5 additional tangential cells projecting to the central brain (Mt-VPNs) that
499 were targeted by the seed column photoreceptors, collectively receiving 25 synapses (1
500 neuron in Figure 5E, others in Figure 5 – figure supplement 2). The most targeted cell, which
501 we refer to as medulla tangential visual projection neuron (Mt-VPN1), had processes in layer
502 M7, with branches reaching up into layers M5-M6, where it received inputs from both seed
503 column yellow R7s, and projected an axon to the posterior lateral protocerebrum (Figure 5E).
504 To check whether it was a preferential target of yellow R7 cells, we traced Mt-VPN1 outside
505 the seed columns and found that across 20 columns it received input from 13 yellow R7 cells,
506 and 7 pale R7 cells, indicating it is selective for R7. Our 65% threshold for selectivity applies
507 to the home columns that equally sample pale and yellow columns, but across 20 columns,
508 these data did not indicate yellow R7 selectivity, as 62% of all columns were yellow. The
509 remaining tangential cells included a match to a known octopaminergic neuron (OA-AL2i3;
510 Busch et al. 2009; Figure 5 – figure supplement 2A). This cell had processes in the distal
511 medulla in layers M1-M2 as well as processes reaching out into the chiasm which received
512 photoreceptor input (Figure 5 – figure supplement 2Aii-iii), and an axon that ipsilaterally
513 innervated the inferior and superior posterior slope, and the flange (Figure 5 – figure
514 supplement 2Ai). This cell was one of the rare cell types that formed synapses onto
515 photoreceptors, making 5 synapses onto the R7 and R8 cells, but only in one yellow column
516 (Supplementary File 1—Mt-VPN). The remaining Mt-VPN cells were very lightly innervated by
517 the seed column photoreceptors in multiple (Figure 5 – figure supplement 2Cii) and single
518 columns (Figure 5 – figure supplement 2 Bii, Dii), but may prove to integrate large numbers of

519 photoreceptor inputs as they covered many medulla columns. Collectively they innervated the
520 ipsilateral superior posterior slope, accessory medulla, and lobula, and in both hemispheres
521 the inferior posterior slope and lobula plate (Figure 5 – figure supplement 2B-D), and so
522 revealed multiple pathways for transmitting direct photoreceptor signals into the central brain.
523
524 Synaptic interconnection between R7 and R8 in the DRA and their connections to different
525 medulla cell types
526 So far, no prior studies have generated EM-based connectomic data for targets of the
527 polarization-sensitive photoreceptors in the DRA region of the *Drosophila* eye. This section
528 first presents DRA photoreceptor targets also found in the central reconstructions (Figure 6),
529 followed by modality-specific Dm cell types strongly connected to DRA inner photoreceptors
530 while avoiding contacts with non-DRA counterparts (Figure 7), visual projection neurons
531 directly connecting the DRA with the central brain (Figure 8), and finally more weakly
532 connected medulla cell types only found in the DRA region of the medulla (Figure 9).
533 As in the central region of the medulla, R7-DRA and R8-DRA axons are strongly
534 interconnected via chemical synapses. The absolute number of R7-DRA synapses onto R8-
535 DRA cells are very similar to the numbers found in the central seed columns (13.7 mean, range
536 10 – 16) accounting for 4.9% (41/837) of total R7-DRA output (as compared to 4.8% (57/1187)
537 in central seed columns; Figure 6 – Figure supplement 1A, Supplementary File 1). Similarly,
538 the R8-DRA synapse numbers onto R7-DRA cells are also comparable (36.0 mean, range 33
539 - 38 in the DRA compared to 39.0 mean, range 36 – 46 in the central eye; Figure 6 – Figure
540 supplement 1B, Supplementary File 1). However, due to the overall reduced number of R8-
541 DRA presynapses, the relative proportion of R8-to-R7 synapses is substantially increased
542 (21.6% of total R8-DRA outputs (108/499), compared to 10.3% (157/1520) in the central
543 region; Figure 6 – Figure supplement 1C, Supplementary File 1). As in the central region of
544 the medulla, a considerable proportion of the DRA seed column R8-to-R7 synapses (15%,
545 16/108, mean 5.3 synapses per cell, range 3-8), and R7-to-R8 synapses (48%, 19/41, mean

546 6.3 synapses per cell, range 4-8) were found in the axonal projection outside the medulla
547 (Figure 6Ai, arrow).

548 The connectivity between R7-DRA and/or R8-DRA and several lamina and medulla cell
549 types is comparable to their connectivity of central column photoreceptors, most notably L1,
550 L3, and Mi1 (Figure 6 – figure supplement 2A-C), whereas others manifest slight differences
551 in their connectivity between these two seed-column regions. Dm2 cells are primarily R8
552 targets in central eye columns, but in the DRA, the Dm2 cells receive similar numbers of R7-
553 DRA and R8-DRA synapses (7.0 mean, range 5 – 10 for R7-DRA, 9.0 mean, range 5 -15 for
554 R8-DRA synapses per column; Figure 6Bi-iii, Supplementary File 1). These differences in
555 connectivity of Dm2 between the DRA and the central region confirm light microscopic findings
556 proposing DRA-specific differences in Dm2 photoreceptor connectivity (Sancer et al. 2020).
557 Dm9 cells in the DRA also are prominent synaptic target of both inner photoreceptors, while
558 providing strong synaptic feedback into them (Figure 6C, Table 3, 4). On average, Dm9
559 receives 31.7 (mean, range 26 – 38) R7-DRA synapses per column, corresponding to 11.3%
560 (95/837) of R7-DRA's total output (Supplementary File 1). As in the central region, R8-DRA
561 also is more strongly connected to Dm9, providing an average of 38.3 (mean, range 36 – 43)
562 synapses, corresponding to 23% (115/499) of its total output. Strikingly, Dm9 and R7-DRA
563 together account for 44.6% (223/499) of all R8-DRA output synapses (Supplementary File 1).
564 The absolute number of R7 and R8 inputs to Dm9 per seed column are reduced in DRA seed
565 columns, when compared to central seed columns (111.2 mean, range 102 – 123 for the
566 central eye and 70 mean, range 62 – 81 for the DRA; Supplementary File 1). The distribution
567 of R8 synapses onto Dm9 is different in the DRA, with the greatest density in layer M6,
568 reflecting the DRA-specific morphology of R8 cells (Figure 6Ci,ii). Past light microscopic
569 studies suggested that marginal Dm9 cells might receive both DRA and non-DRA inputs
570 (Sancer et al. 2020), thereby potentially mixing polarization and color information (Heath et al.
571 2020). To verify these findings, we reconstructed R7 and R8 photoreceptors of three non-DRA
572 columns which are interconnected with one of the Dm9 cells in the DRA. By partially annotating
573 photoreceptor synapses from these three non-DRA columns as well as from two DRA columns

and the same Dm9 cell, we found that marginal Dm9s indeed receive input from both color and polarized light sensitive photoreceptors (Figure 6Cvi).

As in the central region of the medulla, Mi15 cells are also a significant photoreceptor target in the DRA where they receive synapses from both R7-DRA and R8-DRA (7 mean, range 4 – 9 for R7-DRA and 6 mean, range 3 – 10 for R8-DRA; Figure 6Di-iii, Supplementary File 1). As was the case for Dm2 cells, Mi15 receive more balanced inputs from both photoreceptor types in the DRA seed columns, while showing a strong preference for R8 inputs from the central seed columns. Unlike in central columns, where Dm11 cells represent a significant R7 target, this cell type was found in only one DRA seed column, receiving minor and again balanced input from both R7 and R8 in the DRA region (4 from R7-DRA and 8 from R8-DRA; Figure 6 – figure supplement 2D, Supplementary File 1). Only two additional columnar cell types appear to be connected to photoreceptors with more than 2 synapses throughout all three DRA seed columns - Mi9 and Tm20. Both cell types are specifically connected to R8-DRA cells, although much more weakly connected than their central counterparts (Mi9: 4 mean, range 0 – 9 for R8-DRA and 6.5 mean, range 0 – 14 for the central eye R8; Tm20: 5.3 mean, range 4 – 8 for R8-DRA and 33 mean, range 30 – 35 for the central eye R8; Supplementary File 1). Mi9 cells receive only 4 (mean, range 0 – 9) synapses per seed column from R8-DRA (and none from R7-DRA) but otherwise showed no obvious morphological differences compared to their central eye counterparts (Figure 6 – figure supplement 2E, Supplementary File 1). Interestingly, Tm20 cells were the only Tm cell type connected to DRA inner photoreceptor cells present in all DRA seed columns with 5.3 (mean, range 4 – 8) synapses per column from R8-DRA (and zero from R7-DRA; Figure 6Ei-iii, Supplementary File 1). Only one other Tm cell (referred here as Tm5-like) was found to be strongly connected, with 12 synaptic inputs from both R7-DRA and R8-DRA inputs, albeit only being present in one of the three DRA columns (Figure 6 – figure supplement 2F).

Dm8-like photoreceptor targets in the DRA region

The strongest target of R7-DRA cells is the Dm-DRA1 cell type (Sancer et al. 2019). A total of 20 Dm-DRA1 cells receive on average 70.1 (mean, range 66 -77) synapses per DRA seed column, corresponding to 25.3% (212/837) of total R7-DRA output (Supplementary File 1). No synaptic inputs from R8-DRA were detected in the three seed columns, despite R8-DRA terminating in close proximity of R7-DRA (Figure 7A). Consistently, synaptic inputs from R7-DRA to Dm-DRA1 are tightly restricted to the proximal edge of layer M6 where R8-DRA are not present (Figure 7Ai, Aii). Although Dm-DRA1 cells have been proposed to be the DRA-specific equivalents of Dm8 (Courgeon and Desplan 2019), we never detected vertical protrusions resembling Dm8 'home columns' in Dm-DRA1 cells. As previously described, Dm-DRA1 cells have deep projections that leave the DRA and stratify below layer M6, and these do not receive strong photoreceptor input (Figure 7Aiii, compare light-microscopic clone in 7Aiv). Few synapses were found in non-DRA columns close to the DRA (Figure 7 – figure supplement 1A, Supplementary File 1). Only one of these R7 cells made a comparably high number (11 synapses) onto the posterior Dm-DRA1 cell. This photoreceptor could be an R7-DRA cell (despite R8 in the same column terminating in M3), since inner photoreceptors choose DRA fates independently. As a result, low numbers of such 'mixed' ommatidia can be found at the DRA/non-DRA boundary of virtually every fly retina (Wernet et al. 2003; Wada 1974b). Outside the DRA, deep projections of Dm-DRA1 cell branches didn't show any clear preference for occupying either pale or yellow columns (Figure 7 – figure supplement 2).

As in the case of Dm8 cells, we took the additional step of identifying all the DRA photoreceptor inputs to three fully traced Dm-DRA1 cells, in order to gain a better understanding of the synaptic connectivity pattern (or distribution) between DRA photoreceptors and these cell types (Figure 7B). Each of the fully traced Dm-DRA1 cells is connected to an average of 9 (mean, range 8 – 10) neighboring R7-DRA cells, receiving on average a total of 94 synapses (mean, range 66 – 112) from R7-DRA, but very few connections from R8-DRA cells (only observed for the posterior DmDRA1 where 2 R8-DRA cells form 3 respectively 2 synapses; Figure 7Bi, Supplementary File 1). Synapse numbers across the cells' DRA backbone resembled a ~50 μm contiguous stretch of inputs from neighboring

columns, with stronger input in the center, but without a single, obvious home column (Figure 7Bii, Figure 7 – figure supplement 3).

R8-DRA Photoreceptors from the three seed columns made an average of 34.3 (mean, range 19 – 44) synapses with a total of 9 different Dm-DRA2 cells (Sancer et al. 2019; Supplementary File 1). Based on our prior descriptions, and confirmed here, each Dm-DRA2 cell has multiple characteristic vertical projections (Figure 7Ci), whose length is highly variable, but are on average much longer than the singular vertical processes observed in Dm8 home columns. Dm-DRA2 vertical projections are also a striking feature of light microscopic clones (Figure 7Civ), and they received synaptic input from R8-DRA cells (Figure 7Cii, Ciii). As with the Dm-DRA1 cells, we fully reconstructed three Dm-DRA2 cells so as to quantify the pattern of their photoreceptor inputs. They are innervated by an average of 9.3 (mean, range 8 – 11) R8-DRA photorecreptors and receive minor inputs from R7-DRA (3.7 mean, range 3 – 4 R7-DRA per DmDRA2 with an average of 5.3, range 3 – 7 synapses; Figure 7D, Supplementary File 1). The distribution of R8-DRA inputs into each Dm-DRA2 cell again resembled a ~50 μm contiguous stretch with a peak in its center and without an obvious home column (Figure 7Di, Dii). Thus, both the Dm-DRA1 and Dm-DRA2 cell types directly integrate photoreceptor input over multiple columns, with a dominant input at the center of their receptive field. In agreement with previous light microscopic data (Sancer et al. 2019), both Dm-DRA1 and Dm-DRA2 skeletons heavily overlap with each other, all along the DRA (Figure 7Ei, Eii). The population of all Dm-DRA1 cells connected to the same R7-DRA seed photoreceptor (8.3 mean, range 6 - 11) on average spans on average 17 DRA columns (mean, range 13 - 19), which can correspond to just under half the DRA. In comparison, both the number of Dm-DRA2 targets of one single seed R8-DRA photoreceptor was lower (3.3 mean, range 2 – 5 Dm-DRA2 cells per column), and the DRA area covered by them was a smaller span of the DRA, with an average 0f 10.7 columns (mean, range 10 -12). It appears therefore that more Dm-DRA1 cells than Dm-DRA2 cells populate the DRA region of the medulla, given that these cells contact similar numbers of DRA inner photoreceptors (9.0 versus 9.3, respectively – see above). Finally, direct comparison of inputs into Dm-DRA1 and Dm-DRA2 from the same location along

657 the DRA reveals a separation of DRA-R7 and R8-DRA synapses into different sublayers of M6
658 (Figure 7Eiii), corroborating light microscopic observations (Sancer et al. 2019).
659
660 Visual projection neurons directly connecting R7-DRA to the central brain
661 The second most prominent R7-DRA target after Dm-DRA1 cells is a previously
662 unidentified cell type that we refer to as MeTu-DRA (Figure 8Ai). These cells are modality-
663 specific, as they exclusively receive R7-DRA photoreceptor inputs, but get no input from R8-
664 DRA. Both the reconstructed skeletons, as well as the corresponding light microscopic clones
665 of MeTu-DRA cells (Figure 8Aii), feature long axons projecting to the small unit of the AOTU,
666 identifying them as specialized MeTu cells (Omoto et al. 2017; Panser et al. 2016; Otsuna,
667 Shinomiya, and Ito 2014; Tai, Chin, and Chiang 2021). They closely resemble cells described
668 in the DRA region of optic lobes from larger insects (Pfeiffer and Kinoshita 2012; el Jundi,
669 Pfeiffer, and Homberg 2011). A total of 30 reconstructed MeTu-DRA cells receive an average
670 of 61.3 (mean, range 49 – 85) R7-DRA synapses per seed column, corresponding to 22.0%
671 (184/837) of the total R7-DRA output (Figure 8Aiii and 8Aiv, Supplementary File 1). As in the
672 case of Dm-DRA1, synapses from R7-DRA onto MeTu-DRA cells are restricted to the
673 photoreceptor tips at the proximal edge of layer M6 (Figure 8Aiv). Outside the DRA region,
674 MeTu-DRA cells form additional processes innervating the dorsal medulla (Figure 8Av).
675 However, these processes appear to avoid non-DRA photoreceptor contacts by stratifying
676 below M6, in a manner reminiscent of the Dm-DRA1 deep projections (Sancer et al. 2019).
677 Again, these processes show no obvious preference for pale or yellow columns (Figure 8 –
678 figure supplement 1A). To confirm their modality-specific connectivity to photoreceptors of the
679 DRA and not the central region, we visualized single MeTu-DRA cell clones in the DRA and
680 indeed found their photoreceptor contacts were always restricted to the DRA (Figure 8Avi).
681 The medulla dendrites of all MeTu-DRA skeletons connected to the same R7-DRA seed
682 photoreceptor (11.3 mean, range 8 – 16) widely overlap along the DRA, covering 15 DRA
683 columns on average (mean, range 12 – 17; Figure 8vii). Since the axons of the central region
684 MeTu cells projected to a discrete subdomain of the small unit of the AOTU (Figure 5Ai), we

685 assessed whether they intermixed with MeTu-DRA terminals. Interestingly, both MeTu-DRA
686 and the other MeTu cells we reconstructed from centrally located seed columns, terminate in
687 separate, adjacent AOTU compartments (Figure 8vii, inset).

688 Besides the MeTu-DRA cells we found one additional, previously uncharacterized cell
689 type directly connecting the DRA with the central brain, which we refer to as VPN-DRA.
690 Individual skeletons of EM-reconstructed neurons, as well as light microscopic clones for a
691 corresponding cell type we identified, populate the DRA and send axonal projections to a
692 specific central brain region, the posterior lateral protocerebrum (PLP; Figure 8Bi, Bii). There
693 are 6 VPN-DRA cells with >2 synapses contacted by the DRA seed columns and they received
694 an average of 10 (mean, range 6 – 13) DRA synapses per seed column (corresponding to
695 3.6%, 30/837, of total R7-DRA output), with no input from R8-DRA cells (Figure 8Biii, Biv,
696 Supplementary File 1). The backbone of VPN-DRA skeletons follows the DRA, while smaller
697 branches infiltrated non-DRA columns (Fig 8Bv). Double labeling of a driver line with apparent
698 VPN-DRA expression with photoreceptor neurons suggests that VPN-DRA cells might be
699 modality-specific, although fine processes can be seen in close contact with non-DRA
700 photoreceptors as well (Figure 8Bvi). VPN-DRA cells form an overlapping group of neurons
701 covering the entire DRA region of the medulla of a given hemisphere with projections to the
702 PLP (Figure 8Bvii). Some morphological heterogeneity appears to exist within the VPN-DRA
703 population, with some cells having additional processes, both in the medulla, as well as in the
704 central brain and a different cell body position (Figure 8 – figure supplement 1B), indicating
705 that VPN-DRA cells might consist of distinct subtypes.

706

707 Other newly identified photoreceptor targets in the DRA region of the medulla

708 We identified two previously uncharacterized DRA cell types that received
709 photoreceptor input in the seed columns. The first cell type, which we named MeMe-DRA,
710 consists of two large heterolateral medulla cells that connected the DRA areas of both
711 hemispheres (Figure 9Ai), crossing the central brain without forming synapses there. These
712 cells resemble the polarization-sensitive MeMe1 cells characterized in locusts (el Jundi,

713 Pfeiffer, and Homberg 2011; El Jundi and Homberg 2010), and we were able to match their
714 morphology to that of a cell type using light microscopy (Figure 9Av). We reconstructed two
715 MeMe-DRA cells (and could not find additional ones), both being exclusively innervated by R7-
716 DRA cells in all three seed columns, receiving on average 12.0 (mean, range 0 – 21) synapses
717 per seed column, corresponding to 4.9% of total R7-DRA output (Figure 9Aiii-iv,
718 Supplementary File 1). The putatively dendritic part of a MeMe-DRA skeleton (located within
719 the hemisphere that contained the cell body) follows the DRA (Figure 9Aiv) and appears to
720 receive DRA modality-specific photoreceptor input, based on light microscopic labeling, with
721 processes reaching layer M6 exclusively in the DRA region of the medulla (Figure 9Av).
722 Interestingly, the DRA areas contacted by a given cell is flipped along the anterior-posterior
723 axis between the two hemispheres, so that the anterior half of one is directly connected to the
724 posterior half in the other hemisphere, and vice versa (Figure 9Avi).

725 Another newly identified group of cells we found as DRA photoreceptor targets is a
726 population of morphologically diverse Mti cells covering the dorsal medulla (Figure 9B,C,
727 Figure 9 – figure supplement 1), for which we also found light microscopy matches. A total of
728 10 of these Mti-DRA cells are all innervated exclusively by R7-DRA, but fall into two distinct
729 morphological populations, named here Mti-DRA1 (Figure 9Bi-Bv) and Mti-DRA2 (Figure 9Ci-
730 Cv). A total of six Mti-DRA1 cells have ventrally located cell bodies (Figure 9Bi) and receive
731 on average 17.3 (mean, range 13 – 21) synapses per seed colum, corresponding to 6.2% of
732 total R7-DRA output (Figure 9Biii, Supplementary File 1). Individual reconstructed Mti-DRA1
733 skeletons form a backbone that covers the DRA columns with short processes leaving the
734 DRA region (Figure 9Biv - 9Bv). Mti-DRA2 cells have dorsally located cell bodies (Figure 9Ci)
735 and are more weakly connected to R7-DRA photoreceptors, with four Mti-DRA2 neurons
736 making 5 (mean, range 3 – 8) synapses per seed column, corresponding to 4.4% and 1.8% of
737 R7-DRA total output, (Figure 9Cii, Ciii – figure supplement 1, Supplementary File 1). The
738 backbones of Mti-DRA2 skeletons also cover the DRA but form longer processes extending
739 further ventrally (Figure 9Civ, 9Cv).
740

741 Comparison of R7/R8 connectivity in the central eye versus the DRA region

742 Taken together, our reconstructions of the synaptic targets of R7 and R8
743 photoreceptors specialized for color versus polarization vision revealed specific stereotypical
744 similarities, as well as striking differences. The pattern of connectivity between R7 and R8
745 terminals from the same ommatidium, and with Dm9, was highly congruent in columns
746 processing color and polarization, indicating that the mechanisms of lateral inhibition between
747 photoreceptors and gain modulation by Dm9 can serve both modalities (Schnaitmann et al.
748 2018; Weir et al. 2016; Heath et al. 2020; Figure 10A).

749 A second striking similarity was the location of synapses located outside the medulla
750 (Figure 1 – figure supplement 2G). In both the central and DRA columns, more than half of the
751 R7 to R8 synapses and the inputs to the lamina cells L1 and L3 were made outside the medulla
752 (Figure 1 – figure supplement 2G, Figure 2 – figure supplement 1, Figure 6 – figure supplement
753 1A,B). In both cases, the strongest lamina monopolar target was L3, receiving 80% of its R7/R8
754 inputs within the chiasm (Figure 2 – figure supplement 1C, Figure 6 – figure supplement 1B).
755 L3 is known to contribute to color processing through innervation of Dm9, Tm20, and Tm5c
756 (Takemura et al. 2015), in addition to the ON and OFF pathways computing motion (Silies et
757 al. 2013). These lamina monopolar cells, combined with weaker connections from R7/R8 onto
758 C2 cells (Figure 2 – figure supplement 1D), provide a source of cross-talk between channels
759 informing color-specific (R7/R8) and motion-sensitive (R1-6) channels (Tuthill et al. 2013),
760 which previously had been believed to operate separately (Heisenberg and Buchner 1977;
761 Yamaguchi et al. 2008). Subsequent data seemed to contradict these findings, (Wardill et al.
762 2012; Schnaitmann et al. 2013; Wernet et al. 2012; Pagni et al. 2021), and our reconstructions
763 provide further support for the convergence of these channels at early stages within the optic
764 lobe circuitry (Takemura et al. 2013).

765 When comparing connections to Dm cell types (Figure 10B), we confirmed that in the
766 DRA, both R7 and R8 cells connect to their own amacrine-like cell type (the Dm-DRAs), as
767 previously proposed using light microscopy (Sancer et al. 2019). Such connections never
768 occur in the central seed columns, where only R7 connects to the amacrine cell type Dm8. As

for central R8, the much smaller Dm2 cells are the strongest biased/specific target of R8. Since recent studies point towards Dm-DRA1 (as target of R7-DRA) and Dm8 cells being developmentally similar (Courgeon and Desplan 2019), it remains to be seen whether Dm-DRA2 represent a duplication of Dm8 fates in the DRA (where orthogonal e-vector orientations presumably are processed downstream of R7 and R8). Alternatively, these cells could be developmentally similar to Dm11 cells (sharing morphological similarities, like numerous, long vertical projections per cell), which we identify here as R7 target cells in the central seed columns, while being only present in one of the three DRA seed columns (Figure 6 – figure supplement 1E).

When comparing R7/R8 connections to Mi cell types, it becomes apparent that many of these connections (Mi1, Mi4, Mi9) are much weaker or completely missing in the DRA region (Figure 10C). Given their important role in the computation of motion (Strother et al. 2017), this could indicate more strict separation between computations of motion and polarization, as compared to motion and color. In contrast, Mi15 cells – for which no role in motion vision has been reported - appear to be targeted by both central and DRA inner photoreceptors. The role of Mi15 remains yet to be determined, but its dopaminergic fate (in addition to other transmitter/modulator signatures) suggests a modulatory role (Davis et al. 2020). We reconstructed morphologically different Mti cells both from central and DRA columns, which might collect input from large numbers of photoreceptors. While the Mti cells are strong R8 targets in the central columns (Figure 3A,B), they are targets of R7 in the DRA (Figure 10C). Interestingly, R7-DRA photoreceptors provide significantly stronger input per seed column into Mti-DRA cells, which could be due to the relatively low number of DRA ommatidia per hemisphere (42, as determined here from FAFB).

One of the most striking results of our reconstruction is the virtually complete lack of lobula targeting neurons receiving photoreceptor connections in the DRA region (Figure 10D). While our reconstruction identifies and confirms the Tm5a, Tm5b, Tm5c, and Tm20 cells as known targets of central R7 or R8 (Meinertzhagen et al. 2009; Gao et al. 2008; Melnattur et al. 2014), the lack of synaptic connections with these cell types in the DRA corroborates the

797 results of a previous light microscopic study (Sancer et al. 2020). In addition to Tm cells, we
798 identify the new cell type ML1, also connecting the medulla to the lobula but without the precise
799 retinopy of the Tm cell arrays and with additional branches in the central brain (Figure 10Dii).
800 This lack of Tm and ML1 connectivity in the DRA is reflected in the overall lower number of
801 R8-DRA synapses (Table 3).

802 Central R7 and R7-DRA cells are strongly connected to different classes of MeTu cells,
803 which form long axons terminating in spatially segregated areas of the small unit of the AOTU
804 (Figure 10E). Previous studies proposed that different kinds of visual information may be
805 processed by distinct parallel pathways leading towards the central brain via the AOTU
806 (Otsuna, Shinomiya, and Ito 2014; Omoto et al. 2017; Timaeus et al. 2020; Tai, Chin, and
807 Chiang 2021). Our reconstructions support this hypothesis, showing different target regions for
808 these 2 putative MeTu types, and functional measurements confirm that the target area of
809 MeTu-DRA cells shows polarization-sensitive responses (Hardcastle et al. 2021). While some
810 studies suggest a potential role of central MeTu cells in wavelength-specific behaviors
811 (Otsuna, Shinomiya, and Ito 2014), the full diversity of the MeTu subtypes and the exact role
812 of specific subtypes remain incompletely understood.

813 Besides the AOTU, cell types postsynaptic to central eye and to DRA ommatidia both
814 project directly to the PLP, but otherwise show little overlap in the central brain areas they
815 project to (Figure 10F). The additional contacts of DRA projection neurons are focused to the
816 lateral horn and the contralateral medulla, while the central eye projection neurons innervate
817 widely across the central brain, including the mushroom bodies, and the contralateral lobula
818 plate. A key modality-specific adaptation of the visual projection neurons is the dominance of
819 R8 input in the central eye, and R7 in the DRA.

820

821 **Discussion**

822 Our systematic reconstruction of all synaptic inputs and outputs of identified,
823 functionally specialized *Drosophila* R7 and R8 photoreceptors (pale, yellow and DRA),
824 provides a complete and comprehensive catalog of the first steps of the color and polarization

pathways, from which all of the computations of the dependent behaviors stem. These data revealed core connectomic motifs shared across columns types (Figure 10A-C), multiple new photoreceptor targets, and uncovered additional cell types as being connected to specific photoreceptor subtypes conveying specific color and polarization information to the central brain (Figure 10E,F).

R7 and R8 connections outside the medulla neuropil

We confirmed previously reported synaptic partners of R7 and R8 photoreceptors in the central medulla (Figure 1-supplement 2) and also identified new photoreceptor targets, discussed below. As prior reconstructions were incomplete (Takemura et al. 2015), it was unclear whether the unidentified connections were mainly onto new target neurons, or represented more connections onto known cell types. Our reconstructions revealed both types of omissions. One functionally important set of missed connections are the synapses between R7 and R8 cells from the same central and DRA ommatidia, which we found to be stronger than previously reported (Takemura et al. 2015; Takemura, Lu, and Meinertzhagen 2008), due to significant numbers of synapses outside the medulla. These strong reciprocal connections likely contribute to color-opponent responses seen in central R7 and R8 terminals (Schnaitmann et al. 2018) and the polarization-opponent signals measured from DRA photoreceptors (Weir et al. 2016). Our reconstructions also support a larger scale opponent process mediated by multi-columnar Dm9 cells (Heath et al. 2020), which also formed some synapses outside the medulla neuropil.

Other cell types also received inner photoreceptor input outside the medulla, notably the lamina monopolar cells L1 and L3, indicating that chromatic comparisons arising from R7 and R8 may feed into the motion vision pathway. This identifies a new site for interplay between the ‘color’ and ‘motion’ pathways; such interplay is thought to also occur in the opposite direction, for example between Mi1, a prominent motion pathway neuron, and Dm8 cells, a major R7 target (Pagni et al. 2021). Together, these observations suggest that synapses in an

852 unexpected location, outside the main synaptic layer of the medulla, could play a significant
853 role in early visual processing.
854
855 Newly identified targets of central versus DRA R7 and R8
856 We identified several cell types either not previously described, or not known to be
857 connected to inner photoreceptors, thus setting up a clear expectation that these cells should
858 contribute to color or polarization vision. We identified ML1 cells as a new, major target of R8,
859 a cell type that connects medulla and lobula via a previously unknown, non-columnar pathway
860 (Figure 4D, Figure 10 Aii). Due to their central brain synapses, ML1 cells might be best
861 considered as a class of visual projection neurons that also have arbors in the deepest layer
862 of the lobula. Our identification of multiple Tm cell types post-synaptic to central R7 and R8
863 support the proposals of previous studies that chromatic signals are further processed in the
864 lobula (Lin et al. 2016; Gao et al. 2008). Whether these Tm neurons and ML1 cells have
865 common targets in the lobula, feed into shared central pathways or contribute to separate
866 channels will require further study; we note that the lobula arbors of the Tm and ML1 cells are
867 mostly in different layers arguing against direct synaptic interactions between the cells. By
868 contrast, cells projecting to the lobula are strikingly absent in DRA columns (Figure 10D).
869 In the central medulla, we find, for the first time in an EM study, strong synaptic
870 connections between R7s and MeTu cells that project to the AOTU (Figure 11Ai), confirming
871 previous claims based on light microscopy (Timaeus et al. 2020). This finding may reconcile
872 disparate observations, such as a role in wavelength-specific phototaxis for cells matching
873 MeTu morphology (Otsuna, Shinomiya, and Ito 2014), as well as measurements of color-
874 sensitive signals in the AOTU (Mota et al. 2013) of bees. Previous anatomical studies
875 partitioned MeTu cells into distinct subclasses that terminate in discrete subdomains of the
876 AOTU (Omoto et al. 2017; Timaeus et al. 2020; Tai, Chin, and Chiang 2021). Here we identified
877 modality-specific MeTu-DRA cells that only integrate from the polarization-sensitive R7-DRA
878 photoreceptors, while avoiding synaptic contacts with color-sensitive pale or yellow R7s. We
879 find that MeTu and MeTu-DRA cells target adjacent subdomains within the small unit of the

AOTU (Figure 10E), in agreement with proposals that parallel channels convey different forms of visual information from the eye to the central complex via the AOTU (Hardcastle et al. 2021; Hulse et al. 2020; Timaeus et al. 2020; Omoto et al. 2017).

The reconstruction of DRA photoreceptor targets identified both Dm-DRA cell types that were described using light microscopy (Sancer et al. 2019), and confirmed their specific connectivity within layer M6: Dm-DRA1 cells are connected almost exclusively to R7-DRA cells, whereas Dm-DRA2 cells are R8-DRA targets. Since R7-DRA and R8-DRA, at each location of the DRA, maximally respond to orthogonal orientations of polarized light, we therefore expect that Dm-DRA1 and Dm-DRA2 process orthogonal e-vector orientations, that are spatially averaged by pooling over ~9 neighboring ommatidia (Weir et al. 2016). Our data also revealed additional DRA pathways into the PLP in the central brain via VPN-DRA cells, as well as to the contralateral DRA, via MeMe-DRA cells (Figure 10F). Such interhemispheric connections have been demonstrated in larger insects (el Jundi, Pfeiffer, and Homberg 2011; Labhart 1988), but not in *Drosophila,* and their synaptic input was not known. Interactions between the DRAs of the two eyes remain poorly understood, although interocular transfer was shown to occur in desert ants navigating only when using celestial polarization, but not when using landmarks (Wehner and Muller 1985). The MeMe-DRA neurons identified here now provide one potential substrate for understanding this phenomenon at a cellular and synaptic level.

Cell types distinguishing between pale and yellow inputs

The fly's retinal mosaic can support circuits with different chromatic sensitivities by selective sampling of pale and yellow photoreceptors. For example, cells contrasting pale and yellow R7 input would be expected to have high chromatic sensitivity around ~350 nm, where the spectral sensitivity of Rh3 and Rh4 overlap (Salcedo et al. 1999). Our reconstructions revealed several cases of connectivity patterns that could support such selective sampling. For R7, these included two cell types previously reported to be pale/yellow selective: Tm5a for yellow R7 input (Karuppudurai et al. 2014), and Tm5b for pale R7 (Menon et al. 2019; Figure

11Bi). By, for the first time, completely reconstructing several Dm8 cells (Figure 2C), we found that Dm8 neurons were most highly innervated by R7 in their home columns, with equal sampling of pale and yellow R7 input in the surrounding columns, an organization consistent with pale and yellow Dm8 subtypes (Menon et al. 2019, Courgeon and Desplan 2019). Unlike in the DRA, there were no cells projecting to the central brain that were substantial targets of R7. Examining the encoding of chromatic signals in Tm5a/b and Dm8 cells, and their other synaptic partners, is therefore a promising avenue for addressing the open question of how, or if, UV information from yellow ommatidia is processed differently from UV signals downstream of pale R7 cells.

We found more pale/yellow selective cells among the R8 targets. Two visual projection neurons were newly identified as selective for pale R8 input, the aMe12 and ML-VPN1 cells. ML-VPN1 provides input to the PLP, while aMe12 has presynaptic sites in the accessory medulla, the PLP, and the mushroom body, where it provides input to γd Kenyon cells (Li et al. 2020; Scheffer et al. 2020). These connectivity patterns suggest roles in circadian entrainment and learning and memory, respectively (Figure 11Bii). *Drosophila* pale R8 cells are most sensitive to blue wavelengths (Sharkey et al. 2020; Salcedo et al. 1999; Schnaitmann et al. 2018; Heath et al. 2020), and the projections of aMe12 and ML-VPN1 demonstrate that blue light is processed and used by the central brain within one synapse. Little is known about the central processing of color in *Drosophila* (Longden 2016), but the detection of blue light plays an important role in the circadian avoidance of bright light (Lazopulo et al. 2019). Flies can also learn to discriminate between large areas of blue and green light and a group of visual projection neurons have been reported to provide to provide input to γd Kenyon cells and be required for this ability (Vogt et al. 2014).

While near perfect specificity for pale versus yellow inputs appears to be limited to a few cell types, several strongly connected cell types show strongly biased inputs: For example, Dm2 favors pale over yellow R8 (60:15), and Tm5c favor yellow over pale R8 (103:20) a result that corroborates and extends the findings of the 7-column medulla connectome. Individual cells, in particular Tm20 neurons, that span just one column, are also constrained to be

selective for pale and yellow photoreceptor input. Such selectivity could in principle be exploited at the level of the synaptic targets of these neurons. Surprisingly, Mi9 cells, another cell type present in every column of the eye, also revealed strong pale/yellow biases in our reconstructions, both with R7 inputs (3:9), as well as R8 inputs (26:1). Given the known role of Mi9 in shaping direction-selective responses on T4 dendrites (Strother et al. 2017; Takemura et al. 2017), these data identify yet another level of crosstalk between chromatic and motion-sensitive channels. Overall, it is an unexpected finding that most projections from the medulla to the lobula from photoreceptor target neurons convey biased pale/yellow inputs. These differences could mediate much broader effects of pale/yellow differences in medulla and lobula circuits than currently appreciated, or these specializations could be blunted by combinations at the next synaptic layer.

Limitations of our approach

By focusing on a small number of columns, we have delivered a very complete picture of local connectivity, but we cannot rule out the possibility that certain cell types may have been overlooked. For instance, we chose an arbitrary threshold of 2-3 synapses below which we did not endeavor to reconstruct synaptic targets to the extent required to uniquely identify them. This threshold may, in principle, have missed large cells that receive small, but significant inputs across many columns. Furthermore, we cannot rule out regional specializations in the eye, such that specific cell types might be found outside of our seed columns. For example, some MeTu cells are only found in the dorsal third of the medulla (Omoto et al. 2017; Otsuna, Shinomiya, and Ito 2014), where incoming R7 cells are known to co-express Rh3 and Rh4 Rhodopsins (Mazzoni et al. 2008).

Complementary usage of multiple connectomic data sets and outlook

Taken together, the data presented here provides access to the full complement of R7 and R8 photoreceptor targets from functionally specialized optical units. By reconstructing these local circuits within a full-brain EM volume, we were able to establish the complete

964 morphology of large, multi-columnar cell types, that are strongly connected to photoreceptors,
965 but had eluded previous connectomic reconstruction efforts (Takemura et al. 2015; Takemura
966 et al. 2013). The sparse tracing approach we have implemented and described here allowed
967 for the relatively efficient identification of the complete set of upstream and downstream
968 partners of the inner photoreceptors, in a manner that is complementary to the dense
969 connectomes generated from smaller-scale medulla volumes. As an example of this
970 synergistic use of complementary data sets, we have returned to the 7-column data (Takemura
971 et al. 2015; Clements et al. 2020) and used our whole-cell morphologies to match the bodies
972 of previously unidentified photoreceptor targets. In that process we have established strong
973 candidates for MeTu, ML1, and perhaps for aMe12 (see Materials and Methods) and confirmed
974 several aspects of their connectivity in FAFB. In so doing, we now have access to the additional
975 connectivity data provided by this dense reconstruction. While full exploration and follow-up
976 analyses of these combined data is beyond the scope of this work, the FIB-SEM/FAFB
977 combination revealed several intriguing connectivity patterns, including new candidate paths
978 for the integration of output from different photoreceptor types. For example, the MeTu cells
979 that are postsynaptic to R7 also receive indirect R8 input via the R8 target Mi15, and ML1
980 combines direct R8 input with indirect input from outer photoreceptors via lamina neurons. As
981 further connectome data sets are completed, this comparative interplay between data sets with
982 unique advantages and limitations, will be an important step in both cross-validating and
983 extending the applicability of all related data sets.

984 Our reconstruction of the DRA photoreceptor targets provides the first EM-based
985 connectomic dataset for modality-specific cell types likely to process skylight information in
986 any insect, and will be important for developing refined models of skylight navigation (Gkanias
987 et al. 2019). Core motifs shared between DRA and central eye columns such as opponency
988 are prime candidates for the computation of visual features that are independent of specific
989 modalities like polarization or color, whereas cell types with preferential connections to either
990 pale of yellow columns are promising candidates for the study of color processing in the insect
991 brain. This comprehensive catalog of the neurons carrying signals from R7 and R8

992 photoreceptors deeper into the brain establishes a broad foundation for further studies into the

993 mechanistic basis of color vision and its contributions to perception and behavior.

994

995

Materials & Methods

EM reconstruction

The "Full Adult Female Brain" (FAFB) data set is a serial section transmission electron microscopy volume of a female *Drosophila melanogaster* brain (Zheng et al. 2018). We manually reconstructed neurons in this volume in the CATMAID environment, which includes a browser-based annotation interface and a server hosting a copy of the data (Saalfeld et al. 2009). We also searched for neurons using two recent auto-segmentations FAFB-FFN1 (Li et al. 2020) and FlyWire (Dorkenwald et al. 2020), importing some of the FAFB-FFN1 auto-segmentation fragments afterwards into the CATMAID environment, a process that facilitated the identification of a small number of neurons. We followed established guidelines for manually tracing neuron skeletons, annotating synaptic connections, and reviewing reconstructed cells (Schneider-Mizell et al. 2016). We completely traced the morphology of pairs of R7 and R8 cells in 7 "seed" columns, 4 adjacent columns chosen to be near the center of the retinal mosaic, and 3 columns in the dorsal rim area (Figure 1C). On the R7 and R8 cells, we annotated as a "pre-synapse" all the locations where there was a T-bar (Figure 1 – figure supplement 1A). Associated with each pre-synapse we annotated a "post-synapse" connection with every synaptic partner. These seed neurons and their pre-synapses were completely proofread by independent team members, a process that amounted in small (<10%) amendments to the connectivity data presented here.

In total, we identified 4043 connections from the seed column R7 and R8 cells to 422 post-synaptic skeletons (the vast majority of which correspond to individual neurons), including the 14 R7/8 cells. We reconstructed their morphology to be able to identify the cell type (e.g. Dm8, Mi1, Tm5a) or cell class (e.g. Dm, Mi, Tm) of 299 cells, whose synapses accounted for 96.2% (3888/4043) of the total synaptic output. For all but one cell, we applied a threshold of >2 synapses to focus our reconstructions on reliable connections – the exception was the Mt-VPN2 cell, which had a large dendritic field and so may integrate many sparse R7 and R8 inputs (Figure 5 – figure supplement 1). There were 244 cells with >2 synapses, of which 224 were identified to cell type, 16 were identified to cell class, giving a total of 240 identified cells

(224 + 16 cells), and the remaining 4 were unidentified (Tables 1 and 3). The 240 identified cells with >2 synapses accounted for 94% (3803/4043) of the total synapses. The 16 cells traced to cell class were sparsely connected, with 4.9 synapses per cell (mean, 79 synapses total). The R7 and R8 cells make infrequent synaptic contacts with glia as well as neurons (Figure 1 – figure supplement 1C), but we did not systematically trace the glia connections. In very rare locations in the FAFB data set, our ability to completely trace processes to completeness was precluded by aberrations in the image quality (Figure 1 – figure supplement 1D), but in most cases the identity of the post-synaptic neurons could still be established.

The 244 cells with >2 synapses were the focus of our analysis, and their connections are summarized in Tables 1 and 3; the connections of individual cells are also organized by cell type for incoming and outgoing synapses in Supplementary File 1. In addition, the morphologies and connections of individual cells with >1 synapses are shown in the gallery figures (Supplementary File 2). Most neurons could be uniquely identified with incomplete reconstructions. Nevertheless, it is useful to establish a reference morphology data and so we completely reconstructed individual examples of specific cell types, in addition to the seed R7 and R8 cells, and in some cases multiple examples. In the central eye, there were 14 completely reconstructed neurons: Dm2, Dm8 (3 cells), Dm9, Dm11, MeTu, Mi15, ML1, ML-VPN1, Tm5a, Tm5b, Tm5c (2 cells). In the DRA, there were 10 completely reconstructed neurons: DmDRA1 (4 cells), DmDRA2 (3 cells), and MeTuDRA (3 cells). A number of these cell types we reconstructed have not been previously described: aMe12, ML1, ML-VPN1, and ML-VPN2 in the central eye; MeMeDRA, MeTuDRA, DRA-VPN and Mti-DRA in the DRA. For one cell whose morphology was similar to the described Tm5a cell type, but whose connectivity was markedly different from the others, we annotated this cell as Tm5a-like. Likewise, for three cells whose morphology was similar to the described Tm5b cell type, but whose connectivity was markedly different from that reported by (Menon et al. 2019), we annotated these cells as Tm5b-like. There were numerous tangential cells contacted in the central eye and DRA columns that do not match those characterized in previous anatomical studies (Fischbach and Dittrich 1989). We have annotated these as medulla tangential intrinsic (Mti) cells when the

cells have processes intrinsic to the medulla, and as medulla tangential visual projection neurons (Mt-VPNs) when they project to neuropils outside the medulla.

We additionally identified 970 incoming synapses to the seed column R7/8 cells from 56 cells, including the 14 R7/8 cells. All of the 30 cells providing >2 synapses were traced so that we could ascribe a cell type, and these cells provided 96% (936/970) of the total incoming synapses (Tables 2,4). In total, we identified the presynaptic cell type of 99% (963/970) of the synapses onto the R7/8 cells (including the 1-synapse contributing cells). All but 1 of the cells providing >2 synapses were themselves contacted by the seed column R7/8 cells, the exception being a DRA C2 cell that provided 5 synapses (Supplementary File 1 - C2 incoming). Including this C2 cell, there were 245 cells with >2 input or output synapses with the seed column photoreceptors (244 + 1 cells).

This report was focused on identifying the synaptic inputs and outputs of the R7 and R8 cells of the central eye and DRA, and so the focus was not on identifying the synaptic inputs to the cells targeted by these photoreceptors. For exceptional cell types, however, we traced more than the cells' connections to the seed column R7 and R8 cells. 1) We traced three aMe12 cells to near completion, to determine the columns that contained the cell type's characteristic vertical processes that we used to determine whether a column was pale or not (see below). 2) We traced all the photoreceptor inputs to three Dm8 cells in the central eye seed columns (Figure 2Cii-iii). 3) For the Mt-VPN1 cell, we reconstructed the photoreceptor inputs in 20 medulla columns to discount the possibility that this was a pale-specific neuronal target in the central eye. 4) For three fully reconstructed DmDRA1 cells and three fully reconstructed DmDRA2 cells we traced all their R7-DRA and R8-DRA inputs (Figure 6E,F). 5) For one Dm9 cell innervated by R7-DRA and R8-DRA, we traced in non-DRA columns to confirm that Dm9 cells in the DRA also receive non-DRA photoreceptor input (Figure 6Cvi).

Defining pale, yellow and DRA medulla columns

To identify medulla columns, we used a map of Mi1 neurons. This Mi1 map, which we have generated for a separate, ongoing study, includes nearly all Mi1 neurons in the medulla of the right hemisphere of the FAFB volume. The Mi1 cell type is columnar, with one cell per

column and unambiguous arborizations in medulla layer 1, 5, 9 and 10 (Fischbach and Dittrich 1989). We defined the location of a column in the medulla as the center-of-mass of the Mi1 dendrite in layer 5 (Figure 1C, 2A).

We traced the vertical dendritic branches of all three aMe12 cells in the data set. Their vertical branches innervate pale columns (Figure 1D), and so we labelled the columns they occupied (by proximity to the nearest Mi1-defined column) as pale columns (Figure 1C). The aMe12 cells have short vertical branches reaching from M6 to M3 and longer vertical branches reaching up to M1 (Figure 1Dii, Eiii). Both the long and short vertical processes were used to assign pale medulla columns. Nearly all the assigned pale columns were innervated by one aMe12 cell, but three columns were innervated by two cells. Using this system, the columns not innervated by aMe12 were yellow candidates (Figure 1C). Despite extreme care and multiple reviews of the aMe12 neurons, errors of omission are always possible in the manual reconstruction procedure, and so we are confident that the 'pale' identified columns are innervated by aMe12, however, it is possible that a small number of the 'yellow' columns are mis-classified. The aMe12 cells innervated just 1 of the 42 identified DRA columns (Figure 1C). While the majority of medulla columns innervated by R7/8 are pale or yellow, there are a small number of ommatidial cartridges with other identities, for example rare (~1-2 per fly) ommatidial pairs of R7 and R8 cells expressing Rh3 and Rh6, respectively (Chou et al. 1996). The congruence of the pale- and yellow-specificity we observed for Tm5a, aMe12 and ML-VPN1 cell types, indicated that our allocation of pale columns in the central eye seed columns was robust, and consistent with the previous report of the yellow-specificity of Tm5a cells (Karuppudurai et al. 2014).

To identify the DRA columns, we reconstructed the R7 and R8 cells in 27 columns along the dorsal-rim-corresponding margin of the medulla and ascertained whether the R8 cell terminated in the same layer as the R7 cell (Figure 1E, arrow; Figure 1 – figure supplement 1A). The R8-DRA cells terminate before the R7-DRA cells in this layer, allowing the two cell types to be distinguished. By careful visual inspection of the M6 layer of all medulla columns located close to the dorsal edge of the medulla we identified 15 additional DRA columns

resulting in a total of 42 DRA columns which is in good agreement with the previously reported average number of 39 DRA columns (Weir et al. 2016; Figure 1C).

Analysis of synapse locations

To define the medulla and lobula layers, we first used the R package "natverse" (Bates et al. 2020) to transform pre-defined neuropil meshes (Jenett et al. 2012; Bogovic et al. 2019) into the FAFB space. Our meshes for the medulla and lobula computed in this way defined the top and bottom layers of these neuropils. We then interpolated the initial internal layer boundaries using demarcations established in prior studies (Takemura et al. 2015; Wu et al. 2016). Finally, we refined the layer boundaries using the characteristic arborizations patterns of the Mi1, C2, Tm5 and Tm20 cell types (Gao et al. 2008; Fischbach and Dittrich 1989). For the medulla, the demarcations were: 0%, 8.2%, 26.2%, 36.1%, 45.9%, 54.1%, 62.3%, 67.2%, 76.2%, 91.0%, 100%. For the lobula the layer demarcations were: 0%, 4.2%, 11.3%, 22.4%, 37.4%, 49.4%, 64.7%, 100%. The layer designations are therefore guides to aid interpretations and comparisons, and not measurements of the neuropils themselves.

To plot the histograms of the synaptic depths in the medulla (e.g. Figure 1Eiii, we took the projection of the synapse locations along the columnar axis, and smoothed this distribution of synaptic depths with a zero-phase Gaussian filter with a standard deviation of 0.4 μm. For the histograms of distances of R7 synapses to each Dm8 cell's home column (Figure 2Ciii), we took the projection of the synapse locations onto the plane perpendicular to the columnar axis, and calculated the distance in that plane to the column center. The resulting distribution of distances was then smoothed with a zero-phase Gaussian filter with a standard deviation of 0.6 μm.

For the histograms of the distances along the DRA of photoreceptor synapses to DmDRA1 and DmDRA2 cells (Figure 6E,F), we first fitted an ellipse to the centers of DRA columns, using least squares regression (Figure 7 – figure supplement 2Ai). We then calculated the location of the perpendicular projection of every synapse along the fitted ellipse

(Figure 7 – figure supplement 2Aii-iv). Finally, these distances were filtered with a zero-phase Gaussian filter with a standard deviation of 0.6 μm.

Comparison with 7-column medulla FIB-SEM data set

To compare the connectivity of R7 and R8 of our central eye reconstructions with the connectivity identified in the medulla FIB-SEM data set (Takemura et al. 2015; Takemura et al. 2013), we took advantage of the identification of pale and yellow columns in that data set used by (Menon et al. 2019). They used the presence or absence of Tm5a to indicate yellow and pale columns, respectively, and excluded columns that contained Tm5 neurons that were ambiguous for being Tm5a or Tm5b neurons. Using this scheme, columns B, D and H are pale, and columns A, E and F are yellow. The 7-column medulla data set is now publically available and accessible with the release of NeuPrint (Clements et al. 2020), and we used NeuPrint to compile the connectivity of cells with pale and yellow R7 and R8 cells from the data set (Figure 1 suppl. 2). The unidentified cells, including cells annotated as output ('out') and fragments of putative tangential cells ('tan') in the six pale and yellow columns are 38.1% for R7 (518/1342 synapses over 6 columns) and 38.9% for R8 (726/1854 synapses over 6 columns).

We also searched the FIB-SEM data set for neurons with shapes and patterns of connectivity similar to aMe12, ML1, and MeTu neurons and identified the following putative matches (NeuPrint medulla7column identifiers in parenthesis): aMe12 (54028), ML1(16666), MeTu (11770; annotated as an unknown Tm; 35751 and other reconstructions annotated as 'Dm7'). The ML1 and MeTu matches are further supported by multiple inputs other than R-cells (e.g. L3, L4 and Dm9 to ML1 and Mi15 to MeTu) that are present in both datasets. These matches provide examples of how the combination of our complete but focused reconstructions and the dense but strongly volume-limited FIB-SEM data can together enable insights that go beyond each individual dataset.

Genetics and molecular biology

1163 Fly genotypes

1164 Fly genotypes are listed in the Key Resources Table (organized by Figure panel).

1165

1166 Driver lines

1167 Split-GAL4 lines were constructed and characterized as in previous work (Wu et al.
1168 2016). Briefly, we tested candidate AD and DBD hemidriver pairs (Tirian and Dickson 2017;
1169 Dionne et al. 2018). for expression in cell types of interest and assembled successful
1170 combinations into stable fly strains that were then used for subsequent experiments. Split-
1171 GAL4 lines generated in this study and images of their expression patterns will be made
1172 available at (https://www.janelia.org/split-GAL4). aMe12, ML1 and ML-VPN1 were initially
1173 identified by light microscopy, allowing us to generate split-GAL4 driver lines targeting these
1174 previously undescribed cell types. Images of cells labeled by these driver lines were
1175 subsequently matched to the EM reconstructions. Split-GAL4 lines labeling Dm11, Mi15, L2
1176 and VPN-DRA were from prior work (Davis et al. 2020; Tuthill et al. 2013; Wu et al. 2016). The
1177 candidate VPN-DRA driver (OL0007B) was originally described as a split-GAL4 driver for a
1178 different cell type (LC12, (Wu et al. 2016)) but also labels neurons highly similar or identical to
1179 VPN-DRA. We also used GAL4 driver lines from the Janelia and Vienna Tiles collections
1180 (Jenett et al. 2012; Tirian and Dickson 2017).

1181 Rhodopsin-LexA reporter constructs

1182 To construct Rh3-, Rh5- and Rh6-LexA driver lines, we amplified previously
1183 characterized promoter regions (Mollereau et al. 2000; Pichaud and Desplan 2001; Tahayato
1184 et al. 2003; Chou et al. 1996; Papatsenko, Sheng, and Desplan 1997; Huber et al. 1997) by
1185 PCR from genomic DNA. Primer sequences are listed in the Key Resources Table. The PCR
1186 products were TOPO-cloned into pENTR-D-TOPO (Invitrogen) and transferred to
1187 pBPnlsLexA::GADflUw (addgene #26232) using standard Gateway cloning. Transgenic flies
1188 were generated by phiC31-mediated integration into the attP40 landing site (injections were
1189 done by Genetic Services, Inc).

1190

Histology

To characterize the neurons labeled by split-GAL4 lines, we visualized both overall expression patterns and individual cells. For the former, we used we pJFRC51-3XUAS-IVS-Syt::smHA in su(Hw)attP1 and pJFRC225-5XUAS-IVS-myr::smFLAG in VK00005 (Nern et al., 2015) or 20XUAS-CsChrimson-mVenus in attP18 (Klapoetke et al. 2017) as reporters; the latter was achieved by stochastic labeling of individual cells with MCFO (Nern, Pfeiffer, and Rubin 2015). Specimens were processed and imaged by the Janelia FlyLight Project team following protocols that are available online (https://www.janelia.org/project-team/flylight/protocols under “IHC - Anti-GFP”, “IHC - Polarity Sequential”, “IHC – MCFO and “DPX mounting”). Additional MCFO images of cells labeled by GAL4 (instead of split-GAL4) driver lines were generated in the same way. Images were acquired on Zeiss LSM 710 or 780 confocal microscope using 20x 0.8 NA or 63x 1.4 NA objectives.

For the combined labeling of aMe12, ML-VPN1 and VPN-DRA with photoreceptor markers, fly brains were processed using standard immunolabeling protocols as previously described in (Davis et al. 2020). Briefly, flies were dissected in in insect cell culture medium (Schneider’s Insect Medium, Sigma Aldrich, #S0146) followed by fixation with 2% PFA (w/v; prepared from a 20% stock solution, Electron Microscopy Sciences: 15713) in cell culture medium for 1 h at room temperature. This fixation step and the subsequent primary and secondary antibody incubations were each followed by several washes with PBT (0.5 % (v/v) TX-100 (Sigma Aldrich: X100) in PBS). To block nonspecific antibody binding, brains were incubated in PBT-NGS (5% Goat Serum, ThermoFisher: 16210-064, in PBT) for at least 30 min prior to addition of primary antibodies in PBT-NGS. Primary and secondary antibody incubations were at 4°C overnight, all other steps were at room temperature. Brains were mounted in SlowFadeGold (ThermoFisher: S36937).

Primary antibodies were anti-GFP rabbit polyclonal (ThermoFisher: A-11122, RRID:AB_221569; used at 1:1000 dilution), anti-GFP mouse monoclonal 3E6 (ThermoFisher: A-11120, RRID:AB_221568; dilution 1:100), anti-dsRed rabbit polyclonal (Clontech Laboratories, Inc.: 632496, RRID:AB_10013483; dilution 1:1000), anti-chaoptin mouse

monoclonal 24B10 (Fujita et al., 1982; DSHB: RRID:AB_528161, dilution 1:20) and anti-Brp mouse monoclonal nc82 (Wagh et al., 2006; DSHB:RRID:AB_2314866; dilution 1:30). Secondary antibodies were from Jackson ImmunoResearch Laboratories, Inc. . Images were acquired on a Zeiss LSM 880 or confocal microscope using a 40x 1.3 NA objective.

Image processing

Most anatomy figures show reconstructed views of cells of interest generated from confocal stack using FluoRender (http://www.sci.utah.edu/software/fluorender.html). Some images were manually edited to only show the cell relevant for the comparison to the EM reconstructions. Some panels in Figure 4 are overlays of registered images with either the template brain used for registration (Bogovic et al. 2019) or the pattern of a second registered expression pattern (L2 lamina neurons terminal in Figure 4 Bvi). Images with rhodopsin reporter (Rh3-, Rh5 or Rh6-LexA) labeling show single sections or maximum intensity projections through a small number of adjacent slices. For these images, other processing was limited to adjustments of brightness and contrast across the entire field of view for each channel.

Acknowledgements

The authors thank: Lou Scheffer, Shinya Takemura, and Kazunori Shinomiya for access to data, advice and discussions; the FAFB tracing community for supportive and open sharing of methods and data; Janelia Fly Core for fly care and Janelia FlyLight Project Team for help with preparation and imaging of light micrsocopy samples; and the Janelia Visitor program for facilitating early stages of this collaboration. This work was supported by the Deutsche Forschungsgemeinschaft (DFG) through grants WE 5761/2-1 (M.F.W.) and SPP2205 (M.F.W.), AFOSR grant FA9550-19-1-7005 (M.F.W), with support from the Fachbereich Biologie, Chemie & Pharmazie of the Freie Universität Berlin (M.F.W.) and by the Howard Hughes Medical Institute through its support of the Janelia Research Campus (M.B.R. and G.M.R.).

Supplementary Files

Supplementary File 1:

Tables of all central eye R7 and R8 and DRA R7 and R8 target cells by type

Supplementary File 2:

Gallery plots of all central eye R7 and R8 and DRA R7 and R8 target cells by type

References

Bates AS, Manton JD, Jagannathan SR, Costa M, Schlegel P, Rohlfing T, and Jefferis GS. 2020. 'The natverse, a versatile toolbox for combining and analysing neuroanatomical data', *Elife*, 9:e53350.

Bell ML, Earl JB, and Britt SG. 2007. 'Two types of *Drosophila* R7 photoreceptor cells are arranged randomly: a model for stochastic cell-fate determination', *J Comp Neurol*, 502: 75-85.

Bogovic JA, Otsuna H, Heinrich L, Ito M, Jeter J, Meissner G, Nern A, Colonell J, Malkesman O, Ito K., and Saalfeld S. 2019. 'An unbiased template of the *Drosophila* brain and ventral nerve cord': *PLoS One* 15: e0236495.

Busch S, Selcho M, Ito K, and Tanimoto H.. 2009. 'A map of octopaminergic neurons in the *Drosophila* brain', *J Comp Neurol*, 513: 643-67.

Chin AL, Lin CY, Fu TF, Dickson BJ, and Chiang AS. 2014. 'Diversity and wiring variability of visual local neurons in the *Drosophila* medulla M6 stratum', *J Comp Neurol*, 522: 3795-816.

Chou WH, Hall KJ, Wilson DB, Wideman CL, Townson SM, Chadwell LV, and Britt SG. 1996. 'Identification of a novel *Drosophila* opsin reveals specific patterning of the R7 and R8 photoreceptor cells', *Neuron*, 17: 1101-15.

Clements J, Dolafi T, Umayam L, Neubarth NL, Berg S, Scheffer LK, and Plaza SM. 2020. 'neuPrint: Analysis Tools for EM Connectomics': *bioRxiv* 2020.01.16.909465.

Courgeon M, and Desplan C. 2019. 'Coordination between stochastic and deterministic specification in the *Drosophila* visual system', *Science*, 366: eaay6727.

Dacke M, and El Jundi B. 2018. 'The Dung Beetle Compass', *Curr Biol*, 28: R993-R97.

Davis FP, Nern A, Picard S, Reiser MB, Rubin GM, Eddy SR, and Henry GL. 2020. 'A genetic, genomic, and computational resource for exploring neural circuit function', *Elife*, 9: e50901.

Dionne H, Hibbard KL, Cavallaro A, Kao JC, and Rubin GM. 2018. 'Genetic Reagents for Making Split-GAL4 Lines in *Drosophila* ', *Genetics*, 209: 31-35.

Dorkenwald S, McKellar C, Macrina T, Kemnitz N, Lee K, Lu R, Wu J, Popovych S, Mitchell E, Nehoran B, Jia Z, Bae JA, Mu S, Ih D, Castro M, Ogedengbe O, Halageri A, Ashwood Z, Zung J, Brittain D, Collman F, Schneider-Mizell C, Jordan C, Silversmith W, Baker C, Deutsch D, Encarnacion-Rivera L, Kumar S, Burke A, Gager J, Hebditch J, Koolman S, Moore M, Morejohn S, Silverman B, Willie K, Willie R, Yu S-C, Murthy M, and Seung HS. 2020. 'FlyWire: Online community for whole-brain connectomics': *bioRxiv* 2020.08.30.274225.

el Jundi B, Pfeiffer K, and Homberg U. 2011. 'A distinct layer of the medulla integrates sky compass signals in the brain of an insect', *PLoS One*, 6: e27855.

Feiler R, Bjornson R, Kirschfeld K, Mismer D, Rubin GM, Smith DP, Socolich M, and Zuker CS. 1992. 'Ectopic expression of ultraviolet-rhodopsins in the blue photoreceptor cells of *Drosophila*: visual physiology and photochemistry of transgenic animals', *J Neurosci*, 12: 3862-8.

Fischbach KF, and Dittrich APM. 1989. 'The Optic Lobe of *Drosophila melanogaster* .1. A Golgi Analysis of Wild-Type Structure', *Cell Tissue Res*, 258: 441-75.

Fischbach KF, and Lyly-Hunerberg I. 1983. 'Genetic dissection of the anterior optic tract of *Drosophila melanogaster*', *Cell Tissue Res*, 231: 551-63.

1300 Fortini ME, and Rubin GM. 1990. 'Analysis of Cis-Acting Requirements of the Rh3 and Rh4
1301 Genes Reveals a Bipartite Organization to Rhodopsin Promoters in *Drosophila*
1302 *melanogaster*', *Gene Dev*, 4: 444-63.

1303 ———. 1991. 'The Optic Lobe Projection Pattern of Polarization-Sensitive Photoreceptor Cells
1304 in *Drosophila melanogaster*', *Cell Tissue Res*, 265: 185-91.

1305 Gao S, Takemura SY, Ting CY, Huang S, Lu Z, Luan H, Rister J, Thum AS, Yang M, Hong
1306 ST, Wang JW, Odenwald WF, White BH, Meinertzhagen IA, and Lee CH. 2008. 'The
1307 neural substrate of spectral preference in *Drosophila*', *Neuron*, 60: 328-42.

1308 Gkanias E, Risse B, Mangan M, and Webb B. 2019. 'From skylight input to behavioural output:
1309 A computational model of the insect polarised light compass', *PLoS Comput Biol*, 15:
1310 e1007123.

1311 Hardcastle BJ, Omoto JJ, Kandimalla P, Nguyen BM, Keles MF, Boyd NK, Hartenstein V, and
1312 Frye MA. 2021. 'A visual pathway for skylight polarization processing in *Drosophila*',
1313 *Elife*, 10: e63225

1314 Heath SL, Christenson MP, Oriol E, Saavedra-Weisenhaus M, Kohn JR, and Behnia R. 2020.
1315 'Circuit mechanisms underlying chromatic encoding in *Drosophila* photoreceptors'. *Curr*
1316 *Biol*. 30(2):264-275.e8.

1317 Heinze S. 2017. 'Unraveling the neural basis of insect navigation', *Curr Opin Insect Sci*, 24:
1318 58-67.

1319 Heisenberg M, and Buchner E. 1977. 'The role of retinula cell types in visual behavior of
1320 *Drosophila melanogaster*', *J Comp Physiol*, 117: 127-62.

1321 Hempel de Ibarra N, Vorobyev NM, and Menzel R. 2014. 'Mechanisms, functions and ecology
1322 of colour vision in the honeybee', *J Comp Physiol A*, 200: 411-33.

1323 Hilbrant M, Almudi I, Leite DJ, Kuncheria L, Posnien N, Nunes MD, and McGregor AP. 2014.
1324 'Sexual dimorphism and natural variation within and among species in the *Drosophila*
1325 retinal mosaic', *BMC Evol Biol*, 14: 240.

1326 Homberg, U. 2015. 'Sky Compass Orientation in Desert Locusts-Evidence from Field and
1327 Laboratory Studies', *Front Behav Neurosci*, 9: 346.

1328 Huber A, Schulz S, Bentrop J, Groell C, Wolfrum U, and Paulsen R. 1997. 'Molecular cloning
1329 of *Drosophila* Rh6 rhodopsin: the visual pigment of a subset of R8 photoreceptor cells',
1330 *FEBS Lett*, 406: 6-10.

1331 Hulse BK, Haberkern H, Franconville R, Turner-Evans DB, Takemura S, Wolff T, Noorman M,
1332 Dreher M, Dan C, Parekh R, Hermundstad AN, Rubin GM, and Jayaraman V. 2020. 'A
1333 connectome of the *Drosophila* central complex reveals network motifs suitable for
1334 flexible navigation and context-dependent action selection': *bioRxiv*
1335 2020.12.08.413955.

1336 Jagadish S, Barnea G, Clandinin TR, and Axel R. 2014. 'Identifying functional connections of
1337 the inner photoreceptors in *Drosophila* using Tango-Trace', *Neuron*, 83: 630-44.

1338 Jenett A, Rubin GM, Ngo TT, Shepherd D, Murphy C, Dionne H, Pfeiffer BD, Cavallaro A, Hall
1339 D, Jeter J, Iyer N, Fetter D, Hausenfluck JH, Peng H, Trautman ET, Svirskas RR, Myers
1340 EW, Iwinski ZR, Aso Y, DePasquale GM, Enos A, Hulamm P, Lam SC, Li HH, Laverty
1341 TR, Long F, Qu L, Murphy SD, Rokicki K, Safford T, Shaw K, Simpson JH, Sowell A,
1342 Tae S, Yu Y, and Zugates CT. 2012. 'A GAL4-driver line resource for *Drosophila*
1343 neurobiology', *Cell Rep*, 2: 991-1001.

1344 Karuppudurai T, Lin TY, Ting CY, Pursley R, Melnattur KV, Diao F, White BH, Macpherson LJ,
1345 Gallio M, Pohida T, and Lee CH. 2014. 'A hard-wired glutamatergic circuit pools and
1346 relays UV signals to mediate spectral preference in *Drosophila*', *Neuron*, 81: 603-15.

1347 Kind E, Belušič G, and Wernet MF. 2020. 'Retinal Mosaics Across Fly Species: Variations on
1348 a Theme.' in, *Reference Module in Neuroscience and Biobehavioral Psychology*
1349 (Elsevier).

1350 Klapoetke NC, Murata Y, Kim SS, Pulver SR, Birdsey-Benson A, Cho YK, Morimoto TK,
1351 Chuong AS, Carpenter EJ, Tian Z, Wang J, Xie Y, Yan Z, Zhang Y, Chow BY, Curek
1352 B, Melkonian M, Jayaraman V, Constantine-Paton M, Wong GK-S, and Boyden ES.
1353 2014. 'Independent Optical Excitement of Distinct Neural Populations', *Nat Methods*,
1354 11: 338-346.

1355 Konstantinides N, Kapuralin K, Fadil C, Barboza L, Satija R, and Desplan C. 2018. 'Phenotypic
1356 Convergence: Distinct Transcription Factors Regulate Common Terminal Features',
1357 *Cell*, 174: 622-35 e13.

1358 Kurmangaliyev YZ, Yoo J, Valdes-Aleman J, Sanfilippo P, and Zipursky SL. 2020.
1359 'Transcriptional Programs of Circuit Assembly in the *Drosophila* Visual System',
1360 *Neuron*, 108: 1045-57 e6.

1361 Kvon EZ, Kazmar T, Stampfel G, Yanez-Cuna JO, Pagani M, Schernhuber K, Dickson BJ, and
1362 Stark A. 2014. 'Genome-scale functional characterization of *Drosophila* developmental
1363 enhancers in vivo', *Nature*, 512: 91-5.

1364 Labhart T. 1988. 'Polarization-Opponent Interneurons in the Insect Visual-System', *Nature*,
1365 331: 435-37.

1366 Li F, Lindsey JW, Marin EC, Otto N, Dreher M, Dempsey G, Stark I, Bates AS, Pleijzier MW,
1367 Schlegel P, Nern A, Takemura SY, Eckstein N, Yang T, Francis A, Braun A, Parekh R,
1368 Costa M, Scheffer LK, Aso Y, Jefferis GS, Abbott LF, Litwin-Kumar A, Waddell S, and
1369 Rubin GM. 2020. 'The connectome of the adult *Drosophila* mushroom body provides
1370 insights into function', *Elife*, 9: e62576.

1371 Lin TY, Luo J, Shinomiya K, Ting CY, Lu Z, Meinertzhagen IA, and Lee CH. 2016. 'Mapping
1372 chromatic pathways in the *Drosophila* visual system', *J Comp Neurol*, 524: 213-27.

1373 Luo J, Ting CY, Li Y, McQueen P, Lin TY, Hsu CP, and Lee CH. 2020. 'Antagonistic regulation
1374 by insulin-like peptide and activin ensures the elaboration of appropriate dendritic field
1375 sizes of amacrine neurons', *Elife*, 9: e50568.

1376 Mathejczyk TF, and Wernet MF. 2019. 'Heading choices of flying *Drosophila* under changing
1377 angles of polarized light', *Sci Rep*, 9: 16773.

1378 ———. 2020. 'Modular assays for the quantitative study of visually guided navigation in both
1379 flying and walking flies', *J Neurosci Methods*, 340: 108747.

1380 Mauss AS, Vlasits A, Borst A, and Feller M. 2017. 'Visual Circuits for Direction Selectivity',
1381 *Annu Rev Neurosci*, 40: 211-30.

1382 Mazzoni EO, Celik A, Wernet MF, Vasiliauskas D, Johnston RJ, Cook TA, Pichaud F, and
1383 Desplan C. 2008. 'Iroquois complex genes induce co-expression of rhodopsins in
1384 *Drosophila*', *PLoS Biol*, 6: e97.

1385 Meinertzhagen IA, and O'Neil SD. 1991. 'Synaptic organization of columnar elements in the
1386 lamina of the wild type in *Drosophila melanogaster*', *J Comp Neurol*, 305: 232-63.

1387 Meinertzhagen IA, Takemura SY, Lu Z, Huang S, Gao S, Ting CY, and Lee CH. 2009. 'From
1388 form to function: the ways to know a neuron', *J Neurogenet*, 23: 68-77.

1389 Meissner GW, Nern A, Singer RH, Wong AM, Malkesman O, and Long X. 2019. 'Mapping
1390 Neurotransmitter Identity in the Whole-Mount *Drosophila* Brain Using Multiplex High-
1391 Throughput Fluorescence in Situ Hybridization', *Genetics*, 211: 473-82.

1392 Melnattur KV, Pursley R, Lin TY, Ting CY, Smith PD, Pohida T, and Lee CH. 2014. 'Multiple
1393 redundant medulla projection neurons mediate color vision in *Drosophila*', *J*
1394 *Neurogenet*, 28: 374-88.

1395 Menon KP, Kulkarni V, Takemura SY, Anaya M, and Zinn K. 2019. 'Interactions between Dpr11
1396 and DIP-gamma control selection of amacrine neurons in *Drosophila* color vision
1397 circuits', *Elife*, 8: e48935.

1398 Mollereau B, Wernet MF, Beaufils P, Killian D, Pichaud F, Kuhnlein R, and Desplan C. 2000.
1399 'A green fluorescent protein enhancer trap screen in *Drosophila* photoreceptor cells',
1400 *Mech Dev*, 93: 151-60.

1401 Morante J, and Desplan C. 2008. 'The color-vision circuit in the medulla of *Drosophila* ', *Curr*
1402 *Biol*, 18: 553-65.

1403 Mota T, Gronenberg W, Giurfa M, and Sandoz JC. 2013. 'Chromatic processing in the anterior
1404 optic tubercle of the honey bee brain', *J Neurosci*, 33: 4-16.

1405 Nern A, Pfeiffer DB, and Rubin GM. 2015. 'Optimized tools for multicolor stochastic labeling
1406 reveal diverse stereotyped cell arrangements in the fly visual system', *Proc Natl Acad*
1407 *Sci USA*, 112: E2967-76.

1408 Nilsson DE., and Warrant EJ. 1999. 'Visual discrimination: Seeing the third quality of light', *Curr*
1409 *Biol*, 9: R535-7.

1410 Omoto JJ, Keles MF, Nguyen BM, Bolanos C, Lovick JK, Frye MA, and Hartenstein V. 2017.
1411 'Visual Input to the *Drosophila* Central Complex by Developmentally and Functionally
1412 Distinct Neuronal Populations', *Curr Biol*, 27: 1098-110.

1413 Otsuna H, and Ito K. 2006. 'Systematic analysis of the visual projection neurons of *Drosophila*
1414 *melanogaster*. I. Lobula-specific pathways', *J Comp Neurol*, 497: 928-58.

1415 Otsuna H, Shinomiya K, and Ito K. 2014. 'Parallel neural pathways in higher visual centers of
1416 the *Drosophila* brain that mediate wavelength-specific behavior', *Front Neural Circuits*,
1417 8: 8.

1418 Ozel MN, Simon F, Jafari S, Holguera I, Chen YC, Benhra N, El-Danaf RN, Kapuralin K, Malin
1419 JA, Konstantinides N, and Desplan C. 2021. 'Neuronal diversity and convergence in a
1420 visual system developmental atlas', *Nature*, 589: 88-95.

1421 Pagni M, Haikala V, Oberhauser V, Meyer PB, Reiff DF, and Schnaitmann C. 2021. 'Interaction
1422 of "chromatic" and "achromatic" circuits in *Drosophila* color opponent processing', *Curr*
1423 *Biol*, 31, 1687-1698.

1424 Pantazis A, Segaran A, Liu CH, Nikolaev A, Rister J, Thum AS, Roeder T, Semenov E, Juusola
1425 M, and Hardie RC. 2008. 'Distinct roles for two histamine receptors (hclA and hclB) at
1426 the *Drosophila* photoreceptor synapse', *J Neurosci*, 28: 7250-9.

1427 Papatsenko D, Sheng G, and Desplan C. 1997. 'A new rhodopsin in R8 photoreceptors of
1428 *Drosophila*: evidence for coordinate expression with Rh3 in R7 cells', *Development*,
1429 124: 1665-73.

1430 Pfeiffer BD, Jenett A, Hammonds AS, Ngo TT, Misra S, Murphy C, Scully A, Carlson JW, Wan
1431 KH, Laverty TR, Mungall C, Svirskas R, Kadonaga JT, Doe CQ, Eisen MB, Celniker
1432 SE, and Rubin GM. 2008. 'Tools for neuroanatomy and neurogenetics in *Drosophila*',
1433 *Proc Natl Acad Sci USA*, 105: 9715-20.

1434 Pfeiffer K, and Kinoshita M. 2012. 'Segregation of visual inputs from different regions of the
1435 compound eye in two parallel pathways through the anterior optic tubercle of the
1436 bumblebee (*Bombus ignitus*)', *J Comp Neurol*, 520: 212-29.

1437 Pichaud F, and Desplan C. 2001. 'A new visualization approach for identifying mutations that
1438 affect differentiation and organization of the *Drosophila* ommatidia', *Development*, 128:
1439 815-26.

1440 Pollack I, and Hofbauer A. 1991. 'Histamine-like immunoreactivity in the visual system and
1441 brain of *Drosophila melanogaster*', *Cell Tissue Res*, 266: 391-8.

1442 Rister J, and Desplan C. 2011. 'The retinal mosaics of opsin expression in invertebrates and
1443 vertebrates', *Dev Neurobiol*, 71: 1212-26.

1444 Rivera-Alba M, Vitaladevuni SN, Mishchenko Y, Lu Z, Takemura SY, Scheffer L,
1445 Meinertzhagen IA, Chklovskii DB, and de Polavieja GC. 2011. 'Wiring economy and
1446 volume exclusion determine neuronal placement in the *Drosophila* brain', *Curr Biol*, 21:
1447 2000-5.

1448 Saalfeld S, Cardona A, Hartenstein V, and Tomancak P. 2009. 'CATMAID: collaborative
1449 annotation toolkit for massive amounts of image data', *Bioinformatics*, 25: 1984-6.

1450 Salcedo E, Huber A, Henrich S, Chadwell LV, Chou WH, Paulsen R, and Britt SG. 1999. 'Blue-
1451 and green-absorbing visual pigments of *Drosophila*: ectopic expression and
1452 physiological characterization of the R8 photoreceptor cell-specific Rh5 and Rh6
1453 rhodopsins', *J Neurosci*, 19: 10716-26.

1454 Sancer G, Kind E, Plazaola-Sasieta H, Balke J, Pham T, Hasan A, Munch LO, Courgeon M,
1455 Mathejczyk TF, and Wernet MF. 2019. 'Modality-Specific Circuits for Skylight
1456 Orientation in the Fly Visual System', *Curr Biol* 29: 2812-2825.e4.

1457 Sancer G, Kind E, Uhlhorn J, Volkmann J, Hammacher J, Pham T, Plazaola-Sasieta H, and
1458 Wernet MF. 2020. 'Cellular and synaptic adaptations of neural circuits processing
1459 skylight polarization in the fly', *J Comp Physiol A*, 206: 233-46.

1460 Scheffer LK, C. Xu CS, Januszewski M, Lu Z, Takemura SY, Hayworth KJ, Huang GB,
1461 Shinomiya K, Maitin-Shepard J, Berg S, Clements J, Hubbard P, Katz W, Umayam L,
1462 Zhao T, Ackerman D, Blakely T, Bogovic J, Dolafi T, Kainmueller D, Kawase T, Khairy
1463 KA, Leavitt L, Li PH, Lindsey L, Neubarth N, Olbris DJ, Otsuna H, Trautman ET, Ito M,
1464 Goldammer J, Wolff T, Svirskas R, Schlegel P, Neace ER, Knecht CJ, Alvarado CX,
1465 Bailey DA, Ballinger S, Borycz JA, Canino BS, Cheatham N, Cook M, Dreher M, Duclos
1466 O, Eubanks B, Fairbanks K, Finley S, Forknall N, Francis A, Hopkins GP, Joyce EM,
1467 Kim SJ, Kirk NA, Kovalyak J, Lauchie SA, Lohff A, Maldonado C, Manley EA, McLin S,
1468 Mooney C, Ndama M, Ogundeyi O, Okeoma N, Ordish C, Padilla N, Patrick C, Paterson
1469 T, Phillips EE, Phillips EM, Rampally N, Ribeiro C, Robertson MK, Rymer JT, Ryan SM,
1470 Sammons M, Scott AK, Scott AL, Shinomiya A, Smith C, Smith K, Smith NL, Sobeski
1471 MA, Suleiman A, Swift J, Takemura S, Talebi I, Tarnogorska D, Tenshaw E, Tokhi T,
1472 Walsh JJ, Yang T, Horne JA, Li F, Parekh R, Rivlin PK, Jayaraman V, Ito K, Saalfeld
1473 S, George R, Meinertzhagen IA, Rubin GM, Hess HF, Jain V, and Plaza SM. 2020. 'A
1474 Connectome and Analysis of the Adult *Drosophila* Central Brain', *eLife* 9: e57443.

1475 Schnaitmann C, Garbers C, Wachtler T, and Tanimoto H. 2013. 'Color discrimination with
1476 broadband photoreceptors', *Curr Biol*, 23: 2375-82.

1477 Schnaitmann C, Haikala V, Abraham E, Oberhauser V, Thestrup T, Griesbeck O, and Reiff
1478 DF. 2018. 'Color Processing in the Early Visual System of *Drosophila*', *Cell*, 172: 318-
1479 30 e18.

1480 Schneider-Mizell CM, Gerhard S, Longair M, Kazimiers T, Li F, Zwart MF, Champion A,
1481 Midgley FM, Fetter RD, Saalfeld S, and Cardona A. 2016. 'Quantitative neuroanatomy
1482 for connectomics in *Drosophila* ', *Elife*, 5: e12059.

1483 Sharkey CR, Blanco J, Leibowitz MM, Pinto-Benito D, and Wardill TJ. 2020. 'The spectral
1484 sensitivity of *Drosophila* photoreceptors', *Sci Rep*, 10: 18242.

1485 Shinomiya K, Karuppudurai T, Lin TY, Lu Z, Lee CH, and Meinertzhagen IA. 2014. 'Candidate
1486 neural substrates for off-edge motion detection in *Drosophila*', *Curr Biol*, 24: 1062-70.

1487 Silies MD, Gohl M, Fisher YE, Freifeld L, Clark DA, and Clandinin TR. 2013. 'Modular use of
1488 peripheral input channels tunes motion-detecting circuitry', *Neuron*, 79: 111-27.

1489 Strother JA, Wu ST, Wong AM, Nern A, Rogers EM, Le JQ, Rubin GM, and Reiser MB. 2017.
1490 'The Emergence of Directional Selectivity in the Visual Motion Pathway of *Drosophila*',
1491 *Neuron*, 94: 168-82 e10.

1492 Tahayato A, Sonneville R, Pichaud F, Wernet MF, Papatsenko D, Beaufils P, Cook T, and
1493 Desplan C. 2003. 'Otd/Crx, a dual regulator for the specification of ommatidia subtypes
1494 in the *Drosophila* retina', *Dev Cell*, 5: 391-402.

1495 Tai CY, Chin AL, and Chiang AS. 2021. 'Comprehensive map of visual projection neurons for
1496 processing ultraviolet information in the *Drosophila* brain', *J Comp Neurol*, 529: 1988-
1497 2013.

1498 Takemura S, Bharioke A, Lu ZY, Nern A, Vitaladevuni S, Rivlin PK, Katz WT, Olbris DJ, Plaza
1499 SM, Winston P, Zhao T, Horne JA, Fetter RD, Takemura S, Blazek K, Chang LA,
1500 Ogundeyi O, Saunders MA, Shapiro V, Sigmund C, Rubin GM, Scheffer LK,
1501 Meinertzhagen IA, and Chklovskii DB. 2013. 'A visual motion detection circuit
1502 suggested by *Drosophila* connectomics', *Nature*, 500: 175-181.

1503 Takemura, S. Y., Z. Y. Lu, and Meinertzhagen IA. 2008. 'Synaptic circuits of the *Drosophila*
1504 optic lobe: The input terminals to the medulla', *J Comp Neurol*, 509: 493-513.

1505 Takemura, S. Y., Nern A, Chklovskii DB, Scheffer LK, Rubin GM, and Meinertzhagen IA. 2017.
1506 'The comprehensive connectome of a neural substrate for 'ON' motion detection in
1507 *Drosophila* ', *Elife*, 6: e24394.

1508 Takemura SY, C. S. Xu, Z. Lu, P. K. Rivlin, T. Parag, D. J. Olbris, S. Plaza, T. Zhao, W. T.
1509 Katz, L. Umayam, C. Weaver, H. F. Hess, J. A. Horne, J. Nunez-Iglesias, R. Aniceto,
1510 L. A. Chang, S. Lauchie, A. Nasca, O. Ogundeyi, C. Sigmund, Takemura S, Tran J,
1511 Langille C, Le Lacheur K, McLin S, Shinomiya A, Chklovskii DB, Meinertzhagen IA, and
1512 Scheffer LK. 2015. 'Synaptic circuits and their variations within different columns in the
1513 visual system of *Drosophila* ', *Proc Natl Acad Sci USA*, 112: 13711-6.

1514 Timaeus L, Geid L, Sancer G, Wernet MF, and Hummel T. 2020. 'Parallel visual pathways with
1515 topographic versus non-topographic organization connect the *Drosophila* eyes to the
1516 central brain', *bioRxiv*: 2020.04.11.037333.

1517 Tirian L, and Dickson BJ. 2017. 'The VT GAL4, LexA, and split-GAL4 driver line collections for
1518 targeted expression in the *Drosophila* nervous system': *bioRxiv* 198648.

1519 Tuthill JC, Nern A, Holtz SL, Rubin GM, and Reiser MB. 2013. 'Contributions of the 12 neuron
1520 classes in the fly lamina to motion vision', *Neuron*, 79: 128-40.

1521 Uhlhorn J, and Wernet MF. 2020. 'Colour Vision: Self-Centered Fly Photoreceptors
1522 Communicate over Distances', *Curr Biol*, 30: R78-R81.

1523 Wada S. 1974a. 'Special Marginal Ommatidia of Flies (Diptera-Brachycera) - Architecture and
1524 Distribution in Compound Eyes', *Z Morphol Tiere*, 77: 87-125.

1525 ———. 1974b. 'Spezielle randzonale ommatidien von Calliphora Erythrocephala meig.
1526 (diptera calliphoridae): Architektur der zentralen rhabdomeren-kolumne und
1527 topographie im komplexauge', *Int J Insect Morphol*, 3: 397-424.

1528 Wardill TJ, List O, Li X, Dongre S, McCulloch M, Ting CY, O'Kane CJ, Tang S, Lee CH, Hardie
1529 RC, and Juusola M. 2012. 'Multiple spectral inputs improve motion discrimination in the
1530 *Drosophila* visual system', *Science*, 336: 925-31.

1531 Warren TL., Weir PT, and Dickinson MH. 2018. 'Flying *Drosophila melanogaster* maintain
1532 arbitrary but stable headings relative to the angle of polarized light', *J Exp Biol*, 221.

1533 Wehner R, and Muller M. 1985. 'Does Interocular Transfer Occur in Visual Navigation by Ants',
1534 *Nature*, 315: 228-29.

1535 Weir PT, and Dickinson MH. 2012. 'Flying *Drosophila* Orient to Sky Polarization', *Current*
1536 *Biology*, 22: 21-27.

1537 Weir PT, Henze MJ, Bleul C, Baumann-Klausener F, Labhart T, and Dickinson MH. 2016.
1538 'Anatomical Reconstruction and Functional Imaging Reveal an Ordered Array of
1539 Skylight Polarization Detectors in *Drosophila* ', *J Neurosci*, 36: 5397-404.

1540 Wernet MF, Huberman AD, and Desplan C. 2014. 'So many pieces, one puzzle: cell type
1541 specification and visual circuitry in flies and mice', *Genes Dev*, 28: 2565-84.

1542 Wernet MF, Labhart T, Baumann F, Mazzoni EO, Pichaud F, and Desplan C. 2003.
1543 'Homothorax switches function of *Drosophila* photoreceptors from color to polarized
1544 light sensors', *Cell*, 115: 267-79.

1545 Wernet MF, Perry MW, and Desplan C. 2015. 'The evolutionary diversity of insect retinal
1546 mosaics: common design principles and emerging molecular logic', *Trends Genet*, 31:
1547 316-28.

1548 Wernet MF, Velez MM, Clark DA, Baumann-Klausener F, Brown JR, Klovstad M, Labhart T,
1549 and Clandinin TR. 2012. 'Genetic dissection reveals two separate retinal substrates for
1550 polarization vision in *Drosophila* ', *Curr Biol*, 22: 12-20.

1551 Wu M, Nern A, Williamson WR, Morimoto MM, Reiser MB, Card GM, and Rubin GM. 2016.
1552 'Visual projection neurons in the *Drosophila* lobula link feature detection to distinct
1553 behavioral programs', *Elife*, 5: e21022.

1554 Yamaguchi S, Wolf R, Desplan C, and Heisenberg M. 2008. 'Motion vision is independent of
1555 color in *Drosophila*', *Proc Natl Acad Sci USA*, 105: 4910-5.

1556 Zheng Z, Lauritzen JS, Perlman E, Robinson CG, Nichols M, Milkie D, Torrens O, Price J,
1557 Fisher CB, Sharifi N, Calle-Schuler SA, Kmecova L, Ali IJ, Karsh B, Trautman ET,
1558 Bogovic JA, Hanslovsky P, Jefferis GSXE, Kazhdan M, Khairy K, Saalfeld S, Fetter
1559 RD, and Bock. 2018 DD. 'A Complete Electron Microsc opy Volume of the Brain of
1560 Adult *Drosophila melanogaster*', *Cell*, 174: 730-43 e22.

1561

1562

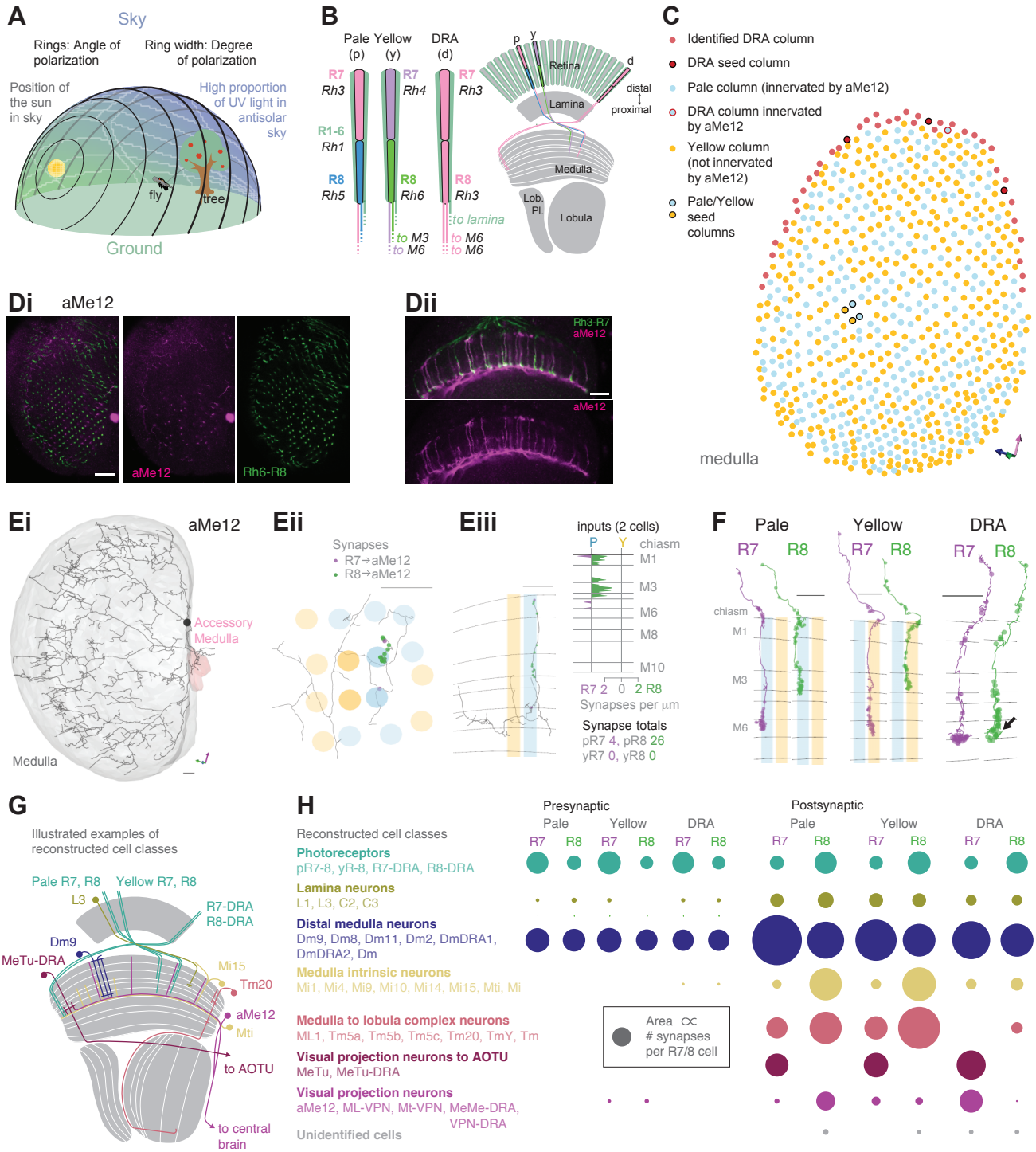
A
Sky
Rings: Angle of polarization
Ring width: Degree of polarization
Position of the sun in sky
High proportion of UV light in antisolar sky
fly
tree
Ground
B
Pale (p)
Yellow (y)
DRA (d)
R7 Rh3
R7 Rh4
R7 Rh3
R1-6 Rh1
R8 Rh5
R8 Rh6
R8 Rh3
to M3
to M6
to lamina
to M6
to M6
p
y
d
Retina
Lamina
distal
proximal
Medulla
Lob. Pl.
Lobula
C
Identified DRA column
DRA seed column
Pale column (innervated by aMe12)
DRA column innervated by aMe12
Yellow column (not innervated by aMe12)
Pale/Yellow seed columns
medulla
Di
aMe12
aMe12
Rh6-R8
Dii
Rh3-R7
aMe12
aMe12
Ei
aMe12
Accessory Medulla
Medulla
Eii
Synapses
R7→aMe12
R8→aMe12
Eiii
inputs (2 cells)
P
Y
chiasm
M1
M3
M6
M8
M10
R7 2 0 2 R8
Synapses per µm
Synapse totals
pR7 4, pR8 26
yR7 0, yR8 0
F
Pale
Yellow
DRA
R7
R8
chiasm
M1
M3
M6
G
Illustrated examples of reconstructed cell classes
Pale R7, R8
Yellow R7, R8
L3
R7-DRA
R8-DRA
Dm9
MeTu-DRA
Mi15
Tm20
aMe12
Mti
to AOTU
to central brain
H
Reconstructed cell classes
Photoreceptors
pR7-8, yR-8, R7-DRA, R8-DRA
Lamina neurons
L1, L3, C2, C3
Distal medulla neurons
Dm9, Dm8, Dm11, Dm2, DmDRA1, DmDRA2, Dm
Medulla intrinsic neurons
Mi1, Mi4, Mi9, Mi10, Mi14, Mi15, Mti, Mi
Medulla to lobula complex neurons
ML1, Tm5a, Tm5b, Tm5c, Tm20, TmY, Tm
Visual projection neurons to AOTU
MeTu, MeTu-DRA
Visual projection neurons
aMe12, ML-VPN, Mt-VPN, MeMe-DRA, VPN-DRA
Unidentified cells
Presynaptic
Postsynaptic
Pale
Yellow
DRA
R7
R8
Area ∝ # synapses per R7/8 cell

Figure 1

Figure 1: Systematic reconstruction of synaptic targets of functionally specialized inner photoreceptor cells R7 and R8

A. Simplified schematic summarizing some of the most salient visual stimuli of a fly (center): celestial cues (sun), color gradients (distribution of green versus UV wavelengths) and skylight polarization (as defined by degree of polarization and angle of polarization) can be used for navigation, as well as more or less colorful landmarks (tree). **B.** Schematic representation of the fly visual system. Left: In the retina, inner photoreceptor R7 (distal) and R8 (proximal) rhodopsin expression differs across three functionally specialized subtypes pale (p), yellow (y), and DRA (d). Rh3 and Rh4 opsins are both UV-sensitive, whereas Rh5 and Rh6 are more sensitive to blue and green wavelengths, respectively. Only in the DRA, both R7 and R8 axons terminate in the same layer of the medulla neuropil (M6), which is the target layer of R7 cells outside the DRA, and non-DRA R8 cells terminate in layer M3. Right: Overview of the main four optic lobe neuropils. Oút of these, only lamina and medulla receive direct photoreceptor input. **C.** Distribution of medulla columns downstream of either p (light blue), y (yellow), and DRA (red) photoreceptors reconstructed from the FAFB dataset. Pale columns were identified via presence of aMe12 long vertical projections (see below). Seven seed columns used for systematic reconstruction are highlighted with black circles. **D.** Double labeling of aMe12 vertical processes (purple) and yellow R8 cells. Left (Di): Confocal section showing the array of medulla columns with labeling of aMe12 neurons (purple) and yellow R8 axons (green). Note that the two patterns appear near-mutually exclusive. Right (Dii): Side view of aMe12 vertical projections and pale R7 axons (green). Di-ii Scale bars: 20 μm. **E.** Left (Ei): Skeleton of the optic lobe part of a fully reconstructed aMe12 neuron (gray), with processes leaving the medulla through the accessory medulla (pink). Eii: Across the four central seed columns (darker shading), synaptic input from R7 (purple dots) and R8 phoroeceptors (green dots) to aMe12 is specific to pale columns. Eiii, Left: Sideview depicting the distribution of R7 and R8 inputs into aMe12 across medulla layers (color code of pale and yellow columns as before). Right: Same distribution plotted as synapses/μm, for both pale and yellow columns (color code as before). Ei-iii: Scale bars: 10 μm. **F.** Reconstructed pale R7 and R8, yellow R7 and R8, and

R7-DRA and R8-DRA terminals with R7 presynapses in purple and R8 presynapses in green. Note the termination of R8-DRA in the R7 target layer M6 (arrow). Scale bars: 10 μm. **G.** Illustrations of reconstructed neuron classes, including lamina monopolar (L), distal medulla (Dm), medulla intrinsic (Mi), transmedulla (Tm), medulla tangential intrinsic (Mti), visual projection neurons targeting the central brain (example: aMe12), and medulla-to-tubercle (MeTu) cells, projecting to the anterior optic tubercle (AOTU). **H.** Overview over the relative strength of R7 and R8 synaptic connections with different neuron classes (color code as before), including unidentified cells (Tables 1-4), across pale, yellow, and DRA columns (pre- and post-synaptic), for cells with ≥3 synapses. Area of circles corresponds to the number of synapses per R7 R8 cell.

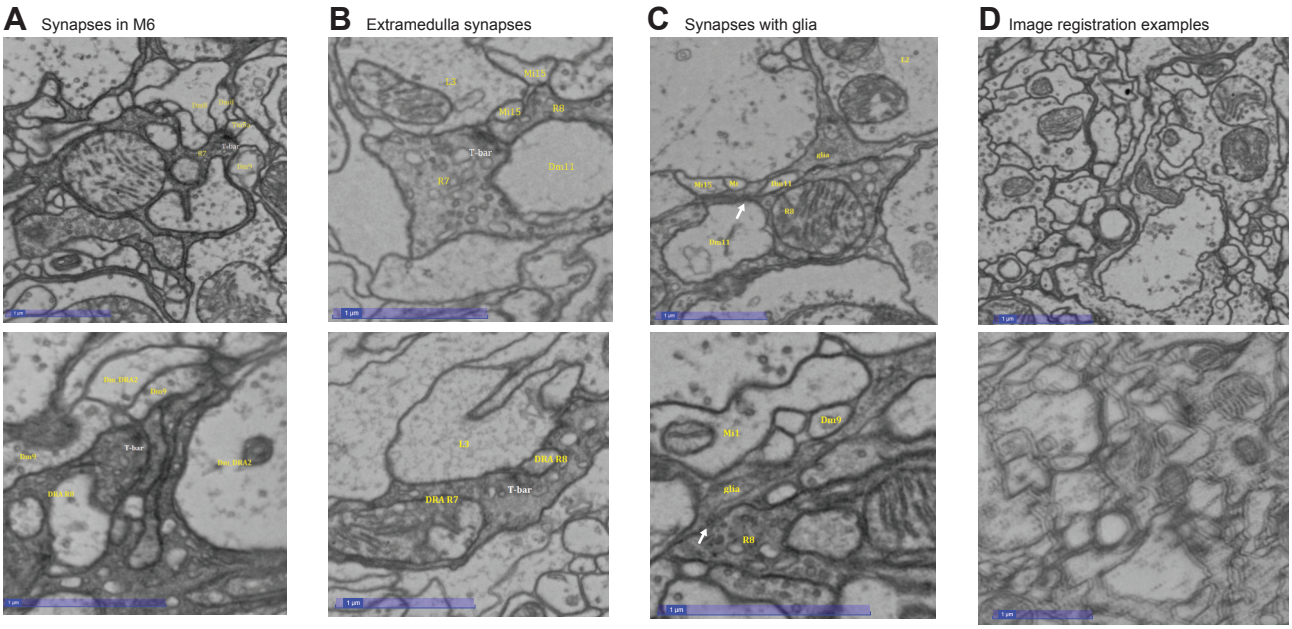

Figure 1 – figure supplement 1

1602 Figure 1 - figure supplement 1: Examples of EM-images

1603 **A**. Examples of EM-images of photoreceptors synapses in medulla layer 6. Top: an R7
1604 presynapse (T-bar labelled) with postsynaptic Dm8, Dm9 and Tm5a cells. Bottom: an R8-DRA
1605 presynapse, with postsynaptic Dm9 and DmDRA2 cells. The presence of R8 synapses in layer
1606 6 was diagnostic of DRA columns (see Materials and Methods). **B**. Images of extramedullar
1607 synapses in the central eye (top) and DRA (bottom) seed columns. **C**. Photoreceptors
1608 infrequently but reliably make synapses onto glia. Two examples are shown, with the arrows
1609 indicating the postsynaptic density in the glial cell. **D**. Very occasionally there were step
1610 changes in the image registration, which hindered, for example, the complete tracing of all
1611 three aMe12 cells across the medulla. One example is shown for two spatially close images.
1612 All scale bars: 1 μm.

1613

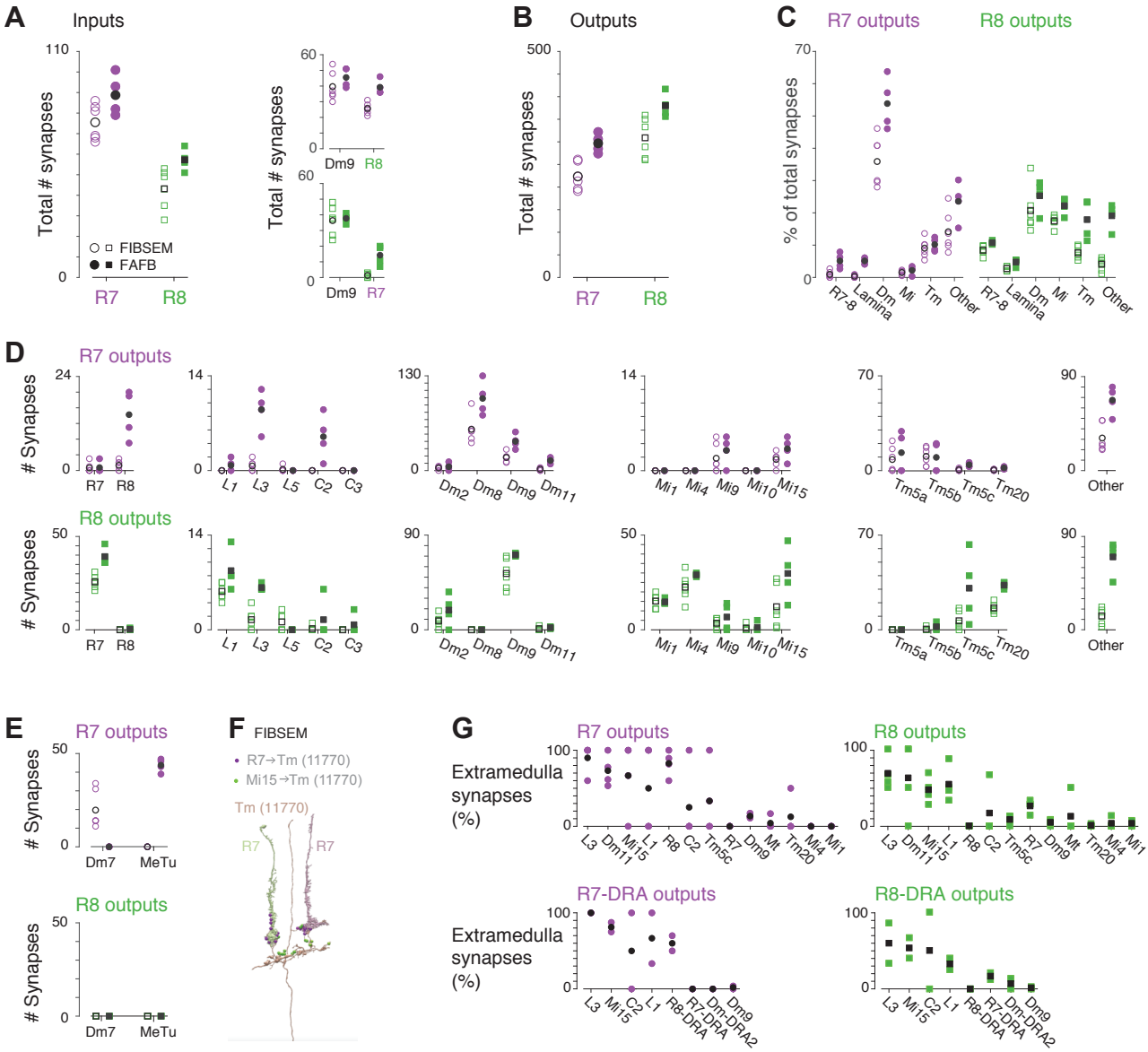

Figure 1 – figure supplement 2

Figure 1 – figure supplement 2: Comparison with medulla FIB-SEM data

A. Left: Comparison of total numbers of synaptic inputs to R7 (purple, circles) and R8 (green, squares) in our dataset (filled symbols) and a medulla FIB-SEM dataset (open symbols), with mean values are indicated by black symbols. These plotting conventions are used throughout the figure. We used the six columns identified as pale and yellow in the FIB-SEM dataset by Menon et al. (2019), made available in Clements et al. (2020), see Materials and Methods. Right: The R7/R8 photoreceptors and Dm9 inputs dominate the synaptic input; the increased number of extramedullar synapses (see panel G) accounts for the higher number of inputs to our R7/R8 cells. **B**. Comparison of the total number of synapses outputs of R7 and R8. We reconstructed more output synapses than in the FIB-SEM dataset, and subsequent plots identify the cell types that account for this increase. **C**. Comparison of total numbers of R7/R8 output synapses disaggregated by cell classes. To enable like-for-like comparisons, we used cell classes of cell types present in both datasets, with the cell types shown in D. To quantify the completeness of cell type identification, we counted all other identified cell types found in the dataset in the 'Other' category. There was a large increase in R7 synapses to multicolumnar Dm cells, and increases in R8 synapses to multicolumnar cell classes, such as Tm cells and cells like aMe12 in the 'Other' class. **D**. Comparison of total numbers of R7 (top) and R8 (bottom) output synapses disaggregated by cell type, with cell types grouped from left to right by their cell class categories in C. For R7, there were increases in synapses to R8 and L3, which receive extramedullar synapses, and Dm8 cells, which are multicolumnar. For R8, there were increases in synapses to R7 and Mi15, which receive extramedullar synapses, and multicolumnar Tm5c and 'Other' cell types, and also Tm20 cells, which was surprising because this cell type is columnar. **E**. Comparison of R7/R8 synapses to Dm7 and MeTu cells. These two cell types were the only cell type discrepancies between the datasets: Dm7 cells were a target of R7 in the FIB-SEM data, but not in ours, while MeTu cells were major targets in our data but not in the FIB-SEM data. **F**. Example Tm cell (brown, Tm #11770) in the FIB-SEM data whose dendritic morphology matched MeTu cell. Two R7 cells (green, left, and purple, right), are also shown, along with R7 synapses (green circles) and Mi15 synapses (purple).

1642 We propose that some MeTu cells may be annotated as unidientified Tm or Dm7 cells in the
1643 FIB-SEM data. **G**. Percentages of extramedullar R7 (top) and R8 (bottom) connections to cell
1644 types in the central eye (left) and DRA (right) seed columns. L3 in particular is almost
1645 exclusively innervated outside the medulla. Synapses outside the medulla neuropile were
1646 present in both the central eye and DRA columns.
1647

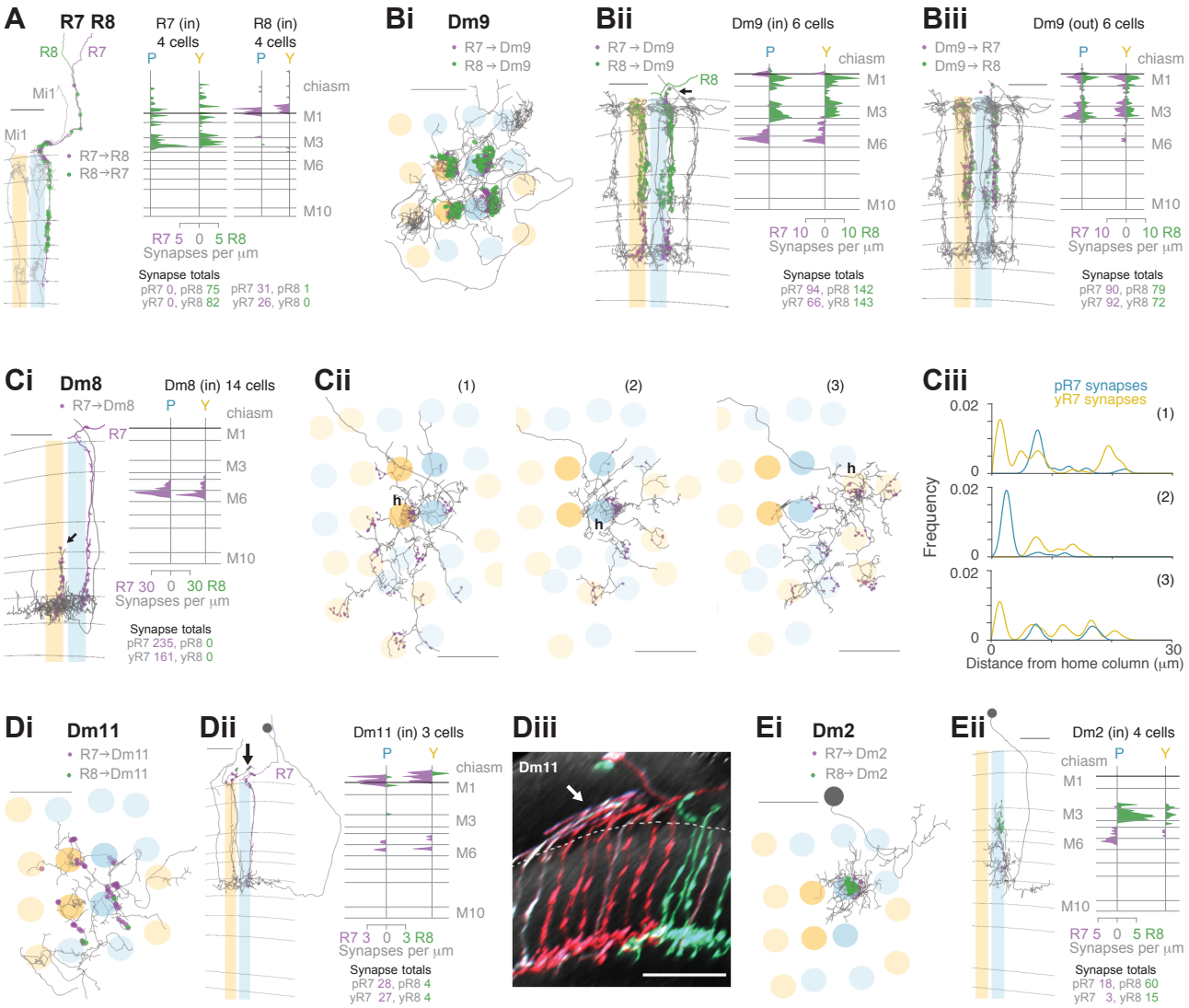
A
R7 R8
R8
R7
Mi1
Mi1
R7→R8
R8→R7
R7 (in)
4 cells
R8 (in)
4 cells
P Y
P Y
chiasm
M1
M3
M6
M10
R7 5 0 5 R8
Synapses per µm
Synapse totals
pR7 0, pR8 75
yR7 0, yR8 82
pR7 31, pR8 1
yR7 26, yR8 0
Bi
Dm9
R7→Dm9
R8→Dm9
Bii
R7→Dm9
R8→Dm9
R8
Dm9 (in) 6 cells
P Y
chiasm
M1
M3
M6
M10
R7 10 0 10 R8
Synapses per µm
Synapse totals
pR7 94, pR8 142
yR7 66, yR8 143
Biii
Dm9→R7
Dm9→R8
Dm9 (out) 6 cells
P Y
chiasm
M1
M3
M6
M10
R7 10 0 10 R8
Synapses per µm
Synapse totals
pR7 90, pR8 79
yR7 92, yR8 72
Ci
Dm8
R7→Dm8
R7
Dm8 (in) 14 cells
P Y
chiasm
M1
M3
M6
M10
R7 30 0 30 R8
Synapses per µm
Synapse totals
pR7 235, pR8 0
yR7 161, yR8 0
Cii
(1)
(2)
(3)
h
h
h
Ciii
pR7 synapses
yR7 synapses
0.02
0
0.02
0
0.02
0
Frequency
(1)
(2)
(3)
0
30
Distance from home column (µm)
Di
Dm11
R7→Dm11
R8→Dm11
Dii
R7
Dm11 (in) 3 cells
P Y
chiasm
M1
M3
M6
M10
R7 3 0 3 R8
Synapses per µm
Synapse totals
pR7 28, pR8 4
yR7 27, yR8 4
Diii
Dm11
Ei
Dm2
R7→Dm2
R8→Dm2
Eii
Dm2 (in) 4 cells
chiasm
P Y
M1
M3
M6
M10
R7 5 0 5 R8
Synapses per µm
Synapse totals
pR7 18, pR8 60
yR7 3, yR8 15

Figure 2

Figure 2: Synapses between R7 and R8 and with Dm neurons in the central medulla

A. Synapses between central R7 and R8 cells. Left: Side view of R7 (purple) and R8 (green), with R7→R8 synapses (purple points) and R8→R7 synapses (green points). Note synapses outside the medulla neuropil (distal to layer M1). Mi1 skeletons (light grey) were used as column markers. Scale bar: 10 μm. Right: Synapse distribution (in synapses/μm) in the yellow and pale seed columns. **B.** Synapses between R7 and R8 and Dm9 cells. Bi: Top view of a fully reconstructed Dm9 skeleton (grey) covering all four central seed columns (darker shading) with all R7 (purple) and R8 (green) inputs. Bii, Left: Side view of R7 (purple) and R8 synapses (green) to the same Dm9 cell across medulla layers. Right: Layer distribution of photoreceptor inputs to six Dm9 cells. Biii, Left: Side view of Dm9→ R7 (purple) and Dm9→R8 (green) feedback synapses from the same Dm9 cell. Right: Layer distribution of feedback synapses from six Dm9 occupying the seed columns. **C.** Synapses between R7 and Dm8 cells. Ci, Left: Side view of R7 synapses (purple) to a fully reconstructed Dm8 cell, with one pale R7 cell is shown in purple. Note the characteristic vertical projections of Dm8 in its 'home column' (arrow; yellow R7 cell not shown). Right: Layer distribution of R7 inputs from 14 Dm8 cells innervating the four seed columns. Cii: Full reconstructions of three Dm8 cells (labeled 1,2,3) innervating the four seed columns, with all R7 synapses (purple), including inputs beyond the seed columns. Individual Dm8 home columns (h) are marked. Ci-ii Scale bars: 10 μm. Ciii: R7→Dm8 synapses/μm as a function of their distance from the home column, for the three Dm8 cells (1,2,3 above). The cells receive dense innervation in their home column and weaker inputs from both pale and yellow R7 cells in their periphery. **D.** Synapses between R7 and Dm11 cells with R7 (purple) and R8 (green) synapses from seed columns. Di: Top view of a fully reconstructed Dm11 skeleton. Dii, Left: Side view of the layer distribution of photoreceptor synapses, including synapses outside the medulla (arrow). Di-ii Scale bars: 10 μm. Right: Layer distribution of R7 and R8 inputs to three Dm11 cells. Diii: Rendering of a confocal image of MultiColor FlpOut (MCFO) labelled Dm11 cells. Note the characteristic vertical projections leaving the medulla neuropile (arrow). The dashed line marks the approximate boundary of the medulla neuropile. Scale bar: 20 μm. **E.** Synapses between R7 and R8 and Dm2 cells. Ei: Top

1676 view of a fully reconstructed Dm2 skeleton, with R7 (purple) and R8 (green) synapses. Eii,

1677 Left: Side view of layer distribution of photoreceptor synapses onto the same Dm2 cell. Ei-ii

1678 Scale bars: 10 μm. Right: Layer distribution of R7 and R8 inputs to four Dm2 cells.

1679

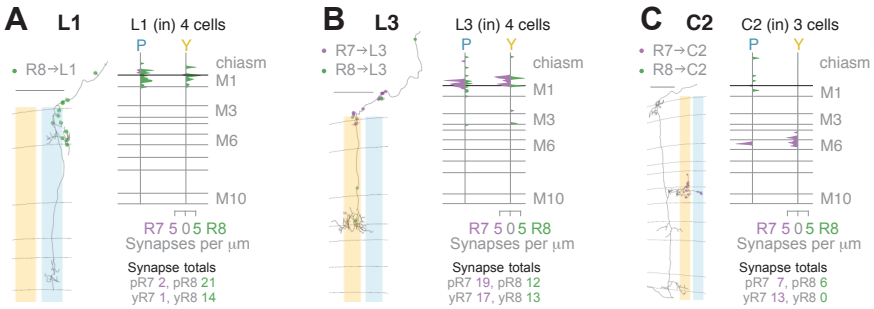

Figure 2 – figure supplement 1

1680 Figure 2 – figure supplement 1: Lamina cell types targeted by central eye R7 and R8

1681 **A**. Left: Side view of a reconstructed L1 cell (gray) with R8→L1 synapses (green). Right: Layer
1682 distribution (in synapses/µm) of all R7 and R8 inputs to 4 L1 cells. B**.** Left: Side view of a
1683 reconstructed L3 cell (gray), with R7→L3 (purple) and R8→L3 synapses (green). Right: Layer
1684 distribution (in synapses/µm) of all R7 and R8 inputs to 4 L3 cells. **C.** Left: Side view of a
1685 reconstructed C2 cell (gray), with R7→C2 (purple) and R8→C2 synapses (green). Right: Layer
1686 distribution (in synapses/µm) of all R7 and R8 inputs to 4 C2 cells. **A-C.** All scale bars: 10 µm.

1687

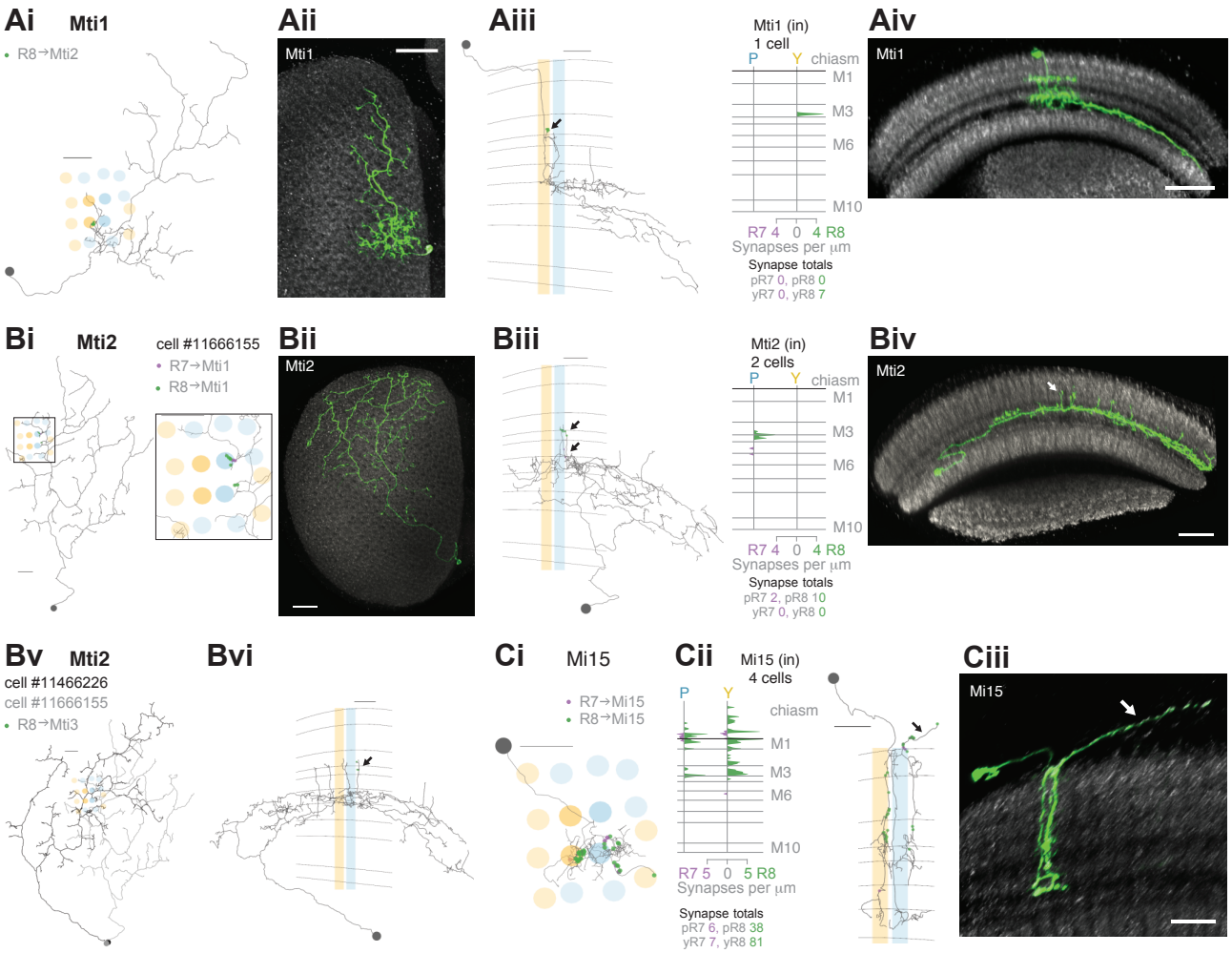
Ai
Mti1
R8→Mti2
Aii
Mti1
Aiii
Mti1 (in)
1 cell
P
Y
chiasm
M1
M3
M6
M10
R7 4 0 4 R8
Synapses per µm
Synapse totals
pR7 0, pR8 0
yR7 0, yR8 7
Aiv
Mti1
Bi
Mti2
cell #11666155
R7→Mti1
R8→Mti1
Bii
Mti2
Biii
Mti2 (in)
2 cells
P
Y
chiasm
M1
M3
M6
M10
R7 4 0 4 R8
Synapse totals
pR7 2, pR8 10
yR7 0, yR8 0
Biv
Mti2
Bv
Mti2
cell #11466226
cell #11666155
R8→Mti3
Bvi
Ci
Mi15
R7→Mi15
R8→Mi15
Cii
Mi15 (in)
4 cells
P
Y
chiasm
M1
M3
M6
M10
R7 5 0 5 R8
Synapses per µm
Synapse totals
pR7 6, pR8 38
yR7 7, yR8 81
Ciii
Mi15

Figure 3

Figure 3: Central eye R7 and R8 connections to Mi and Mti cells

A. Synapses of central R7 and R8 with Mti1 cells. Ai: Top view of an Mti1 skeleton with synapses from seed column R8 cells (green). Scale bar: 10 μm. Aii: Top view of an MCFO-labeled cell matching overall Mti1 morphology. Scale bar: 20 μm. Aiii: Side view of the same Mti1 cell and R8 (green) synapses. Scale bar: 10 μm. Aiv: Side view rendering of the same light microscopy Mti1 image (green). Scale bar: 20 μm. **B.** Synapses from R7 and R8 to Mti2. Bi: Top view of a reconstructed Mti2 cell, with R7 (purple) and R8 (green) synapses. Scale bar: 10 μm. Bii: Top view of an MCFO-labeled cell matching overall Mti2 morphology. Scale bar: 20 μm. Biii: Side view of the same Mti2 skeleton as in Bi with R7 (purple) and R8 (green) synapses on characteristic vertical projections (arrow). Scale bar: 10 μm. Biv: Side view of the cell shown in Bii. Arrow indicates vertical projections. Scale bar: 20 μm. Bv: Top view of a second reconstructed Mti2 cell (dark gray) overlayed on the first (pale gray), with R8 (green) synapses. Bvi: Side view of the second Mti2 skeleton, with R8 (green) synapses again located on vertical projections (arrow). Bv-vi Scale bars: 10 μm. **C.** Synapses of R7 and R8 with Mi15 cells. Ci: Top view of a fully reconstructed Mi15 skeleton, with R7 (purple) and R8 (green) synapses. Cii, left: Side view depicting the layer distribution of photoreceptor synapses (same color code) onto the same Mi15 skeleton, with synapses outside the medulla (arrow). Ci-ii Scale bars: 10 μm. Right: Layer distribution of R7 and R8 inputs to four Mi15 cells. Ciii: Side view rendering of a light microscopy image (MCFO) of an Mi15 cell. Note the long process leaving the medulla (arrow). Scale bar: 10 μm.

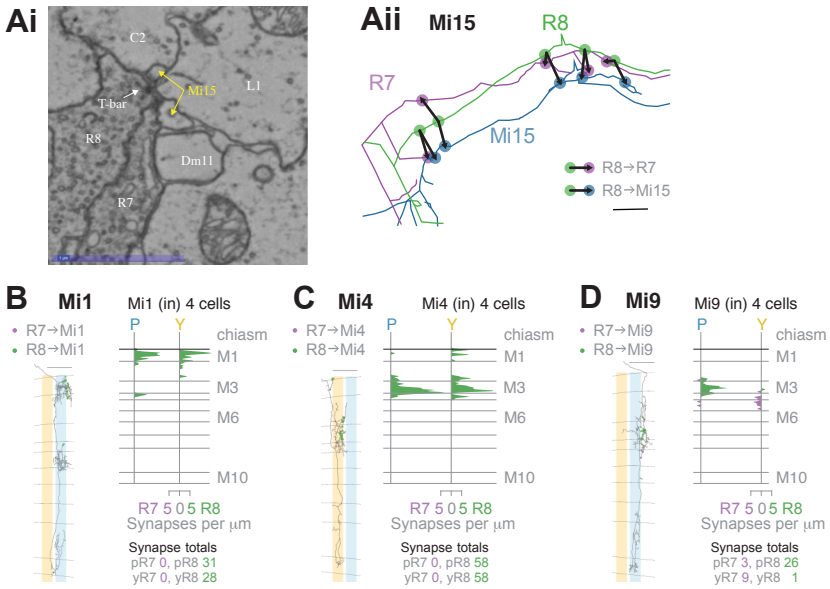

Figure 3 – figure supplement 1

Figure 3 – figure supplement 1: Medulla intrinsic cell types targeted by central eye R7 and R8

A. Colocalization of R8→Mi15 synapses with R8→R7 synapses. Ai. Example EM-image of Mi15 and R7 cells as postsynaptic partners of the same R8 presynapse. Scale bar: 1 μm. Aii. Magnified view of skeletons of R8, Mi15, and R7 cells in the optic chiasm, illustrating the colocalization of R8→Mi15 synapses with R8→R7 synapses at 5 successive locations. Scale bar: 1 μm. **B**. Left: Side view of a reconstructed Mi1 cell (gray) with R7→Mi1 (purple) and R8→Mi1 synapses (green). Right: Layer distribution (in synapses/μm) of all R7 and R8 inputs to 4 Mi1 cells. **C**. Left: Side view of a reconstructed Mi4 cell (gray) with R7→Mi4 (purple) and R8→Mi4 synapses (green). Right: Layer distribution (in synapses/μm) of all R7 and R8 inputs to 4 Mi4 cells. **D**. Left: Side view of a reconstructed Mi9 cell (gray) with R7→Mi9 (purple) and R8→Mi9 synapses (green). Right: Layer distribution (in synapses/μm) of all R7 and R8 inputs to 4 Mi9 cells. In the pale seed columns, Mi9 cells received many R8 synapses, but only received 1 R8 synapse in the yellow seed columns. **B-D.** Scale bars: 10 μm.

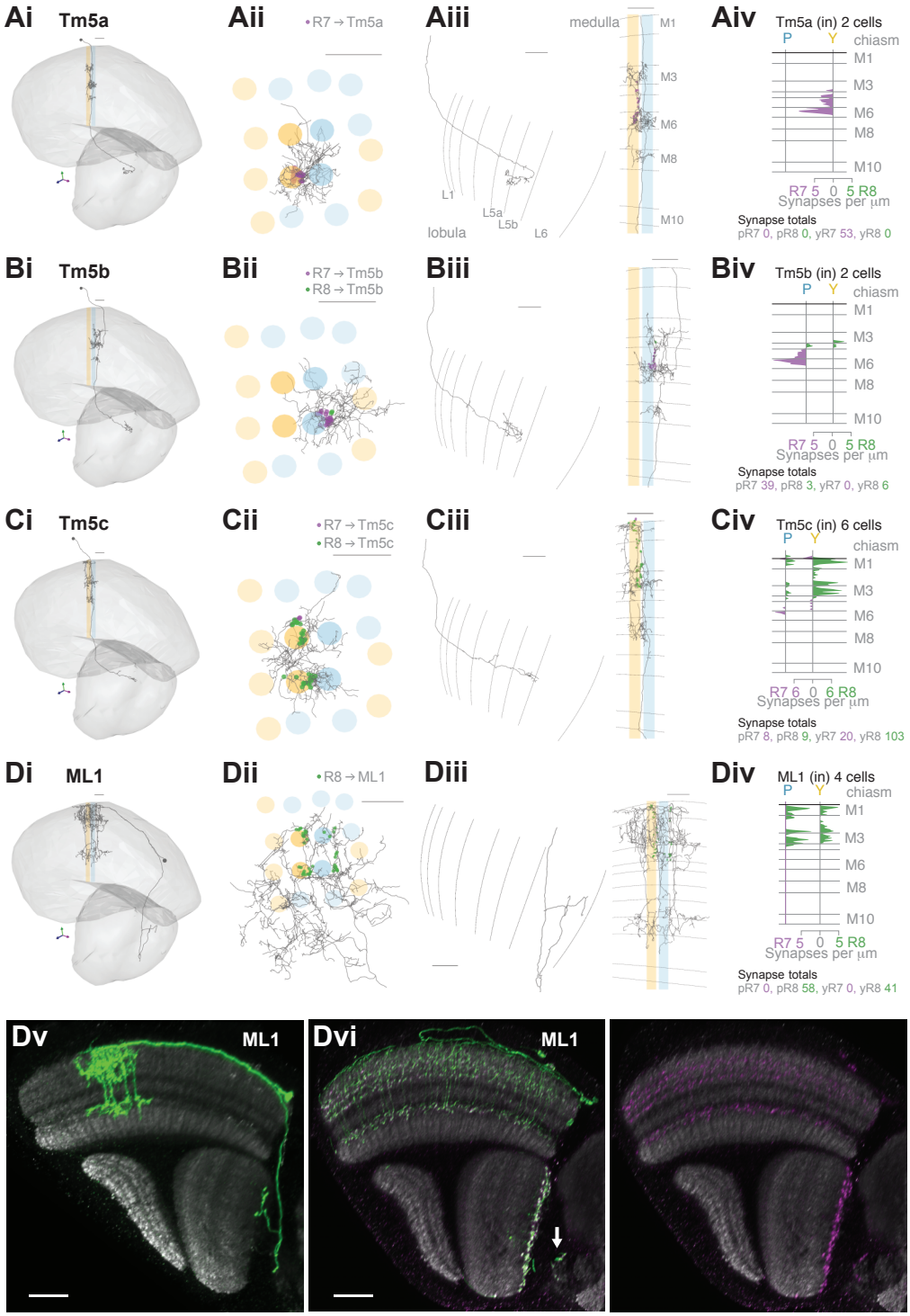
Ai
Tm5a
Aii
R7 → Tm5a
Aiii
medulla
M1
M3
M6
M8
M10
L1
L5a
L5b
L6
lobula
Aiv
Tm5a (in) 2 cells
P
Y
chiasm
M1
M3
M6
M8
M10
R7 5 0 5 R8
Synapses per µm
Synapse totals
pR7 0, pR8 0, yR7 53, yR8 0
Bi
Tm5b
Bii
R7 → Tm5b
R8 → Tm5b
Biii
Biv
Tm5b (in) 2 cells
P
Y
chiasm
M1
M3
M6
M8
M10
R7 5 0 5 R8
Synapses per µm
Synapse totals
pR7 39, pR8 3, yR7 0, yR8 6
Ci
Tm5c
Cii
R7 → Tm5c
R8 → Tm5c
Ciii
Civ
Tm5c (in) 6 cells
P
Y
chiasm
M1
M3
M6
M8
M10
R7 6 0 6 R8
Synapses per µm
Synapse totals
pR7 8, pR8 9, yR7 20, yR8 103
Di
ML1
Dii
R8 → ML1
Diii
Div
ML1 (in) 4 cells
P
Y
chiasm
M1
M3
M6
M8
M10
R7 5 0 5 R8
Synapses per µm
Synapse totals
pR7 0, pR8 58, yR7 0, yR8 41
Dv
ML1
Dvi
ML1

Figure 4

Figure 4: Central eye R7 and R8 connections with cells projecting to the lobula

A-D. Synapses between R7 and R8 and Tm5a (A), Tm5b (B), Tm5c (C) and ML1 (D) cell types. Panels **i-iii**: Anatomy of fully reconstructed cells. **i**: Side view. **ii**: Top view. **iii**, Left: Side view of axon terminals in the lobula. Right: Side view of medulla branches. R7 synapses are indicated in purple, R8 synapses in green in ii, iii (Right). **iv**: Layer distribution of R7 and R8 inputs. Scale bars: 10 μm. **A.** Tm5a. The two Tm5a cells were exclusively targeted by yellow R7 cells. **B.** Tm5b. The two Tm5b cells were highly biased to pale R7 inputs. **C.** Tm5c. The five Tm5ccells were highly biased to yellow R8 inputs. **D.** ML1. Dv: Reconstructed side view of a single MCFO-labeled ML1 cell (Light microscopy). Note this cell has terminals both at the base of the deepest lobula layer and in the central brain; not all ML1 cells have terminals in the central brain. Scale bar: 20 μm. Dvi: Reconstructed side view showing the distribution of a membrane marker (green) and presynaptic marker synaptotagmin-HA (purple) in ML1 cells imaged as a population. The combined patterns (Left), and the presynaptic marker alone (Right) are shown. Arrow indicates central brain terminals. Scale bar: 20 μm.

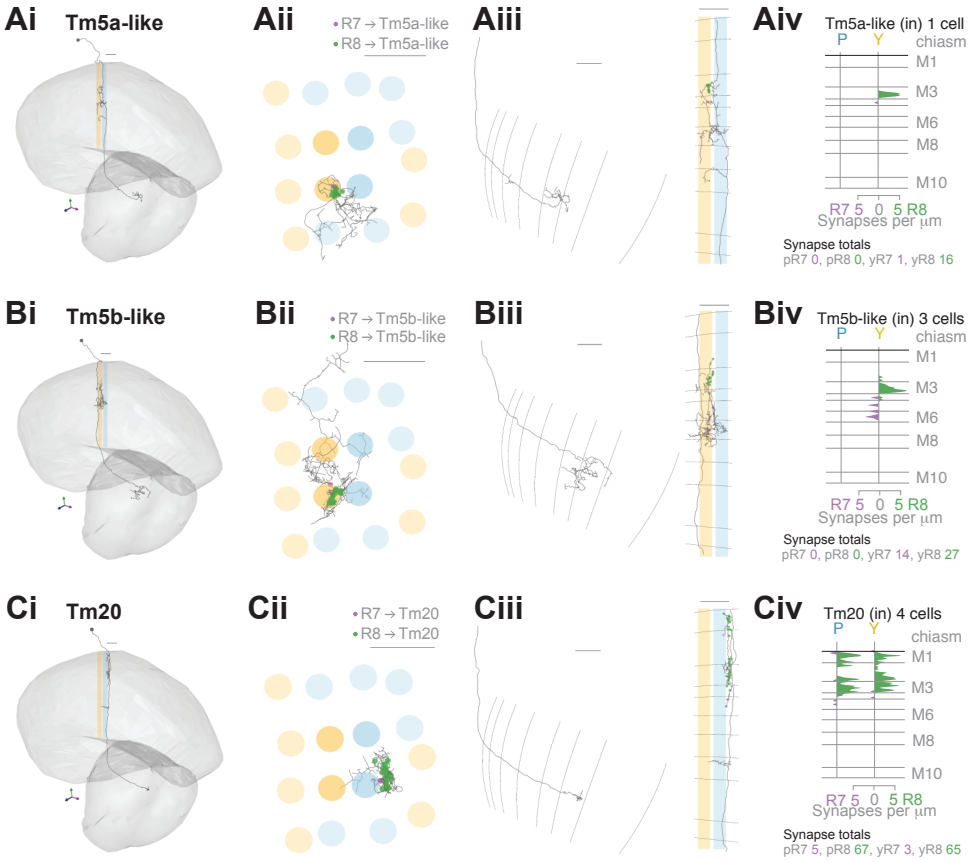

Figure 4 – figure supplement 1

Figure 4 – figure supplement 1: Additional connections of central R7 and R8 to cell types projecting into the lobula neuropil

A. R7 and R8 connections with the Tm5a-like cell, that has a morphology similar to a Tm5a cell, but a different pattern of connectivity. The same reconstructed cell is shown in Ai-iii. Ai: Side view. Aii: Top view with R7 (purple) and R8 (green) synapses. Aiii: Left: The axon terminals in the lobula. Right: Side view with R7 (purple) and R8 (green) synapses. Aiv: Layer distribution (in synapses/µm) of all R7 and R8 inputs from four seed columns to the Tm5a-like cell. **B.** R7 and R8 connections with three Tm5b-like cells, that each have a morphology similar to a Tm5b cell, but a different, shared pattern of connectivity. The same reconstructed Tm5b-like cell is shown in Bi-iii. Bi: Side view. Bii: Top view with R7 (purple) and R8 (green) synapses. Biii: Left: The axon terminals in the lobula. Right: Side view with R7 (purple) and R8 (green) synapses. Biv: Layer distribution (in synapses/µm) of all R7 and R8 inputs from four seed columns to the three Tm5b-like cells. Unlike the Tm5b cells, the Tm5b-like cells are predominantly targeted by yellow R8 photoreceptors. **C.** R7 and R8 connections with Tm20 cells. The same reconstructed Tm20 cell is shown in Ci-iii. Ci: Side view. Cii: Top view with R7 (purple) and R8 (green) synapses. Ciii: Left: The axon terminals in the lobula. Right: Side view with R7 (purple) and R8 (green) synapses. Civ: Layer distribution (in synapses/µm) of all R7 and R8 inputs from four seed columns to the four Tm20 cells. **A-C.** Scale bars: 10 µm.

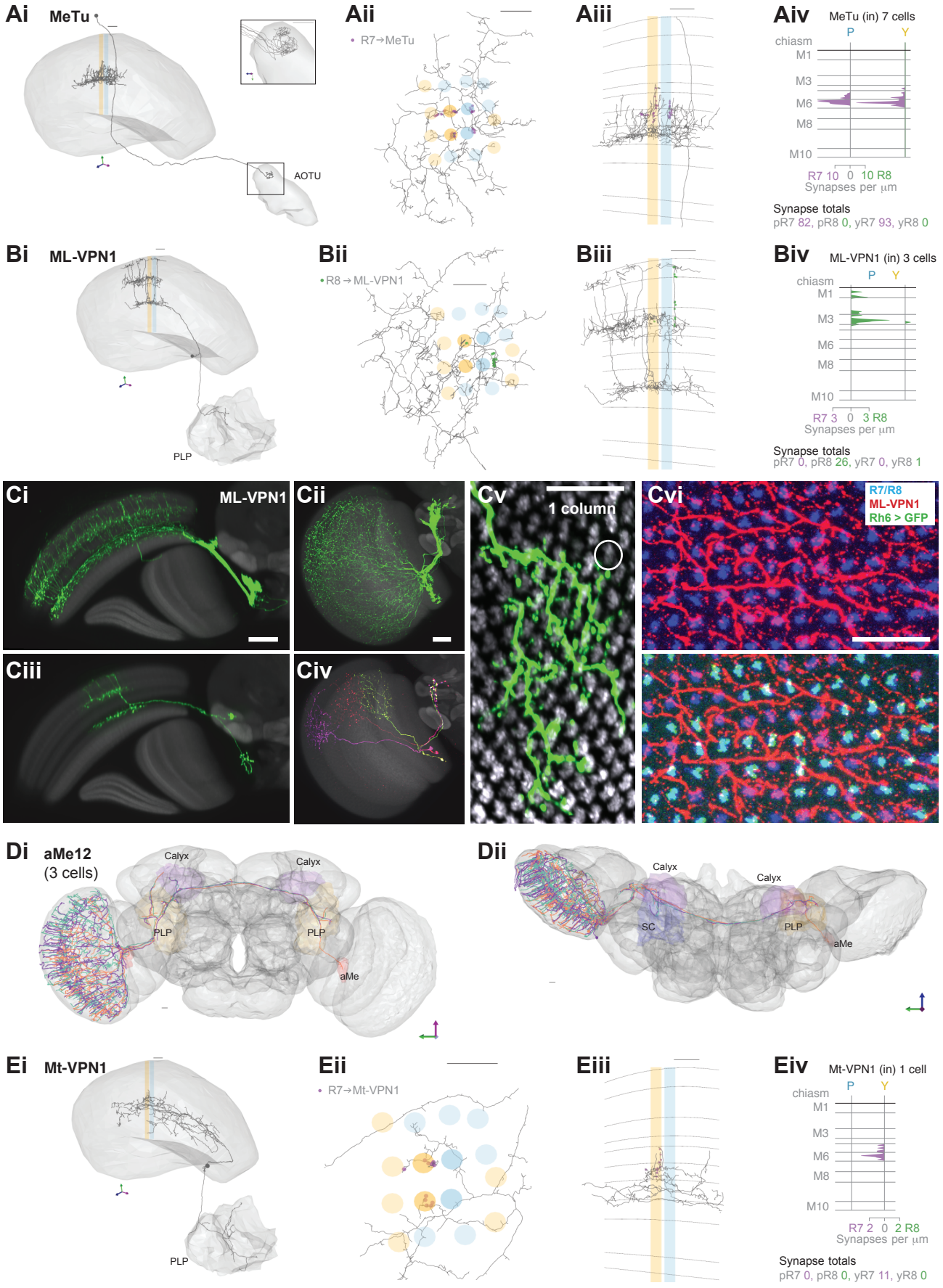
Ai
MeTu
AOTU
Aii
R7→MeTu
Aiii
Aiv
MeTu (in) 7 cells
P
Y
chiasm
M1
M3
M6
M8
M10
R7 10 0 10 R8
Synapses per µm
Synapse totals
pR7 82, pR8 0, yR7 93, yR8 0
Bi
ML-VPN1
PLP
Bii
R8→ML-VPN1
Biii
Biv
ML-VPN1 (in) 3 cells
R7 3 0 3 R8
Synapses per µm
Synapse totals
pR7 0, pR8 26, yR7 0, yR8 1
Ci
ML-VPN1
Cii
Ciii
Civ
Cv
1 column
Cvi
R7/R8
ML-VPN1
Rh6 > GFP
Di
aMe12
(3 cells)
Calyx
Calyx
PLP
PLP
aMe
Dii
Calyx
Calyx
SC
PLP
aMe
Ei
Mt-VPN1
PLP
Eii
R7→Mt-VPN1
Eiii
Eiv
Mt-VPN1 (in) 1 cell
R7 2 0 2 R8
Synapses per µm
Synapse totals
pR7 0, pR8 0, yR7 11, yR8 0

Figure 5

Figure 5: Interneurons connecting central eye R7 and R8 with the central brain

A,B,E. Synapses between R7 and R8 and MeTu (A), ML-VPN1 (B) and Mt-VPN1 (E) cells. Panels **i-iii**: Anatomy of reconstructed cells. **i**: Side view. **ii**: Top view. **iii**: Side view of medulla branches. R7 synapses are indicated in purple, R8 synapses in green in ii, iii. **iv**: Layer distribution of R7 and R8 inputs. Scale bars: 10 μm. **A**. The MeTu cell shown was fully reconstructed. Ai. Inset shows a magnified view of axon projections to the AOTU. Aiv: All seven MeTu cells were exclusively R7 targets. **B.** The ML-VPN1 cell shown was fully reconstructed. Bi. ML-VPN1 cells project to the PLP. Biv. Both ML-VPN1 cells were pale R8 targets. **Ci-vi**: Light miscroscopy of ML-VPN1 anatomy. Ci,Cii: Side view (Ci) and top view (Cii) of the population of ML-VPN1 cells. Ciii: Side view of a single MCFO-labeled ML-VPN1 cells. Civ: Top view of multiple MCFO-labeled ML-VPN1 cells. Cv: Overlay of arbors of a single cell ML-VPN1 cell with L2 terminals (gray) indicating medulla columns. Images in Ci-Cv show overlays of aligned confocal images with the standard brain used for registration (Ci-iv) or a second registered image showing L2 terminals (Cv). Cvi: Confocal substack projection showing medulla columns at approximately the level of R8 terminals. ML-VPN1 (red) and photoreceptor axons (blue) are shown without (top) and with (bottom) labelling of yellow R8 axons (Rh6 > green). Overlap between ML1 and photoreceptos is largely limited to pale columns (i.e. columns without the Rh6 marker). **Cv-vi** Scale bars: 20 μm. **D.** Reconstructions of three aMe12 cells (orange, green, purple) covering the entire medulla, with axons leaving via the accessory medulla and innervating the mushroom body calyces (Calyx) and the PLP and accessory medulla (aMe) of both hemispheres. Di: Frontal view. Dii: Dorsal view. **E.** Mt-VPN1 cells. Eiv: Tracing of Mt-VPN1 photoreceptor synapses in 16 additional columns did not confirm yellow specificity found in the seed columns.

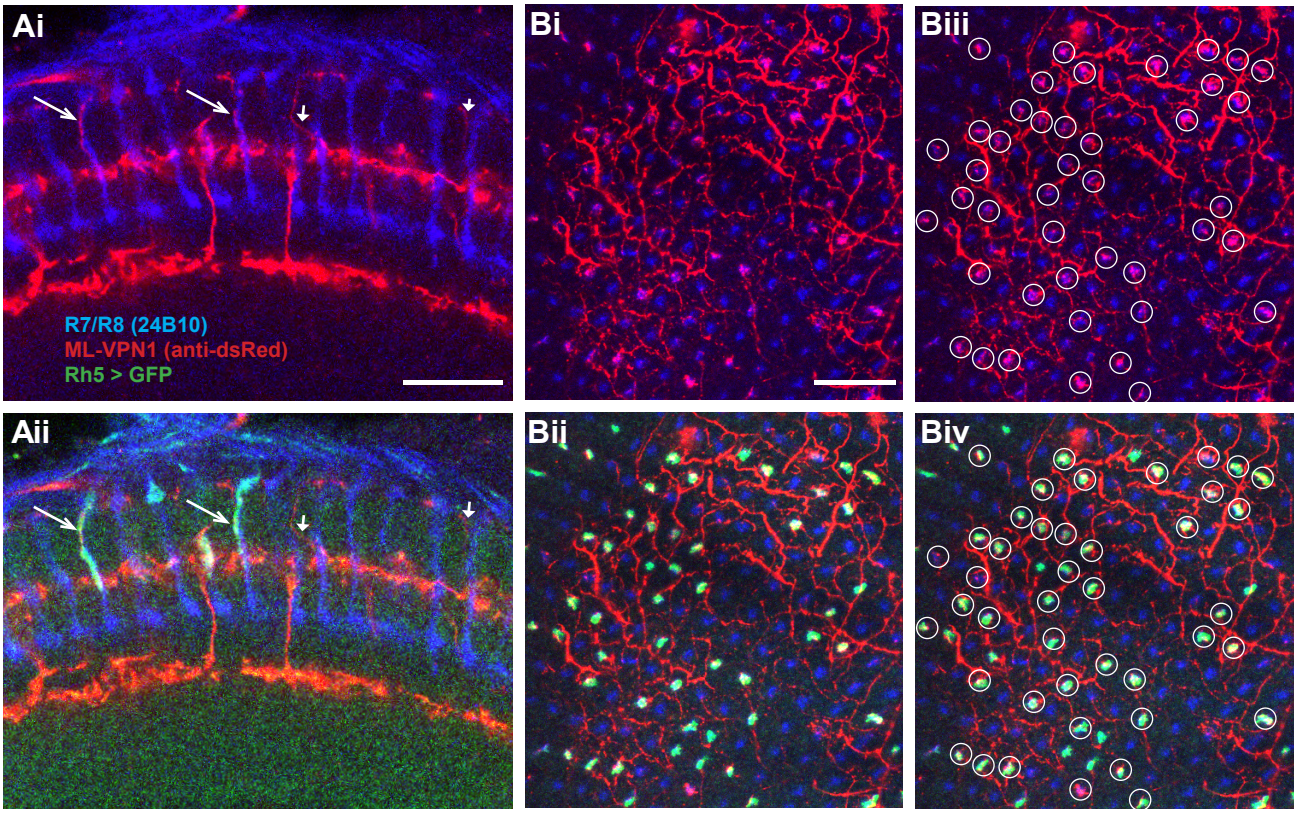

Figure 5 – figure supplement 1

Figure 5 – figure supplement 1: Pale specificity of ML-VPN1 in the central eye seed columns

A. Side view of R7 and R8 photoreceptors (blue) and ML-VPN1 cells (red), without (Ai) and with (Aii) Rh5 expression (green). Ai. Four vertical processes that traverse layers 1-3 are labelled by arrows. In our EM reconstructions the photoreceptor synapses were largely located on such characteristic processes. Most vertical processes that followed photoreceptors, such as the two examples indicated by long, open arrows were in pale (Rh5-positive) columns. Other vertical processes that did not follow photoreceptors (short, closed arrows) were also frequently found in yellow (Rh5-negative) columns or could not be readily assigned to a column. **B**. Projection through a few adjacent confocal slices showing ML-VPN1 and photoreceptor axons at approximately the level of R8 terminals, with color labelling as in A. without (Bi) and with (Bii) pale R8 columns labelled by the Rh5 marker. Overlap between ML1 and R-cells is largely limited to pale columns. For example, out of 43 putative overlaps circled (Biii), only four did not overlap with pale R8 expression (Biv), indicating that 93% of putative innervated columns were of a pale fate in this image. **A-B** Scale bars: 20 μm.

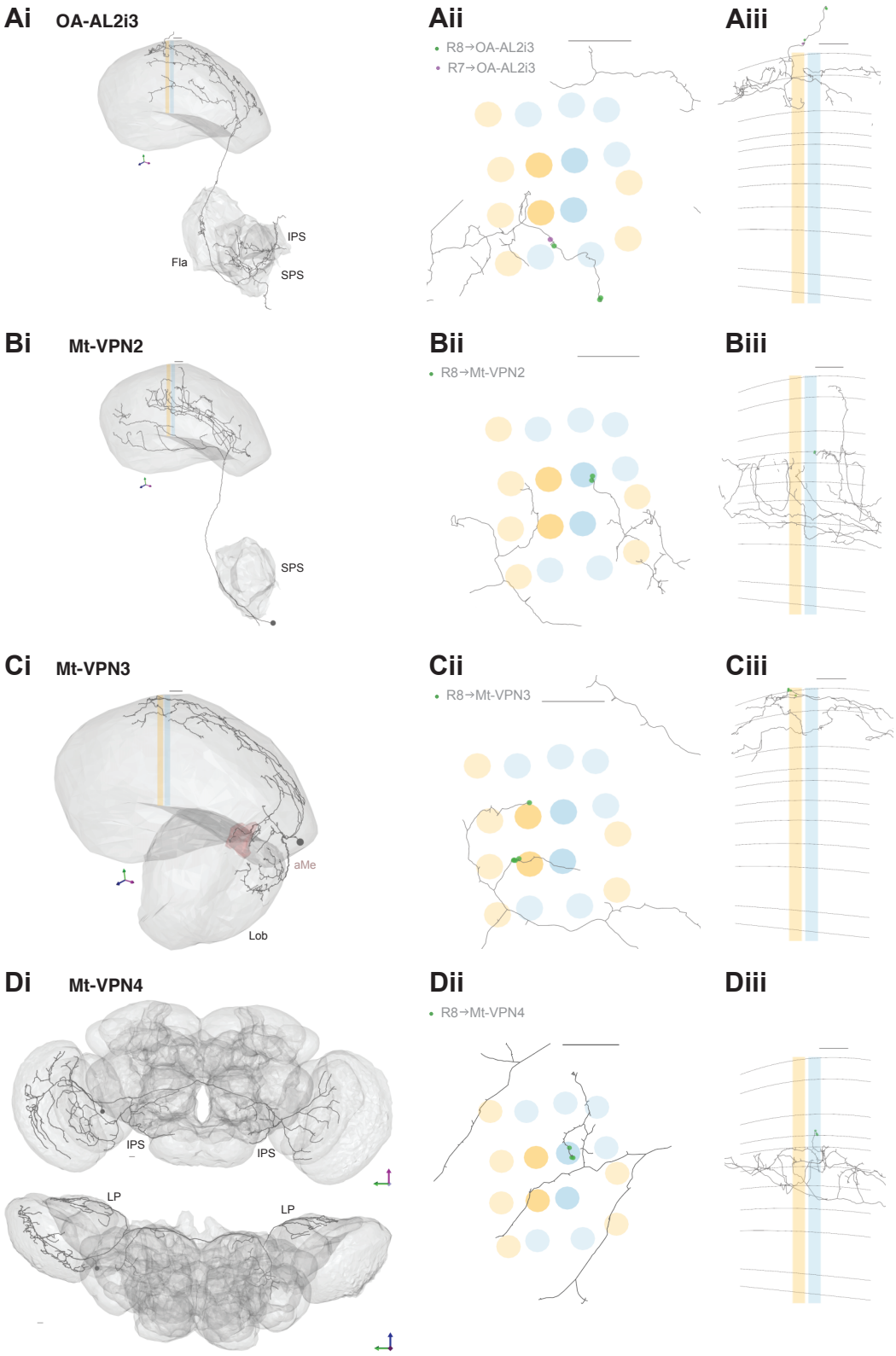

Figure 5 – figure supplement 2

Figure 5 – figure supplement 2: Weakly connected visual projection neurons connecting central eye R7 and R8 to the central brain

A. R7 and R8 connections with a Mt-VPN matching the anatomy of a known octopaminergic cell type (OA-AL2i3). The same reconstructed cell is shown in Ai-iii. Ai: Side view, showing the projections to the flange (Fla), inferior posterior slope (IPS), and superior posterior slope (SPS). Aii: Top view with R7 (purple) and R8 (green) synapses. Aiii: Side view with R7 (purple) and R8 (green) synapses. The cell has processes leaving the medulla that track the photoreceptors, where it received synaptic inpu in our seed columns. **B.** R8 connections with the reconstructed Mt-VPN2 cell. Bi: Side view, showing the projection to the SPS. Bii: Top view with R8 (green) synapses. Biii: Side view with R8 (green) synapses. **C.** R8 connections with the reconstructed Mt-VPN3 cell. Ci: Side view, showing the projections to the lobula (Lob) and accessory medulla (aMe). Cii: Top view with R8 (green) synapses. Ciii: Side view with R8 (green) synapses. **D.** R8 connections with the reconstructed Mt-VPN4 cell, which is also a heterolateral lobula late tangential cell. Di: Side view, showing the projections to the lobula plate (LP) and IPS in both hemispheres. Dii: Top view with R8 (green) synapses. Diii: Side view with R8 (green) synapses. **A-D.** Scale bars: 10 μm.

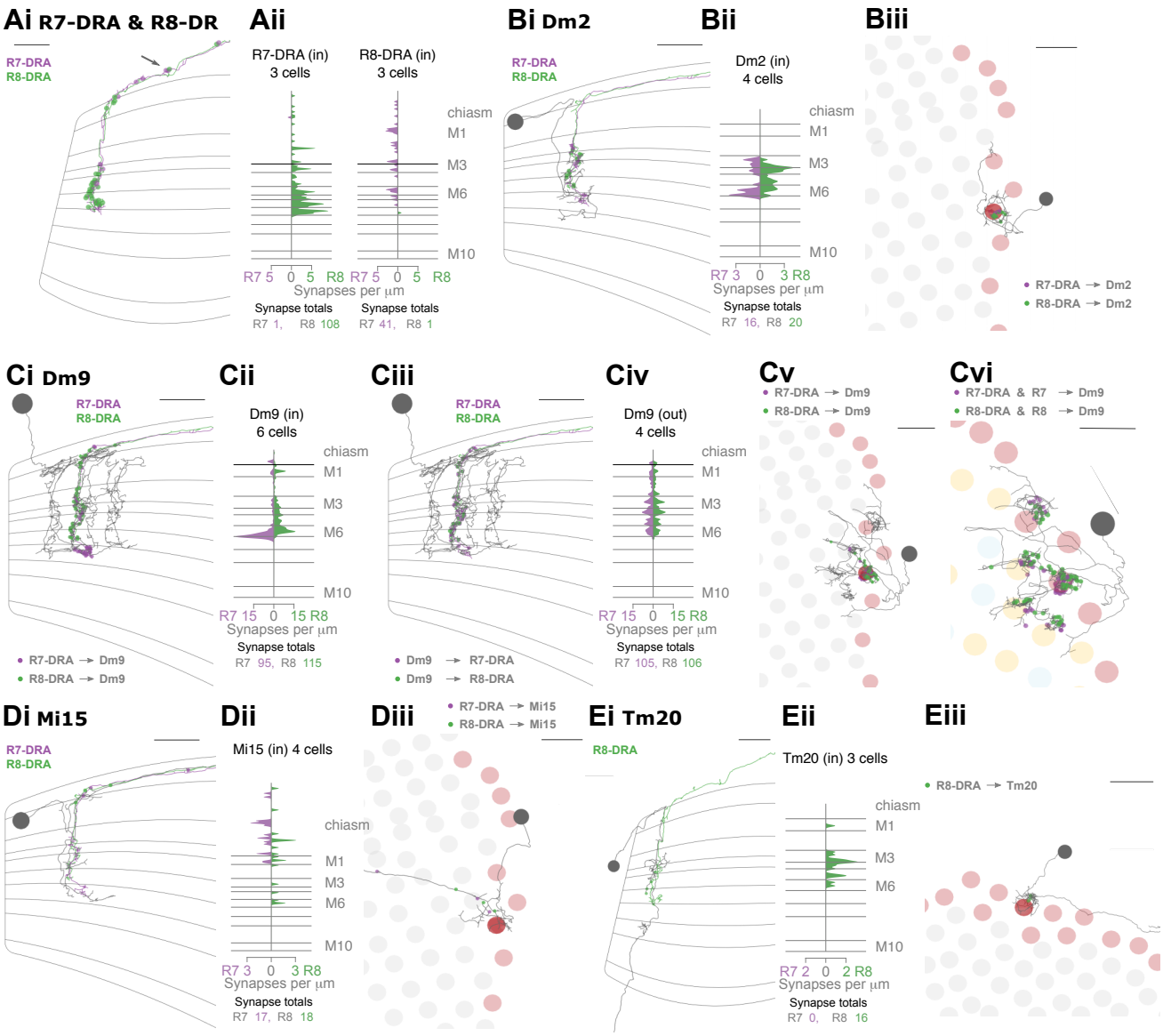
Ai R7-DRA & R8-DR
R7-DRA
R8-DRA
Aii
R7-DRA (in)
3 cells
R8-DRA (in)
3 cells
chiasm
M1
M3
M6
M10
R7 5 0 5 R8
R7 5 0 5 R8
Synapses per µm
Synapse totals
R7 1, R8 108
Synapse totals
R7 41, R8 1
Bi Dm2
R7-DRA
R8-DRA
Bii
Dm2 (in)
4 cells
chiasm
M1
M3
M6
M10
R7 3 0 3 R8
Synapses per µm
Synapse totals
R7 16, R8 20
Biii
R7-DRA → Dm2
R8-DRA → Dm2
Ci Dm9
R7-DRA
R8-DRA
R7-DRA → Dm9
R8-DRA → Dm9
Cii
Dm9 (in)
6 cells
chiasm
M1
M3
M6
M10
R7 15 0 15 R8
Synapses per µm
Synapse totals
R7 95, R8 115
Ciii
R7-DRA
R8-DRA
Dm9 → R7-DRA
Dm9 → R8-DRA
Civ
Dm9 (out)
4 cells
chiasm
M1
M3
M6
M10
R7 15 0 15 R8
Synapses per µm
Synapse totals
R7 105, R8 106
Cv
R7-DRA → Dm9
R8-DRA → Dm9
Cvi
R7-DRA & R7 → Dm9
R8-DRA & R8 → Dm9
Di Mi15
R7-DRA
R8-DRA
Dii
Mi15 (in) 4 cells
chiasm
M1
M3
M6
M10
R7 3 0 3 R8
Synapses per µm
Synapse totals
R7 17, R8 18
Diii
R7-DRA → Mi15
R8-DRA → Mi15
Ei Tm20
R8-DRA
Eii
Tm20 (in) 3 cells
chiasm
M1
M3
M6
M10
R7 2 0 2 R8
Synapses per µm
Synapse totals
R7 0, R8 16
Eiii
R8-DRA → Tm20

Figure 6

Figure 6: Synapses of R7 and R8 with each other and different medulla cell types in the DRA

A. Reciprocal synapses between R7 and R8 in the DRA. Ai: Side view of an R7- and R8-DRA cell with R7-DRA→R8-DRA (purple points) and R8-DRA→R7-DRA (green points Aii: Layer distribution of R7-DRA and R8-DRA reciprocal synapses in three columns. **B.** Synapses between DRA R7 and R8 photoreceptors and Dm2 cells. Bi: Reconstruction of a Dm2 cells with synapses from R7-DRA (purple) and R8-DRA (green). Bii: Layer distribution of R7-DRA and R8-DRA synapses onto 4 Dm2 cells. Biii: Top view of Dm2 skeleton in the DRA. **C.** Reciprocal synapses between Dm9 cells in the DRA and R7-DRA / R8-DRA. Ci: Side view of a fully reconstructed Dm9 skeleton (grey) in the DRA region, with R7-DRA→Dm9 synapses (purple) and R8-DRA→Dm9 synapses (green). Cii: Layer distribution of DRA photoreceptor inputs into Dm9. Ciii: Feedback synapses from Dm9 to R7-DRA (purple) and R8-DRA (green) photoreceptors. Civ: Layer distribution of Dm9 inputs into DRA inner photoreceptors. Cv: Top view of a Dm9 cell that connects to photoreceptors in both DRA (light red) and non-DRA columns (grey). Synapses from R7-DRA (purple) and R8-DRA (green) are indicated. Cvi: DRA and non-DRA R7 (purple) and R8 (green) inputs into the same Dm9 as in (Cv). **D.** Synapses between DRA R7 and R8 and Mi15. Di: Side view of a reconstructed Mi15 with R7-DRA→Mi15 synapses (purple) and R8-DRA→Mi15 synapses (green). Dii: Layer distribution of R7-DRA and R8-DRA input to 4 Mi15 cells. Diii: Top view of Mi15 skeleton in the DRA. **E.** Synapses between DRA R7 and R8 photoreceptors and Tm20 cells. Ei: Side view of a reconstructed Tm20 with R8-DRA→Mi15 synapses in green. Eii: Layer distribution of R8-DRA input to 3 Tm20 cells. Eiii: Top view of Tm20 skeleton in the DRA. (All scale bars: 10 μm).

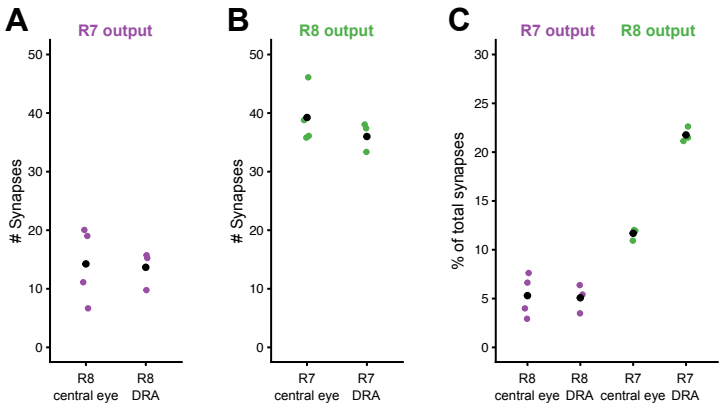

Figure 6 – figure supplement 1

Figure 6 - figure supplement 1: Reciprocal synapses of R7 and R8 in the central eye and the DRA

A. Total number of R7 synapses onto R8 for all full reconstruced cells in the central eye (4) and the DRA (3). **B**. Total number of R8 synapses onto R7 for all full reconstruced cells in the central eye (4) and the DRA (3). **C**. Fraction of photoreceptor-to-photoreceptor synapses of the total output of R7 and R8 in the central eye and the DRA.

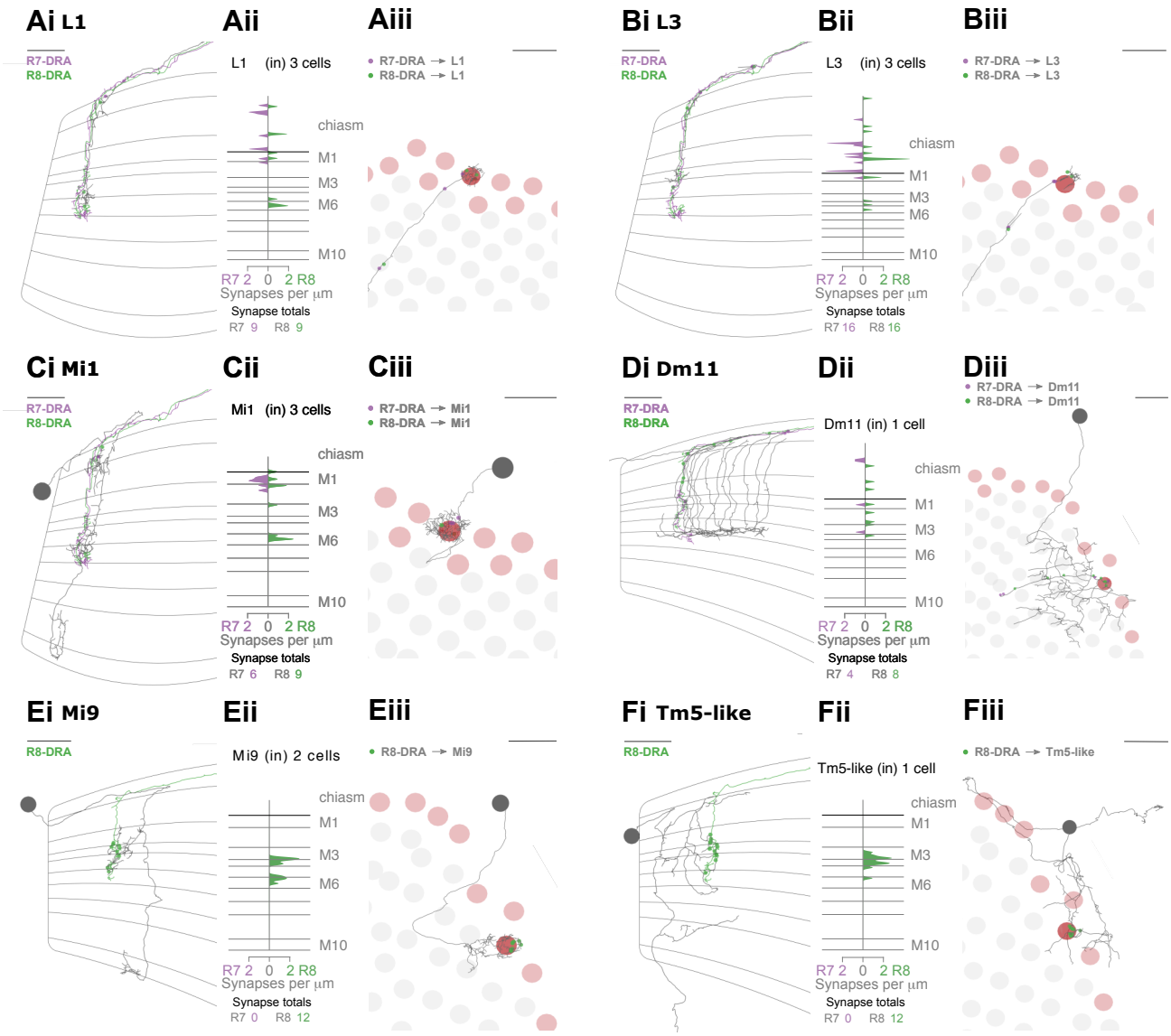

Figure 6 – figure supplement 2

Figure 6 – figure supplement 2: additional cell types connected to R7 and R8 in the DRA with lower synaptic strength

A. Synapses between DRA photoreceptors and L1. Ai: Side view of a reconstructed L1 skeleton (dark grey), together with R7-DRA (purple) and R8-DRA (green) from the same column plus R7-DRA→L1 synapses (purple) and R8-DRA→L1 synapses (green). Aii: Synapse distribution (in synapses/µm) of all three reconstructed L1 cells from the three DRA seed columns across medulla layers. Aiii Top view of the same L1 cell with R7-DRA→L1 synapses (purple) and R8-DRA→L1 synapses (green). **B**. Synapses between DRA photoreceptors and L3. Bi: Side view of a reconstructed L3 skeleton (dark grey), together with R7-DRA (purple) and R8-DRA (green) from the same column plus R7-DRA→L3 synapses (purple) and R8-DRA→L3 synapses (green). Bii: Synapse distribution (in synapses/µm) of all three reconstructed L3 cells from the three DRA seed columns across medulla layers. Biii Top view of the same L3 cell with R7-DRA→L3 synapses (purple) and R8-DRA→L3 synapses (green). **C**. Synapses between DRA photoreceptors and Mi1. Ci: Side view of a reconstructed Mi1 skeleton (dark grey), together with R7-DRA (purple) and R8-DRA (green) from the same column plus R7-DRA→Mi1 synapses (purple) and R8-DRA→Mi1 synapses (green). Cii: Synapse distribution (in synapses/µm) of all three reconstructed Mi1 cells from the three DRA seed columns across medulla layers. Ciii Top view of the same Mi1 cell with R7-DRA→Mi1 synapses (purple) and R8-DRA→Mi1 synapses (green). **D**. Synapses between DRA photoreceptors and Dm11. Di: Side view of a reconstructed Dm11 skeleton (dark grey), together with R7-DRA (purple) and R8-DRA (green) from the same column plus R7-DRA→Dm11 synapses (purple) and R8-DRA→Dm11 synapses (green). Dii: Synapse distribution (in synapses/µm) of one reconstructed Dm11 cells from the three DRA seed columns across medulla layers. Note that synapses between PR→Dm11 were only found in one of the three DRA seed columns. Diii Top view of the same Dm11 cell with R7-DRA→Dm11 synapses (purple) and R8-DRA→Dm11 synapses (green). **E.** Synapses between R8-DRA and Mi9. Ei: Side view of a reconstructed Mi9 skeleton (dark grey), together with R8-DRA (green) from the same column plus R8-DRA→Mi9 synapses (green). Eii: Synapse distribution (in

synapses/µm) of two reconstructed Mi9 cells from the three DRA seed columns across medulla layers. Note that only in two of the three DRA seed columns PR→Mi9 synapses were found. Eiii Top view of the same Mi9 cell with R8-DRA→Mi9 synapses (green). **F**. Synapses between R8-DRA and a Tm5-like cell. Fi: Side view of the reconstructed Tm5-like skeleton (dark grey), together with R8-DRA (green) from the same column plus R8-DRA→ Tm5-like synapses (green). Fii: Synapse distribution (in synapses/µm) of the one Tm5-like cell from the three DRA seed columns across medulla layers. Note that only in one of the three DRA seed columns such a cell was found. Fiii Top view of the same Tm5-like cell with R8-DRA→Tm5-like synapses (green).

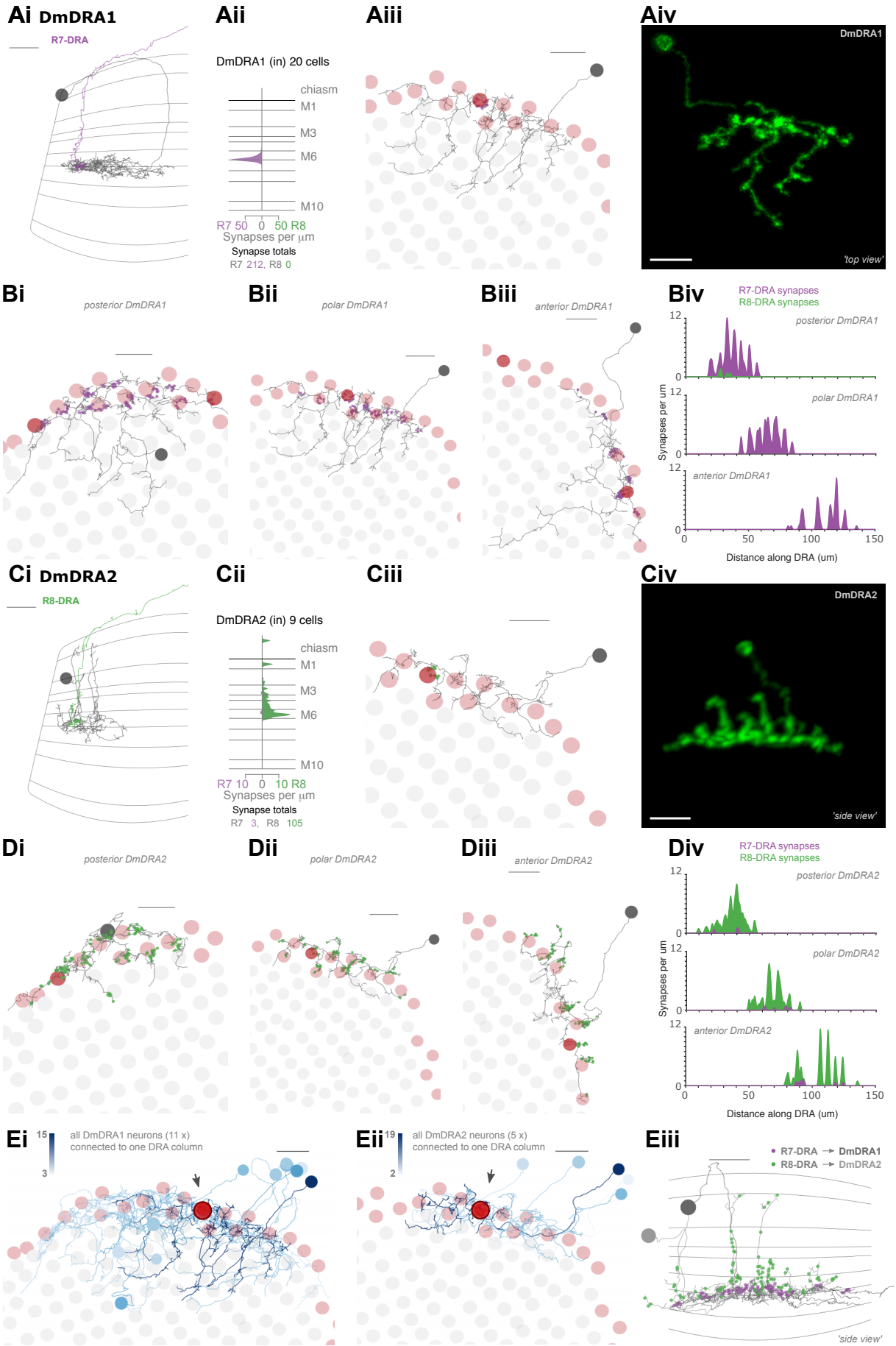
Ai DmDRA1
R7-DRA
Aii
DmDRA1 (in) 20 cells
chiasm
M1
M3
M6
M10
R7 50 0 50 R8
Synapses per µm
Synapse totals
R7 212, R8 0
Aiii
Aiv
DmDRA1
'top view'
Bi
posterior DmDRA1
Bii
polar DmDRA1
Biii
anterior DmDRA1
Biv
R7-DRA synapses
R8-DRA synapses
posterior DmDRA1
polar DmDRA1
anterior DmDRA1
Synapses per um
Distance along DRA (um)
Ci DmDRA2
R8-DRA
Cii
DmDRA2 (in) 9 cells
chiasm
M1
M3
M6
M10
R7 10 0 10 R8
Synapses per µm
Synapse totals
R7 3, R8 105
Ciii
Civ
DmDRA2
'side view'
Di
posterior DmDRA2
Dii
polar DmDRA2
Diii
anterior DmDRA2
Div
R7-DRA synapses
R8-DRA synapses
posterior DmDRA2
polar DmDRA2
anterior DmDRA2
Synapses per um
Distance along DRA (um)
Ei
all DmDRA1 neurons (11 x)
connected to one DRA column
Eii
all DmDRA2 neurons (5 x)
connected to one DRA column
Eiii
R7-DRA → DmDRA1
R8-DRA → DmDRA2
'side view'

Figure 7

Figure 7: Dm8-like cells in the DRA

A. Synapses between photoreceptors and Dm-DRA1 cells. Ai: Side view of a reconstructed Dm-DRA1 (grey) innervated by DRA.R7 (purple). Aii: Distribution of DRA.R7 synapses (purple) onto 20 Dm-DRA1 cells, plotted across medulla layers. Aiii: Top view of the same fully reconstructed Dm-DRA1 skeleton and R7-DRA inputs from the seed column (purple). Aiv: Top view of a light microscopic Dm-DRA1 single cell clone with processes leaving the DRA. **B.** R7-DRA inputs into Dm-DRA1 cells. Bi-iii: Three skeletons of fully reconstructed Dm-DRA1 cells (grey) at different positions along the DRA (posterior, polar and anterior) with all R7-DRA synapses (purple) originating from an average of 11 columns. Biv: Distribution of R7-DRA synapses onto the three Dm-DRA1 cells from Bi-iii along the DRA. **C.** Synapses between photoreceptors and Dm-DRA2 cells. Ci: Side view of one reconstructed Dm-DRA2 skeleton (grey) innervated by R8-DRA (green). Cii: Layer distribution of DRA photoreceptor synapses onto 9 Dm-DRA2 cells.Ciii: Top view of the same fully reconstructed Dm-DRA2 skeleton and photoreceptor inputs from the seed column. Civ: Side view of a light microscopic Dm-DRA2 single cell clone with vertical processes. **D.** Photoreceptor inputs into Dm-DRA2 cells. Di-iii: Three skeletons of fully reconstructed Dm-DRA2 cells (grey) at different positions along the DRA (posterior, polar and anterior) with all R8-DRA (green) synapses originating from an average of 11 columns. Div: Distribution of R8-DRA (and few R7-DRA) synapses onto the three Dm-DRA2 cells from Di-iii along the DRA. **E.** Comparison of Dm-DRA1 and Dm-DRA2 connectivity. All reconstructed Dm-DRA1 skeletons connected to the same R7-DRA cell (circled column, arrow). The saturation of blue color indicates strength of connectivity (from 3 to 15 synapses). Eii: Summary all Dm-DRA2 skeletons connected to the same R8-DRA (circled column, arrow), blue color indicates the strength of connectivity (from 2 to 19 synapses). Eiii: Side views of overlapping Dm-DRA1 and Dm-DRA2 cell skeletons with all R7-DRA and R8-DRA synapses (same cells as in Bii and Dii). (All scale bars: 10 μm).

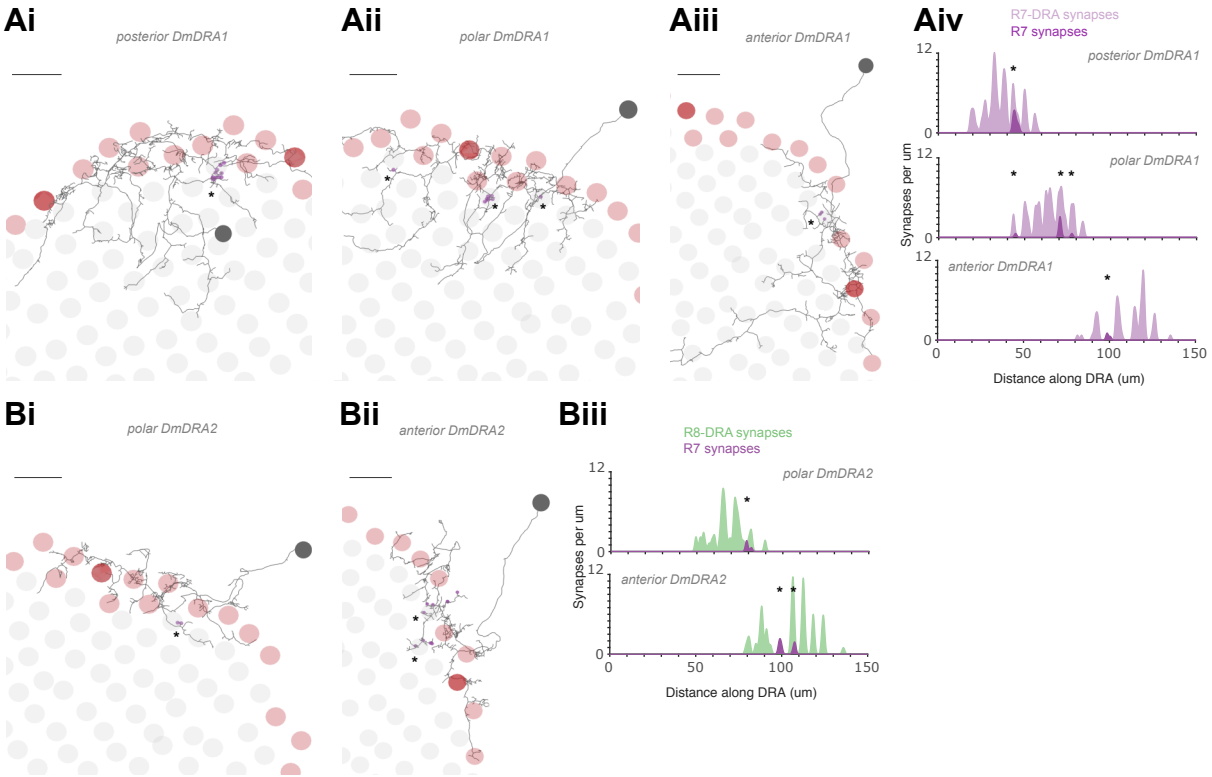

Figure 7 – figure supplement 1

Figure 7 – figure supplement 1: non-DRA photoreceptor inputs into Dm-DRA cells

A. Top view (Ai-Aiii) of three fully traced Dm-DRA1 cells (same as in Figure 7B) with all non-DRA R7 inputs marked (purple dots), as well as distribution of synapses along te DRA (Aiv). Note the strong inputs into the posterior Dm-DRA1 cell, originating from an ommatidium cell at the DRA/non-DRA boundary, with a putative 'mixed' fate (Ai). **B.** Top view (Bi-Biii) of three fully traced Dm-DRA2 cells (same as in Figure 7D) with all non-DRA R7 inputs marked (purple dots), as well as distribution of synapses along te DRA (Biv).

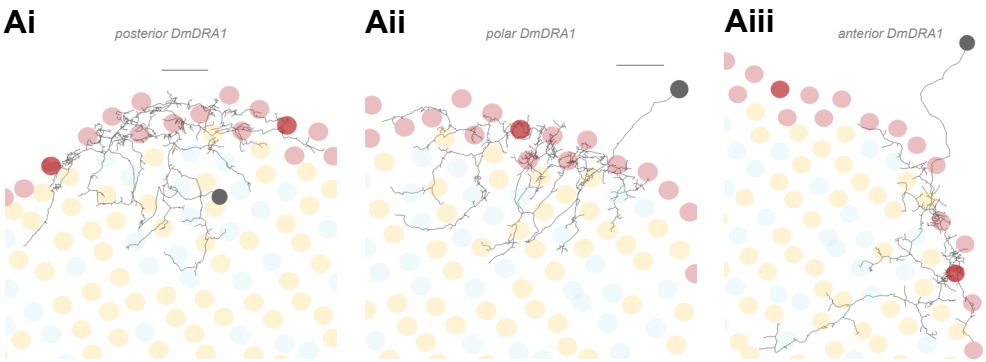

Figure 7 – figure supplement 2

1914 Figure 7 – figure supplement 2: deep projections of Dm-DRA cells

1915 **A.** Top view (Ai-Aiii) of three fully traced Dm-DRA1 cells (same as in Figure 7B) with pale and

1916 yellow fates of all non-DRA ommatidia indicated. Deep projections of Dm-DRA1 cells do not

1917 seem to show any obvious preference for pale or yellow columns.

1918

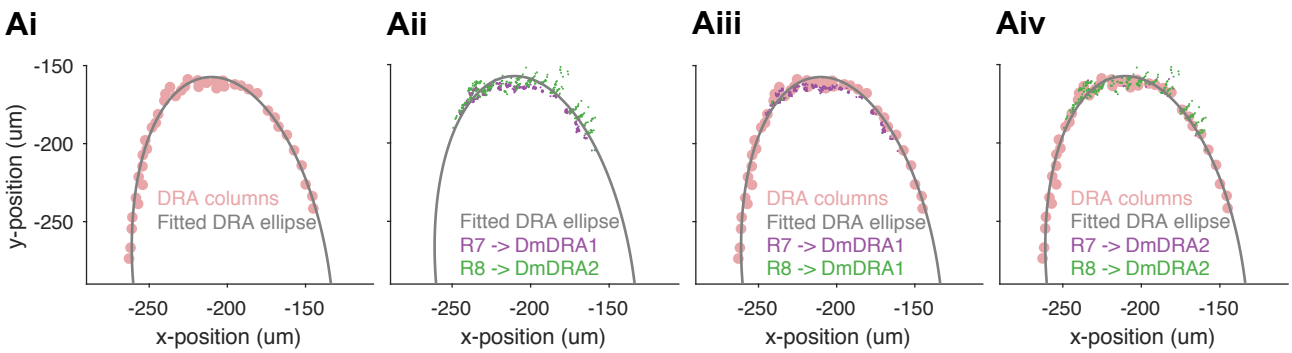

Figure 7 – figure supplement 3

Figure 7 – figure supplement 3: Fitting a linear distance of synapses along the DRA

Ai. The lateral locations of the 42 DRA columns (pink circles) were used to fit an ellipse (black line) along the DRA, where the lateral x- and y-coordinates are points in a plane that is approximately parallel to the medulla layers, and this plane does not take into account the curvature of the medulla. At the dorsal pole, there are DRA columns in two rows, and the ellipse passes between these. **Aii**. The alignment of R7 (purple) synapses to DmDRA1 cells and R8 (green) synapses to DmDRA2 vary along an axis that is approximately perpendicular to the ellipse, partly due to differences in the locations of the synapses, and partly an effect of the curvature of the medulla. For all the synapses, the projection onto the fitted DRA ellipse provides a good description of the location along the DRA. **Aiii**. Synapses from R7 (purple) to DmDRA1 cells shown with the Mi1 columns (pink circles) to appreciate their locations in the columns. The synapses are concentrated around layer 6, and this narrow depth profile generates tightly clustered synaptic locations in columns. **Aiv**. Synapses from R8 (green) to DmDRA2 cells shown with the Mi1 columns (pink circles) to appreciate their locations in the columns. The synapses are spread between the chiasm and layer 6, and this diffuse depth profile contributes to the wide, linear clusters of synapses as the medulla curves away from the plane containing the fitted DRA ellipse.

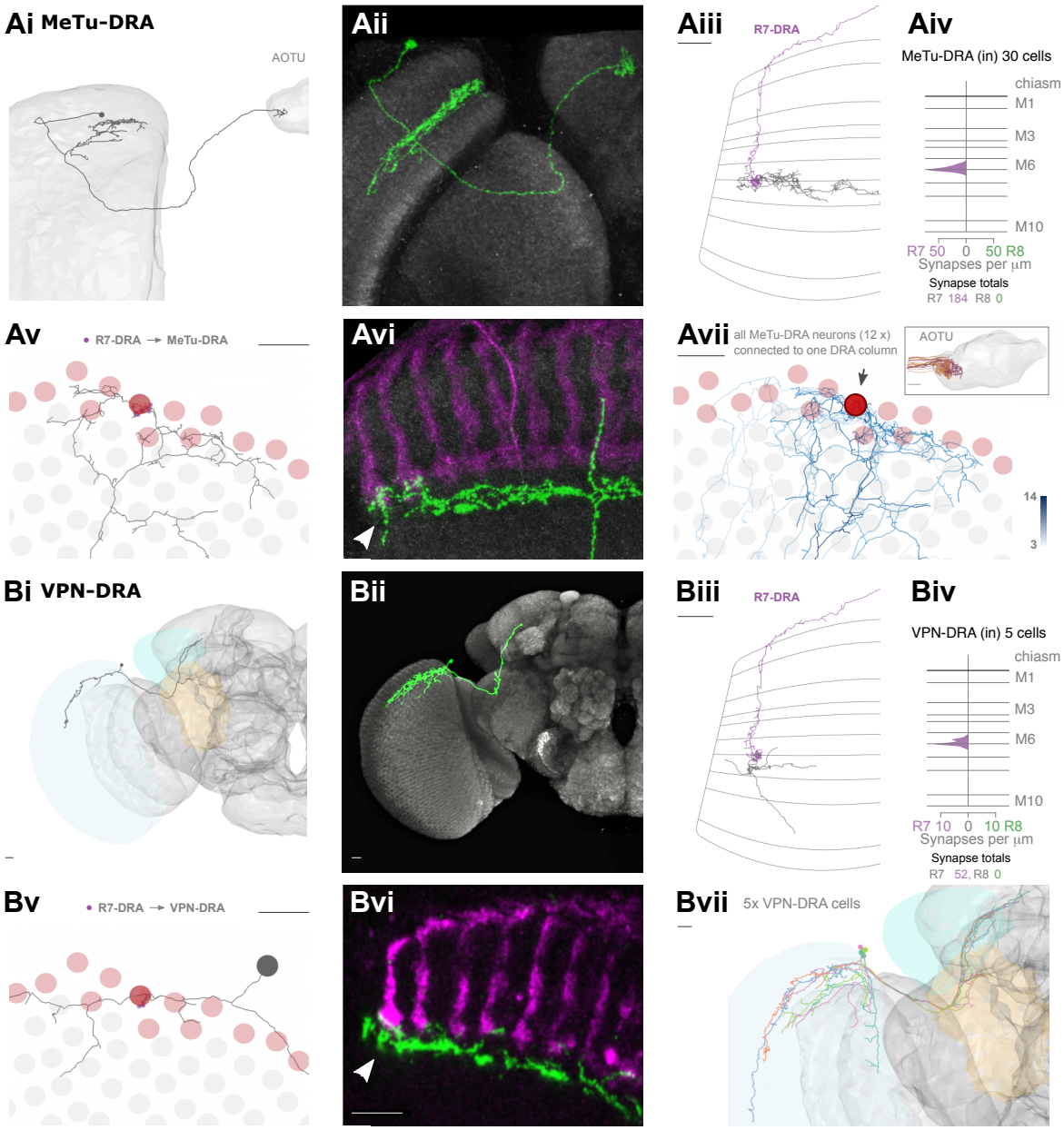
Ai MeTu-DRA
AOTU
Aii
Aiii
R7-DRA
Aiv
MeTu-DRA (in) 30 cells
chiasm
M1
M3
M6
M10
R7 50 0 50 R8
Synapses per µm
Synapse totals
R7 184 R8 0
Av
R7-DRA → MeTu-DRA
Avi
Avii
all MeTu-DRA neurons (12 x)
connected to one DRA column
AOTU
14
3
Bi VPN-DRA
Bii
Biii
R7-DRA
Biv
VPN-DRA (in) 5 cells
chiasm
M1
M3
M6
M10
R7 10 0 10 R8
Synapses per µm
Synapse totals
R7 52, R8 0
Bv
R7-DRA → VPN-DRA
Bvi
Bvii
5x VPN-DRA cells

Figure 8

Figure 8: Visual projection neurons directly connecting R7 and R8 of the DRA to the central brain

A. Synapses of R7-DRA onto MeTu-DRA cells. Ai: The entire skeleton of a fully reconstructed MeTu-DRA cell with an axon projecting to the AOTU. Aii: Light microscopic single cell clone of a MeTu-DRA cell. Aiii: Side view of a fully reconstructed MeTu-DRA skeleton (grey) innervated by R7-DRA (purple). Aiv: Layer distribution of R7-DRA synapses (purple) onto 30 MeTu-DRA cells. Av: Top view of the MeTu-DRA skeleton depicting its medulla processes innervating both DRA (red circles), and non-DRA columns. Avi: Light microscopic side view of a MeTu-DRA single cell clone (green) with exclusive contacts to DRA photoreceptor terminals (white arrowhead). Avii: Summary all MeTu-DRA skeletons connected to the same R7-DRA cell (circled column, arrow). The saturation of blue color indicates the strength of connectivity (from 3 to 14 synapses). Inset: MeTu-DRA axon terminations in the AOTU in orange and reconstructed MeTus from the central eye in purple. **B.** Synapses between R7-DRA and visual projection neurons VPN-DRA. Bi: The entire skeleton of a reconstructed VPN-DRA cell with its axon projecting to the PLP. Bii: Light microscopy image of a VPN-DRA single cell with projection to the PLP region of the central brain. A neuropile marker is shown in grey. Biii: Side view of one VPN-DRA skeleton (grey) innervated by R7-DRA (purple). Biv: Layer distribution of R7-DRA synapses onto 5 VPN-DRA cells. Bv: Top view of medulla processes formed by one reconstructed VPN-DRA skeleton (grey) with all R7-DRA synapses from the seed column (purple). Bvi: Double labeling of several VPN-DRA cells (green) with with R7 and R8 photoreceptors (purple, anti-Chaoptin). VPN-DRA processes overlap with DRA photoreceptors (white arrowhead) but also appear to show some contacts to non-DRA R-cells. Bvii: Skeletons of all reconstructed VPN-DRA cells covering the dorsal medulla.

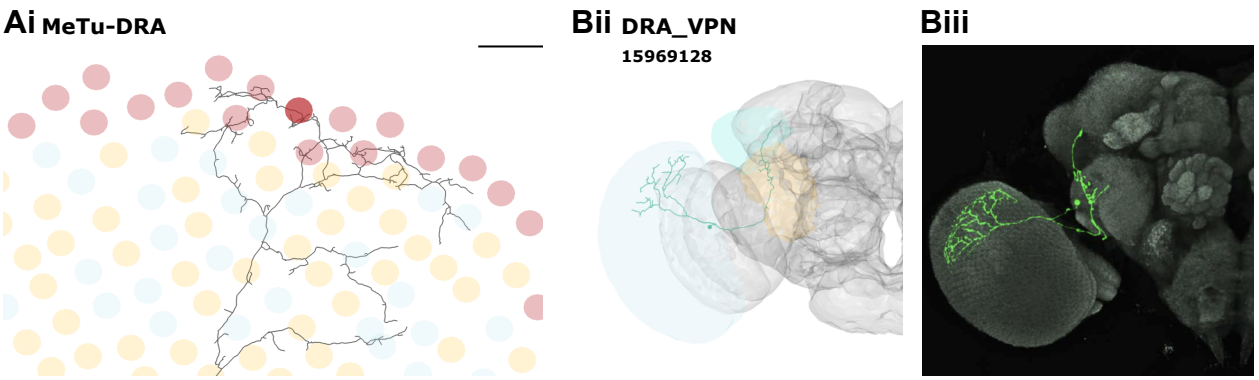

Figure 8 – figure supplement 1

Figure 8 – figure supplement 1: visual projection neuron morphology in the DRA.

A. Top view of the fully traced MeTu-DRA cell (same as in Figure 7A) with pale and yellow fates of all non-DRA ommatidia indicated. Medulla processes of MeTu-DRA do not seem to show any obvious preference for pale or yellow columns. B. Reconstructed skeleton (Bi) of an unusual VPN-DRA cell with additional processes in the central brain (putative VPN-DRA2). Light microscopy image of a cell with similar morphology (Bii).

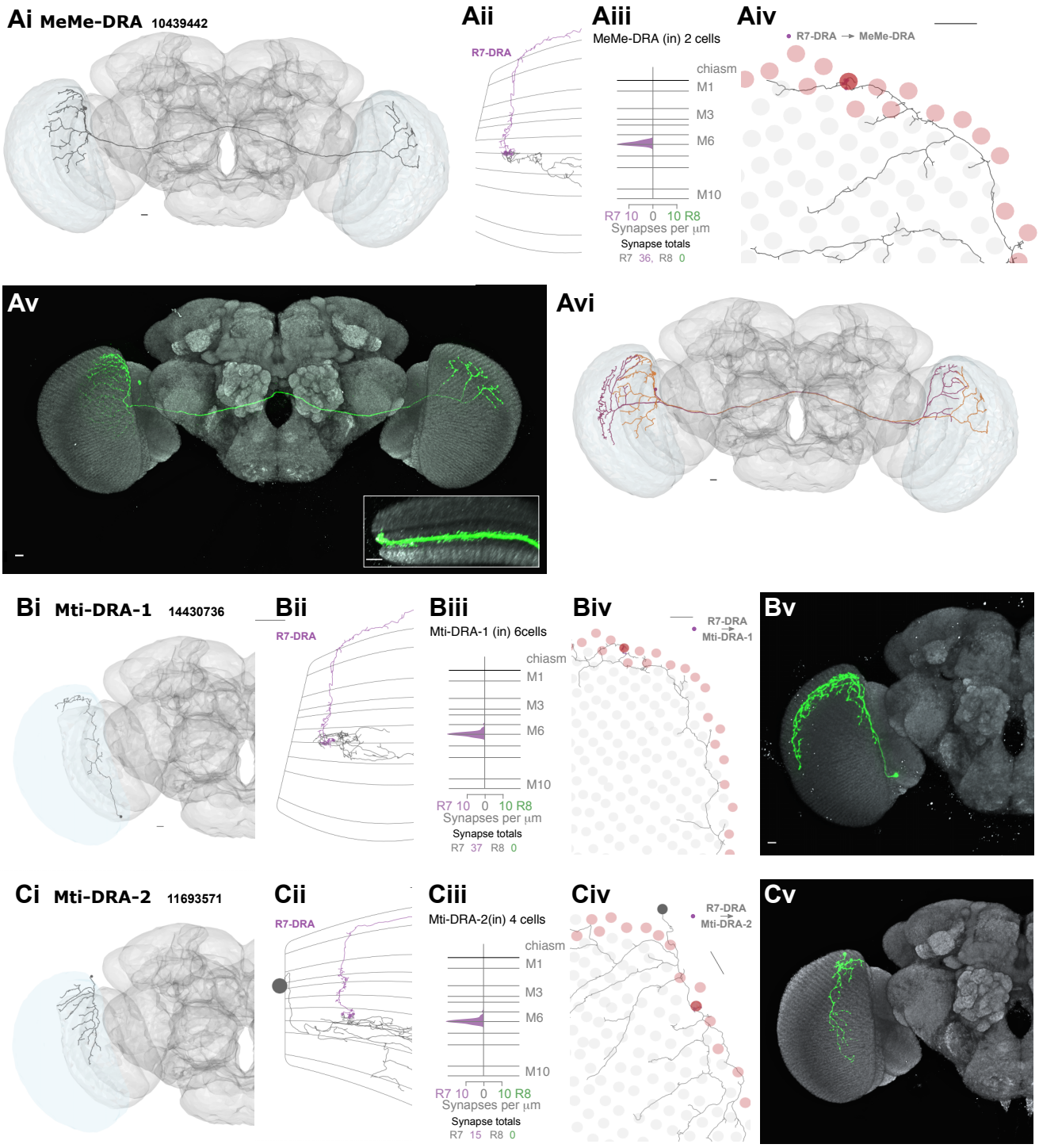
Ai MeMe-DRA 10439442
Aii
R7-DRA
Aiii
MeMe-DRA (in) 2 cells
chiasm
M1
M3
M6
M10
R7 10 0 10 R8
Synapses per µm
Synapse totals
R7 36, R8 0
Aiv
R7-DRA → MeMe-DRA
Av
Avi
Bi Mti-DRA-1 14430736
Bii
R7-DRA
Biii
Mti-DRA-1 (in) 6cells
chiasm
M1
M3
M6
M10
R7 10 0 10 R8
Synapses per µm
Synapse totals
R7 37 R8 0
Biv
R7-DRA
→
Mti-DRA-1
Bv
Ci Mti-DRA-2 11693571
Cii
R7-DRA
Ciii
Mti-DRA-2(in) 4 cells
chiasm
M1
M3
M6
M10
R7 10 0 10 R8
Synapses per µm
Synapse totals
R7 15 R8 0
Civ
R7-DRA
→
Mti-DRA-2
Cv

Figure 9

Figure 9: Newly identified photoreceptor targets in the DRA region of the medulla

A. Synapses from R7-DRA onto bilaterally projecting MeMe-DRA neurons. Ai: The skeleton of a reconstructed MeMe-DRA cell with putative axonic projections to the dorsal periphery of the contralateral medulla. Aii: Side view of one MeMe-DRA skeleton (grey) innervated by R7-DRA (purple). Aiii: layer distribution of R7-DRA synapses onto 2 MeMe-DRA cells. Aiv: Top view of medulla processes formed by the reconstructed MeMe-DRA skeleton (grey) with all R7-DRA synapses from the seed column (purple). Av: Light microscopy image of an MCFO-labeled MeMe-DRA single cell (green) with processes to the contralateral medulla. Inset: Reconstructed side view of dendrites of a MeMe-DRA cell in the medulla. Note that arbors move upwards towards photoreceptor terminals in the DRA region (arrowhead). Avi: Neighboring relationships of two reconstructed MeMe-DRA skeletons (purple and orange) connecting both medullas in a reciprocal manner, while flipping the innervated DRA regions along the anterior-posterior axis. **B.** Synapses from R7-DRA onto medulla tangential intrinsic neurons (Mti) forming froming two putative Mti-DRA populations (Mti-DRA-1 and Mti-DRA-2). Bi: The skeleton of a reconstructed Mti-DRA-1 cell with processes covering the dorsal periphery of the medulla. Bii: Side view of one Mti-DRA-1 skeleton (grey) innervated by R7-DRA (purple). Biii: Layer distribution of R7-DRA synapses onto 6 Mti-DRA-1 cells. Biv: Top view of medulla processes formed by one reconstructed Mti-DRA-1 skeleton (grey) with all R7-DRA synapses from the seed column (purple). Bv: Light microscopy image of a single cell similar to the reconstructed Mti-DRA covering the dorsal periphery of the medulla. C. Synapses from R7-DRA onto medulla tangential intrinsic neurons (Mti) Mti-DRA-2 Ci: The skeleton of a reconstructed Mti-DRA-2 cell with processes covering dorsal parts of the medulla. Cii: Side view of one Mti-DRA-2 skeleton (grey) innervated by R7-DRA (purple). Ciii: Layer distribution of R7-DRA synapses onto 4 Mti-DRA-2 cells. Civ: Top view of medulla processes formed by one reconstructed Mti-DRA-2 skeleton (grey) with all R7-DRA synapses from the seed column (purple). Civ: Light microscopic image of a putatively corresponding single cell clone (green) covering dorsal parts of the medulla.

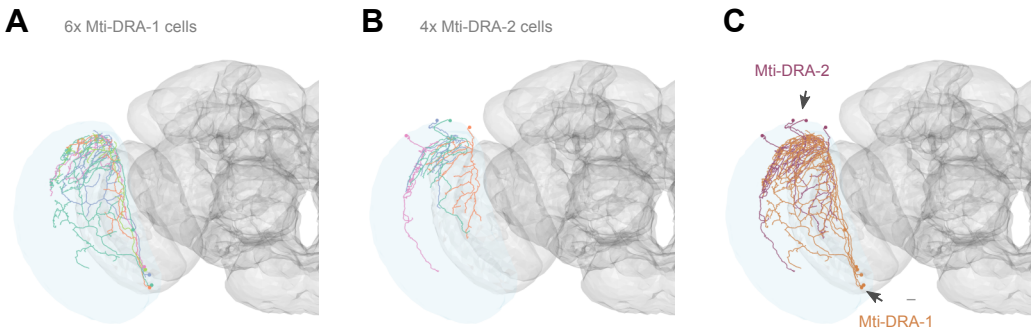

Figure 9 – figure supplement 1

Figure 9 – figure supplement 1: Medulla tangential intrinsic cells in the DRA.

A. All reconstructed Mti-DRA-1 skeletons (6x) covering the dorsal medulla. **B**. All reconstructed Mti-DRA-2 skeletons (4x) covering the dorsal medulla. **C**. Separation of putative Mti-DRA subtypes. One population with cell bodies located ventrally (putative cell type Mti-DRA1, orange, arrow), and several cells with dorsally located cell bodies (putative Mti-DRA2, purple, arrow).

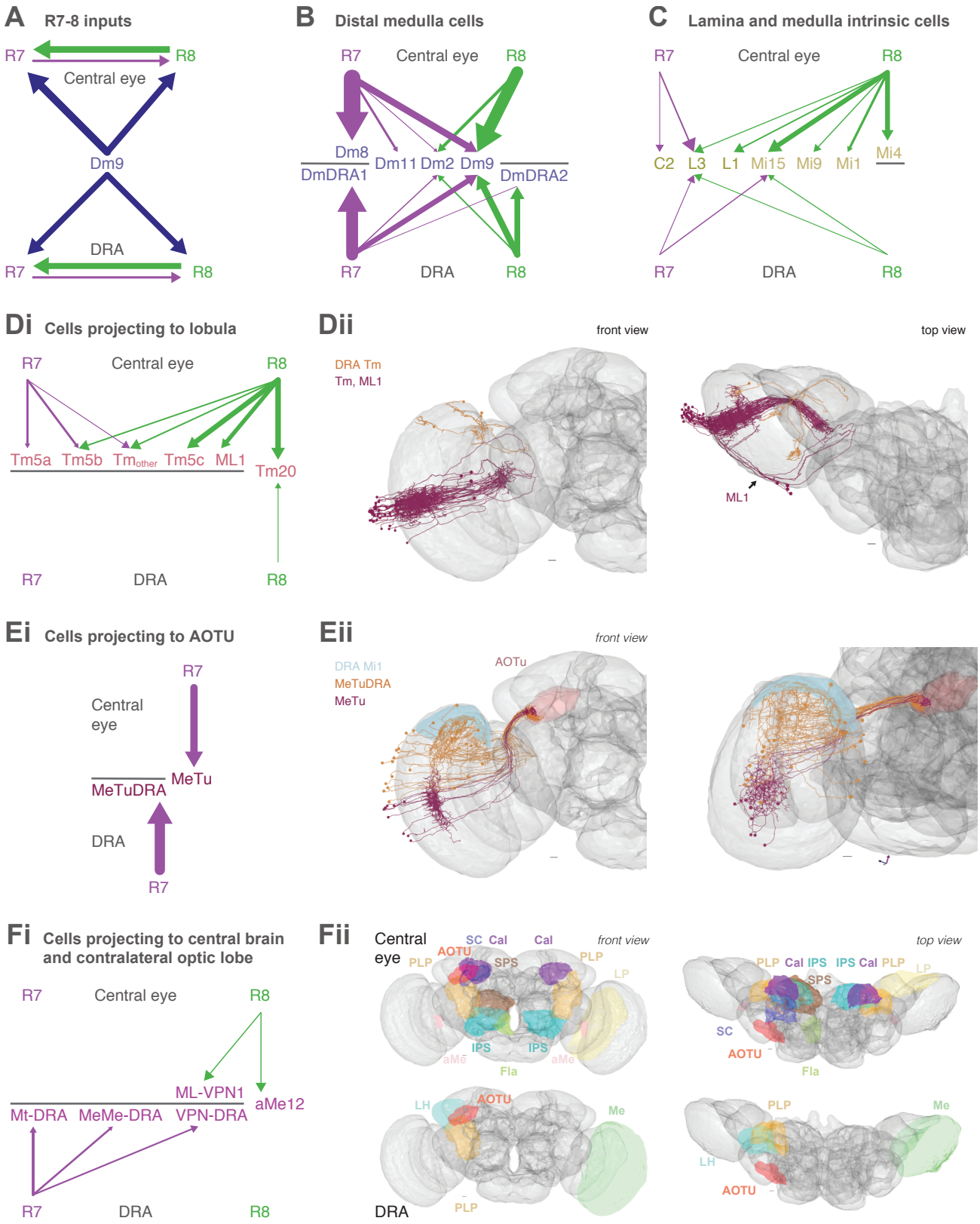
A
R7-8 inputs
R7
R8
Central eye
Dm9
DRA
R7
R8
B
Distal medulla cells
R7
Central eye
R8
Dm8
DmDRA1
Dm11
Dm2
Dm9
DmDRA2
R7
DRA
R8
C
Lamina and medulla intrinsic cells
R7
Central eye
R8
C2
L3
L1
Mi15
Mi9
Mi1
Mi4
R7
DRA
R8
Di
Cells projecting to lobula
R7
Central eye
R8
Tm5a
Tm5b
Tm other
Tm5c
ML1
Tm20
R7
DRA
R8
Dii
front view
top view
DRA Tm
Tm, ML1
ML1
Ei
Cells projecting to AOTU
R7
Central eye
MeTu
MeTuDRA
DRA
R7
Eii
front view
DRA Mi1
MeTuDRA
MeTu
AOTu
Fi
Cells projecting to central brain and contralateral optic lobe
R7
Central eye
R8
ML-VPN1
aMe12
Mt-DRA
MeMe-DRA
VPN-DRA
R7
DRA
R8
Fii
Central eye
front view
top view
SC
Cal
Cal
AOTU
PLP
SPS
PLP
LP
IPS
IPS
aMe
aMe
Fla
PLP
Cal
IPS
IPS
Cal
PLP
LP
SPS
SC
AOTU
Fla
LH
AOTU
Me
PLP
DRA
PLP
Me
LH
AOTU

Figure 10

Figure 10: Direct comparison of central versus DRA connectivity by cell type

A. Schematic summary of synaptic connections between central or DRA R7 and R8, as well as other cell types providing synaptic feedback to them purple). In all panels, arrow widths are proportional to the numbers of synapses per seed column, and weak connections were excluded for clarity by a threshold of >4 synapses per column. Despite the differences in modality, the circuit organization of inputs to R7 and R8 cells is conserved in the central eye and DRA. **B.** Synapses between R7/R8 and Dm cell types in central and DRA columns. Note the presence of a second Dm8-like cell type downstream of R8 only in the DRA (Dm-DRA2). **C.** Summary of inner photoreceptor connections with lamina and Mi and Mti cells in central and DRA columns. The connections from R8 to these cells were very reduced in the DRA, and Mi4 was not a photoreceptor target in the DRA seed columns. **D.** Summary of lobula connections. Di: Schematic of central and DRA R7/R8 connections with Tm and ML1 cells. Note the virtual absence of lobula connectivity in the DRA. Dii: Front view (left) and top view (right) of all reconstructed central Tm and ML1 skeletons (claret) and Tm skeletons from the DRA (orange). **E.** Summary of MeTu cell connections. Ei: Schematic of central and DRA R7 cells targeting different MeTu populations. Eii: Front view (left) and DRA view (right) of all central MeTu skeletons (purple) and MeTu-DRA skeletons (orange), with axons following the same tract but terminating with spatially separated axon target areas in the AOTU. **F.** Summary of other visual projection neurons. Fi: Diagram summarizing VPN connectivity in central and DRA columns. While R8 input dominates in central eye columns, R7 input dominates in the DRA. Fii: Front view (left) and top view (right) of VPN target areas in the central brain. VPNs from both central eye and DRA project to the posterior lateral protocerebrum (PLP, golden yellow) and the AOTU (red). The central eye VPNs additionally project ispsilaterally to the mushroom body calyx (mauve), accessory medulla (aMe, pink), superior clamp (SC, dark blue), flange (Fla, green), superior posterior slope (SPS, brown), inferior posterior slope (IPS, cyan), and contralaterally to the PLP, mushroom body calyx, aMe, and lobula plate (LP, cream). The DRA VPNs project ipsilaterally to the AOTU, plp, and lateral horn (LH, turquoise), and contralaterally to the medulla (Me, lime green).

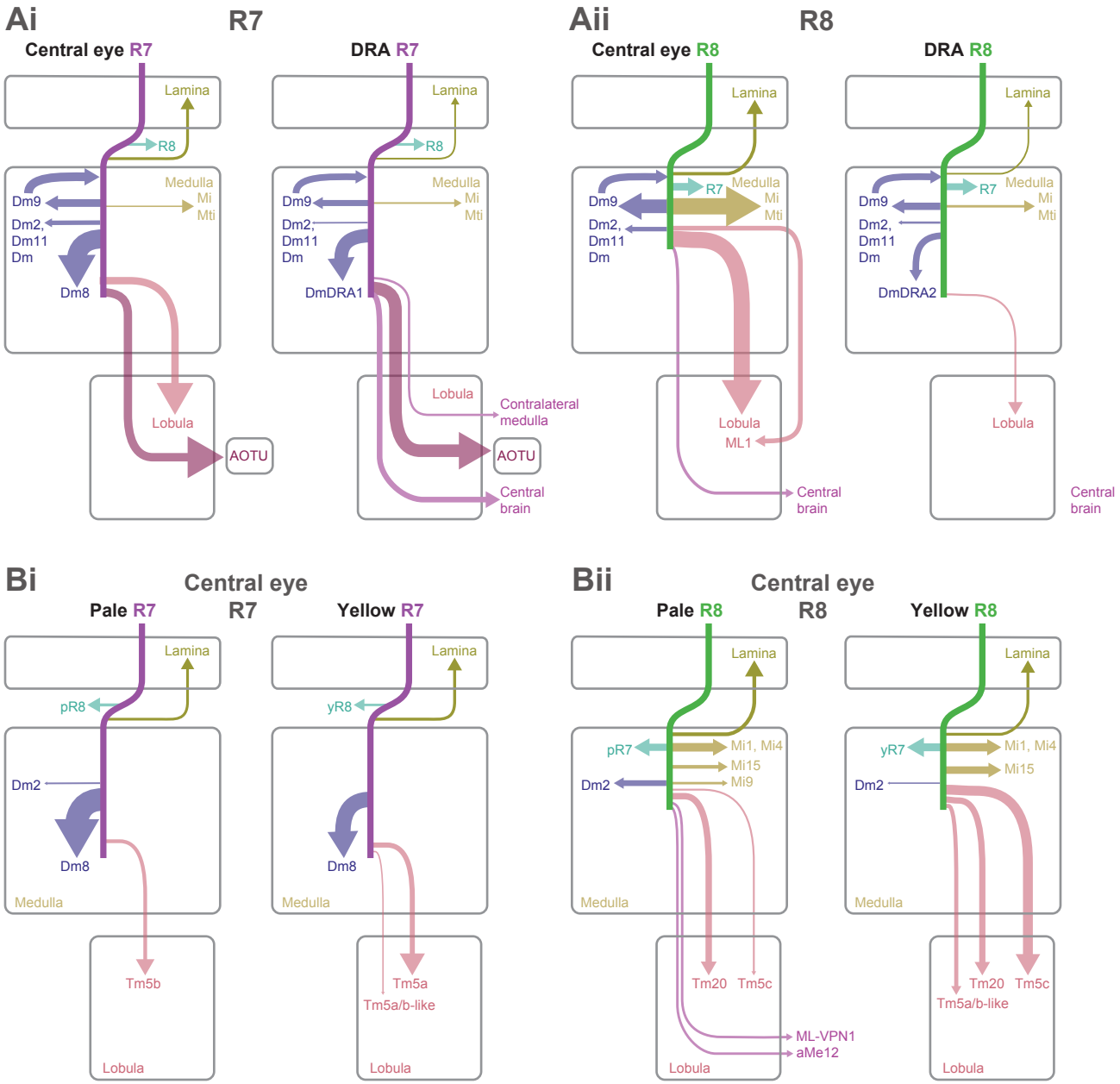
Ai
R7
Central eye R7
DRA R7
Lamina
R8
Medulla
Mi
Mti
Dm9
Dm2,
Dm11
Dm
Dm8
DmDRA1
Lobula
AOTU
Contralateral
medulla
Central
brain
Aii
R8
Central eye R8
DRA R8
R7
ML1
DmDRA2
Bi
Central eye
R7
Pale R7
Yellow R7
pR8
yR8
Dm2
Tm5b
Tm5a
Tm5a/b-like
Bii
Pale R8
Yellow R8
pR7
yR7
Mi1, Mi4
Mi15
Mi9
Tm20
Tm5c
ML-VPN1
aMe12

Figure 11

Figure 11: Direct comparison of central versus DRA, and pale versus yellow pathways

A. Graphical comparison of central and DRA synaptic pathways. In all panels, the arrow widths are proportional to the numbers of synapses per seed column, and weak connections were excluded for clarity by a threshold of >4 synapses per column. Ai: Arrows indicating the relative weight of R7 connections in central (cell types post-synaptic to pale and yellow R7) and in the DRA. Aii: Arrows indicating the relative weight of R8 connections in central (sum of pale and yellow R8) and in the DRA. Connections to the lobula neuropil are dominated by R8 targets in the central eye. Lobula connections are virtually absent in the DRA (synapse numbers below 1% of total synapse count), where connectivity of R8-DRA is dramatically reduced, limited to local computations in the medulla. The projections to the central brain are driven by R8 in the central eye, but by R7 in the DRA. **B.** Graphical comparison of central pale and yellow-specific synaptic pathways. Bi: Arrows indicating the relative weight of pale R7 versus yellow R7 connections in central seed columns. Columnar cell types such as lamina cells have the capacity to preserve pale and yellow information, and Dm8 cells are most densely innervated by their home column input. Tm5a cells were selective for yellow R7, Tm5b cells were selective for pale R7, and the Tm5a-like and Tm5b-like cells were selective for yellow R8, but also received yellow R7 synapses. Bii: Arrows indicating the relative weight of pale R8 versus yellow R8 connections in central seed columns. Columnar medulla cells that have the capacity to preserve pale and yellow information were targets of R8 cells. The aMe12 and ML-VPN1 cell types were specific for pale R8 input, while Tm5c had a strong bias for yellow R8, along with the Tm5a-like and Tm5b-like cells.

Table 1

Synaptic targets of central eye seed column R7 and R8 photoreceptors

Type	No.	pR7	yR7	pR8	yR8	Sum	%R7	%R8	%p	%y	%Total
Dm9	6	94	66	142	143	445	36.0	64.0	53.0	47.0	16.4
Dm8	15	235	161	0	0	396	100.0	0.0	59.3	40.7	14.6
MeTu	7	82	93	0	0	175	100.0	0.0	46.9	53.1	6.5
R7	5	0	3	75	82	160	1.9	98.1	46.9	53.1	5.9
Tm5c	6	8	9	20	103	140	12.1	87.9	20.0	80.0	5.2
Tm20	4	5	3	67	65	140	5.7	94.3	51.4	48.6	5.2
Mi15	4	6	7	38	81	132	9.8	90.2	33.3	66.7	4.9
Mi4	4	0	0	58	58	116	0.0	100.0	50.0	50.0	4.3
ML1	4	0	0	58	41	99	0.0	100.0	58.6	41.4	3.7
Dm2	4	18	3	60	15	96	21.9	78.1	81.2	18.8	3.5
Dm11	2	28	27	4	4	63	87.3	12.7	50.8	49.2	2.3
L3	4	19	17	12	13	61	59.0	41.0	50.8	49.2	2.3
Mi1	4	0	0	31	28	59	0.0	100.0	52.5	47.5	2.2
R8	4	31	26	1	0	58	98.3	1.7	55.2	44.8	2.1
Tm5a	2	0	53	0	0	53	100.0	0.0	0.0	100.0	2.0
Tm5b	2	39	0	3	6	48	81.2	18.8	87.5	12.5	1.8
Tm	9	17	4	7	16	44	47.7	52.3	54.5	45.5	1.6
Tm5b-like	3	0	14	0	27	41	34.1	65.9	0.0	100.0	1.5
Mi9	4	3	9	26	1	39	30.8	69.2	74.4	25.6	1.4
L1	4	2	1	21	14	38	7.9	92.1	60.5	39.5	1.4
aMe12	2	4	0	26	0	30	13.3	86.7	100.0	0.0	1.1
Dm	5	11	7	6	5	29	62.1	37.9	58.6	41.4	1.1
ML-VPN1	3	0	0	26	1	27	0.0	100.0	96.3	3.7	1.0
C2	2	7	13	6	0	26	76.9	23.1	50.0	50.0	1.0
Mt-VPN	4	0	12	3	8	23	52.2	47.8	13.0	87.0	0.8
Mti	3	2	0	10	7	19	10.5	89.5	63.2	36.8	0.7
Tm5a-like	1	0	1	0	16	17	5.9	94.1	0.0	100.0	0.6
TmY10	1	1	0	6	0	7	14.3	85.7	100.0	0.0	0.3
Mi10	1	0	0	0	5	5	0.0	100.0	0.0	100.0	0.2
Mi	1	2	1	0	0	3	100.0	0.0	66.7	33.3	0.1
C3	1	0	0	0	3	3	0.0	100.0	0.0	100.0	0.1
Identified <3	26	5	14	14	4	37	51.4	48.6	51.4	48.6	1.4
Unidentified >=3	2	0	0	5	3	8	0.0	100.0	62.5	37.5	0.3
Unidentified <3	62	9	15	22	24	70	34.3	65.7	44.3	55.7	2.6
Total	211	628	559	747	773	2707	43.8	56.2	50.8	49.2	100.0

Table 2

Cells that synapse onto central eye seed column R7 and R8 photoreceptors

Type	No.	pR7	yR7	pR8	yR8	Sum	%R7	%R8	%p	%y	%Total
Dm9	6	90	92	79	72	333	54.7	45.3	50.8	49.2	57.0
R8	4	75	82	1	0	158	99.4	0.6	48.1	51.9	27.1
R7	4	0	0	31	26	57	0.0	100.0	54.4	45.6	9.8
Mt-VPN	1	0	2	0	3	5	40.0	60.0	0.0	100.0	0.9
C2	1	2	3	0	0	5	100.0	0.0	40.0	60.0	0.9
L3	1	0	0	4	0	4	0.0	100.0	100.0	0.0	0.7
Identified <3	11	4	2	4	8	18	33.3	66.7	44.4	55.6	3.1
Unidentified >=3	0	0	0	0	0	0	0.0	0.0	0.0	0.0	0.0
Unidentified <3	4	1	2	1	0	4	75.0	25.0	50.0	50.0	0.7
Total	32	172	183	120	109	584	60.8	39.2	50.0	50.0	100.0

Table 3

Synaptic targets of DRA seed column R7 and R8 photoreceptors

Type	No.	R7-DRA	R8-DRA	Sum	%Total	%R7	%R8
Dm-DRA1	20	212	0	212	15.9	25.3	0.0
Dm9	6	95	115	210	15.7	11.3	23.0
MeTu-DRA	30	184	0	184	13.8	22.0	0.0
R7-DRA	3	1	108	109	8.2	0.1	21.6
Dm-DRA2	9	3	103	106	7.9	0.4	20.6
Dm2	4	21	27	48	3.6	2.5	5.4
R8-DRA	3	41	1	42	3.1	4.9	0.2
Mi15	4	21	18	39	2.9	2.5	3.6
Mti-DRA-1	6	37	0	37	2.8	4.4	0.0
MeMe-DRA	2	36	0	36	2.7	4.3	0.0
L3	3	16	16	32	2.4	1.9	3.2
VPN-DRA	6	30	0	30	2.2	3.6	0.0
L1	3	9	9	18	1.3	1.1	1.8
Tm20	3	0	16	16	1.2	0.0	3.2
Mti-DRA-2	4	15	0	15	1.1	1.8	0.0
Mi1	3	6	9	15	1.1	0.7	1.8
MeTu	2	13	0	13	1.0	1.6	0.0
Tm5-like	1	0	12	12	0.9	0.0	2.4
Mi9	2	0	12	12	0.9	0.0	2.4
Dm11	1	4	8	12	0.9	0.5	1.6
aMe12	1	3	1	4	0.3	0.4	0.2
TmY	1	0	3	3	0.2	0.0	0.6
ML-VPN2	1	3	0	3	0.2	0.4	0.0
C2	1	2	1	3	0.2	0.2	0.2
Identified <3	33	34	14	48	3.6	4.1	2.8
Unidentified >=3	2	5	5	10	0.7	0.6	1.0
Unidentified <3	57	46	21	67	5.0	5.5	4.2
Total	211	837	499	1336	100.0	100.0	100.0

Table 4

Cells that synapse onto DRA seed column R7 and R8 photoreceptors

Type	No.	R7-DRA	R8-DRA	Sum	%Total	%R7	%R8
Dm9	4	105	106	211	54.7	46.1	67.1
R8-DRA	3	108	1	109	28.2	47.4	0.6
R7-DRA	3	1	41	42	10.9	0.4	25.9
C2	2	4	4	8	2.1	1.8	2.5
Mi15	1	2	2	4	1.0	0.9	1.3
Identified <3	9	6	3	9	2.3	2.6	1.9
Unidentified >=3	0	0	0	0	0.0	0.0	0.0
Unidentified <3	2	2	1	3	0.8	0.9	0.6
Total	24	228	158	386	100.0	100.0	100.0